Addressing Computational Challenges in Renewable Energy Integration: Behind-the-Meter to Transmission

by

Kaitlyn Nicole Garifi

B.A., Mathematics, University of California Santa Cruz, 2015

B.S., Bioengineering, University of California Santa Cruz, 2015

M.S., Electrical Engineering, University of Colorado Boulder, 2017

A thesis submitted to the

Faculty of the Graduate School of the

University of Colorado in partial fulfillment

of the requirements for the degree of

Doctor of Philosophy

Department of Electrical, Computer, and Energy Engineering

2020

Committee Members:

Kyri Baker, Chair

Behrouz Touri

Dane Christensen

Emiliano Dall'Anese

Marco Nicotra

Garifi, Kaitlyn Nicole (Ph.D., Electrical Engineering)

Addressing Computational Challenges in Renewable Energy Integration: Behind-the-Meter to Transmission

Thesis directed by Professor Kyri Baker and Professor Behrouz Touri

Integrating renewable energy into the power grid is challenging due to the intermittent, variable, and non-dispatchable characteristics of renewable energy generation. From behind-the-meter (BTM) to transmission settings, this thesis employs stochastic optimization methods to account for uncertainty in renewable energy generation and addresses computational challenges of including grid-connected energy storage systems (ESSs) models in optimization problems.

For a BTM setting, a stochastic model predictive control (MPC)-based residential energy management system (EMS) algorithm is proposed to optimally coordinate residential electricity usage, controllable appliances, and customer-owned energy sources (e.g., rooftop photovoltaic (PV) panels and an ESS). Instead of computationally limiting sampling-based stochastic optimization approaches, chance constraints are used to ensure both a demand response (DR) event and indoor thermal comfort are satisfied with a high probability given uncertainty in PV generation and weather forecasts. Case study results highlight the residential EMS algorithm performance from both customer and utility perspectives.

For large-scale wind power integration in a transmission setting, a two-stage stochastic flexible line capacity rating algorithm is proposed to determine economic conventional generator dispatch while minimizing the amount of curtailed wind power across probable wind power generation scenarios. Flexible line ratings are incorporated into the model using a sample average approximation of an integer chance constraint, limiting the probability of non-nominal line capacity rating violations. Case study results demonstrate the flexible line capacity rating algorithm can reduce total average wind power curtailment by 40% compared to the static line rating case.

From BTM to transmission settings, grid-connected ESSs are often coupled with renewable

energy sources in optimization models for many applications in power systems. Theoretical analysis is provided that guarantees a relaxed convex ESS model will produce a physically realizable optimal control strategy with non-simultaneous ESS charging and discharging. The relaxed convex ESS model omits the non-convex complementarity constraint that explicitly ensures non-simultaneous ESS charging and discharging, avoiding computationally limiting non-convex or mixed-integer optimization solvers. Case studies with the relaxed convex ESS model show the optimal solutions satisfy the omitted complementarity constraint, result in significantly faster computation times, and the penalty-based approach has a negligible impact on the optimal solution.

Dedication

To everyone who made me laugh along the way.

Acknowledgements

First, thank you to my advisors Dr. Kyri Baker and Dr. Behrouz Touri for their time and support throughout my PhD, for giving me this opportunity be their student, and for their mentorship and invaluable advice. I hope to continue collaborating with them in the future.

Thank you to the Air Force Office of Scientific Research, the U.S. Department of Energy Advanced Research Projects Agency (ARPA-E), the National Renewable Energy Laboratory, and the CU Boulder ECEE department for making this research possible.

Thank you to Dr. Dane Christensen, Dr. Marco Nicotra, and Dr. Emiliano Dall'Anese who were kind enough to serve on my thesis committee. Their feedback and comments were greatly appreciated. I am forever grateful for Dane's continued support, mentorship, and all the opportunities that Dane has shared with me. Thank you to Dr. Lucy Pao for her support, guidance, and funding during the beginning of my Ph.D.

To the team at Lineage Logistics, thank you for inviting me to solve genuinely interesting real problems. To the researchers I worked with at the National Renewablnergy Laboratory and Sandia National Laboratories, thank you for the valuable opportunity to learn and work on research in many areas within power systems.

To my friends and my entire support network, thank you for all the board game nights, family dinners, happy hours, potlucks, breakfast club meetings, swim workouts, hikes, trail runs, marathons, and pasture walks. To my parents, thank you for your support and for providing me with the opportunities to make it to this point and be successful. To Nik, thank you for your support, patience, and love, and for always having a pun ready for any situation.

Contents

Chapter

Tables

Table

Figures

Figure

Chapter 1

Introduction

This thesis is motivated by the need to address the stable integration of renewable energy into the power grid, which is challenging due to the intermittent, variable, and non-dispatchable characteristics of renewable energy generation. In this thesis, renewable energy integration is considered in both behind-the-meter settings with distributed renewable energy resources and transmission grid settings with large wind farms. To aid with the variability of renewable energy resources, they are often coupled with electrical energy storage systems. This dissertation also addresses the use of a computationally tractable energy storage system model for use in large-scale simulations and provides proper behavior guarantees for this model. This chapter starts with an overview of renewable energy integration and grid-connected electrical energy storage systems. Then, the main contributions of this thesis are briefly described, followed by an outline of this dissertation.

1.1 Renewable Energy Integration

Over half the states in the U.S., in addition to local governments, have adopted renewable portfolio standards that require a certain percentage of electricity sold by utility companies must come from renewable sources. These policies aim to reduce carbon emissions to combat climate change and directly impact state and utility investments in renewable technologies [1, 2]. As of 2020, most state targets require that 10%-45% of their electricity must come from renewable energy sources; however, 14 states (including Colorado) have requirements of over 50% [2]. Adopting these standards has led to a substantial increase in renewable energy sources being added to the grid. In

the U.S., 20% of the electricity generating capacity is from renewable resources, where 42.9% of all new capacity additions are renewable resources (as of 2018) [3]. As increasing amounts of renewable energy are integrated into the grid to meet these targets, integration has presented new challenges in power grid operation due to variability in renewable generation availability and uncertainty in renewable generation forecasts.

Furthermore, renewable energy generation does not necessarily coincide with demand. This is best seen in the well-known "duck curve" that shows the net load, which is calculated by subtracting the forecasted renewable generation from the predicted electricity demand [4]. This curve suggests that dispatchable conventional generation sources (such as coal and natural gas) are relied upon in the morning until solar energy generation becomes available, after which the need conventional generation declines quickly for the duration of the daylight hours, and then followed by a steep increase in conventional generation needed to meet the evening peak demand as the sun goes down [4]. These fast changes in the electricity generation mix in the mornings and evenings due to solar energy availability highlights the required fast ramping of conventional generators (if even feasible within their operating limits), and both generation- and demand-side flexibility. In this dissertation, both demand- and generation-side solutions are considered to account for variability in renewable energy generation.

1.1.1 Demand-side Residential Energy Management

This dissertation focuses on behind-the-meter (BTM) energy management solutions to improve the flexibility of customer demand and aid the integration of renewable energy. In particular, we consider residential energy management solutions since residential buildings account for more than 37.6% of total electricity consumption in the U.S., which is more than the transportation, commercial, or industrial sectors [5]. Residential energy management systems provide demand-side energy management by coordinating multiple flexible residential appliances in real-time, given user preferences and renewable energy generation forecasts [6, 7]. Flexible appliances can have their usage shifted in time to better align with renewable energy availability. Home energy management

systems (HEMS) can increase the energy efficiency of a home by leveraging controllable residential devices, such as heating, ventilation, and air-conditioning (HVAC) systems, which account for over 50% of total residential electricity usage [5], to be operated during times when renewable energy generation is available. This dissertation first focuses on a stochastic model predictive control based HEMS algorithm that accounts for uncertainty in customer-owned renewable resource generation and incorporates future forecast information such as weather and electricity demand in order to optimally control residential energy generation and local consumption. Various demand-side utility electricity pricing structures aimed at effectively using available renewable energy and shaping the aggregate load curve are considered, including feed-in tariffs, time-of-use prices, and net metering. The performance of the HEMS algorithm is considered from both utility and customer perspectives.

1.1.2 Generation-side Transmission Capacity Flexibility

Generation-side solutions are also considered for improving the grid's flexibility to respond to quickly changing electricity generation mixes as more renewable energy is added to the total generation capacity. There is currently over 107,300 MW of installed wind capacity in the U.S. (as of July 2020) [8]. This growing amount is challenging how our transmission grid is operated due to the variability of wind power availability and uncertainty in wind forecasts. Additionally, as the penetration of wind power increases, more situations arise where wind power must be curtailed to minimize transmission congestion [9, 10]. Wind curtailment primarily occurs due to limited available transmission during a particular time to incorporate some or all of the wind, or high wind power availability at times of low electricity demand and excess generation cannot be exported to other areas due to transmission constraints [9, 10]. This dissertation also proposes a stochastic algorithm for flexible transmission line capacity limits, while maintaining safe operation, to minimize curtailment of energy generated by wind farms.

1.2 Grid-connected Electrical Energy Storage Systems: Grid Benefits and Computational Challenges

As mentioned previously, the intermittent nature of most renewable energy sources is one of the main challenges of integrating renewable generation into the power grid. Variability in renewable energy sources or renewable energy forecast errors can be partially addressed by incorporating distributed electrical energy storage systems (ESS) in the power grid [11]. Grid-connected ESSs are one of the main technologies suggested for stable integration of renewable energy into the grid. Not only can ESSs act like a generation source, they can simultaneously provide many other valuable grid services as well. These services include bulk energy services, ancillary services, transmission services, distribution services, and customer electricity support [11–15]. The services that grid-connected ESSs provide and their definitions are summarized in Table 1.1.

Due to the many services that grid-connected ESSs provide, they are regularly included in research on renewable energy integration in all aspects of grid operation. At the core of many such studies including an ESS, there is an ESS model that describes the physical dynamics and limits of the system. The model is used to determine how to intelligently operate the battery, i.e., charging and discharging decisions, to maximize the value of the services provided by the ESS [16]. However, when deciding on an ESS model, there are many trade-offs between model accuracy and computational complexity, which are surveyed in [16]. To accurately capture round-trip efficiency in an ESS model, separate terms are used for ESS charging and discharging. This requires enforcing a constraint in the ESS model that prohibits simultaneous charging and discharging. One way to formulate this constraint without introducing binary variables into the model is to use a complementarity constraint, which can be computationally limiting since it is non-convex. This dissertation addresses the use of a relaxed convex ESS model in both BTM and optimal power flow settings. Theoretical analysis is provided that guarantees proper model behavior, i.e., behavior that satisfies the complementarity constraint, in general BTM and optimal power flow settings. Furthermore, situations where proper model behavior for the relaxed convex ESS model cannot be

guaranteed are highlighted.

1.3 Contributions

The main contributions addressed in this dissertation are listed below.

- **Contribution 1. Stochastic residential energy management system algorithms for demand response and with varying controllable resources.** The optimal coordination of residential electricity usage and customer-owned renewable electricity generation is determined by a chance constrained model predictive control (MPC) home energy management system (HEMS) algorithm. In one scenario, chance constraints are used to ensure a utility-requested demand response (DR) event and indoor thermal comfort are satisfied with a high probability given the uncertainty in available photovoltaic (PV) generation and the outdoor temperature forecast. Simulation results for various user preferences and probabilistic model parameters demonstrate that the HEMS algorithm can effectively respond to demand response requests. In a second scenario, the performance of the MPC-based HEMS algorithm as the set of controllable appliances varies is considered to capture a variety of homes that better reflect available controllable resources found in homes today. Similar to the first scenario, the chance constraint ensures indoor thermal comfort is satisfied with a high probability given the uncertainty in the outdoor temperature and solar irradiance forecasts. Simulation results for homes with different sets of controllable resources under both a constant electricity price and time-of-use (TOU) electricity price are evaluated for both customer- and utility-centered metrics. Compared to HEMS operation with a constant electricity price, case studies with a time-of-use rate result in demand profiles with new and larger peaks and increased ESS cycling due to non-preferred ESS usage. Nonetheless, across all varying controllable resource scenarios, the HEMS algorithm was always able to lower the electricity cost to the customer with a TOU rate compared to a constant electricity rate.

- **Contribution 2. Stochastic flexible transmission line flow rating algorithm for minimizing wind power curtailment.** A two-stage stochastic optimization model is proposed to determine the optimal conventional generator dispatch while minimizing the amount of curtailed wind power across wind power generation scenarios. Flexible line ratings are incorporated into the model using integer chance constraints, limiting the probability of non-nominal line capacity rating violations across all wind scenarios. This enables the total transmission line capacity in areas of the network experiencing congestion to be temporarily increased to allow larger amounts of wind power generation to be transported to other areas of the network. Simulation results on the RTS-GMLC test system demonstrate that the flexible line rating algorithm can reduce the total average wind power curtailment by 40% compared to the case where the line ratings are static.

- **Contribution 3. Optimality guarantees for relaxed complementarity models in energy systems in behind-the-meter and optimal power flow settings.** A convex relaxation for a commonly used ESS model with a complementarity constraint on charging and discharging is proposed based on a penalty reformulation approach. In this approach, the complementarity constraints are omitted, and a linear penalty term is added to the optimization objective function. In both behind-the-meter and optimal power flow settings, the theoretical analysis provided guarantees the relaxed convex ESS model produces an optimal control strategy with proper ESS behavior, i.e., solutions with simultaneous charging and discharging are suboptimal. Numerical case study results demonstrate proper ESS behavior when the convex ESS model with the penalty reformulation is used in various grid-connected ESS settings.

1.4 Organization of Thesis

Chapter 2 provides a brief theoretical overview of stochastic optimization methods, optimality guarantees for convex optimization problems, and complementarity constraints. First, the Karush-

Kuhn-Tucker (KKT) optimality conditions for convex optimization problems will be provided and discussed. Then complementarity constraints will be introduced, and common ways of dealing with this type of constraints will be discussed. Within stochastic optimization methods, chance constrained optimization and two-stage stochastic optimization methods are discussed. Lastly, model predictive control (MPC) is briefly introduced.

Chapter 3 presents two stochastic MPC-based optimization models for a home energy management system (HEMS) algorithm that optimally coordinates appliances, customer preferences, and behind-the-meter resources such as photovoltaic (PV) generation and electrical energy storage. The first chance constrained optimization model captures a situation where the HEMS communicates with a utility company to accommodate a demand response (DR) request. The second stochastic optimization model captures a varying set of controllable behind-the-meter appliances and renewable energy resources under different electricity rates. For both models, a case study is provided and the performance of the algorithm is measured using both customer-focused and utility-focused metrics.

Chapter 4 presents a two-stage stochastic optimal power flow model to account for fluctuations in wind power generation that includes flexible transmission line capacity ratings to minimize wind power curtailment. Traditional transmission line capacity ratings are discussed, and the integer chance constraint used to enforce the flexible ratings is derived. A case study on the three-area RTS-GMLC test system is presented to demonstrate the flexible line capacity optimization model and the resulting reduction in wind power curtailment.

Chapter 5 first provides convex relaxations of models found in energy systems that include non-convex complementarity constraints. In particular, we are mainly concerned with grid-connected electrical ESS models. Then, theoretical optimality guarantees and the associated proofs are presented for the convex relaxations. The optimality guarantees are proven in a behind-the-meter setting and in a linear power flow approximation (DC OPF). For each setting, numerical case studies illustrate that proper model behavior is observed in simulations of the convex relaxed models. Lastly, Chapter 6 discusses the main conclusions of this thesis, as well as areas of possible

future work.

Portions of this work have been presented in other publications by the author. Chapter 3 material is presented in [17] and [18]. Chapter 4 is based on [19]. Chapter 5 consists of work from [20] and [21].

Table 1.1: Services that grid-connected energy storage systems (ESSs) can provide and the levels at which they can be provided.

Services	Transmission	Distribution	Customer
Electric Energy Arbitrage ESSs can be used to store energy that was purchased at a low price, and sold back during periods of high electricity prices.	X	X	X
Reserve Capacity ESSs can serve as reserve capacity that can satisfy loads during contingencies or unexpected outages.	X	X	
Frequency and Voltage Support ESSs can help maintain grid frequency and voltage within an acceptable range to maintain grid stability.	X	X	
Black Start ESSs can act as an asset when bringing power plants back online after an outage.	X	X	
Upgrade Deferrals and Increased Supply Capacity ESSs can be used to act as generation capacity to delay, reduce, or avoid investments in new generation capacity to meet projected electricity demand growth.	X	X	
Power Balancing and Ramping Support ESSs can help balance momentary differences caused by fluctuations in generation and electricity demand. Also, ESSs can respond quickly to steep ramps in net load caused by renewable energy availability.	X	X	
Congestion Relief ESSs can be used to serve loads downstream of congested transmission corridors, typically during times of high electricity demand, to minimize congestion in the system.	X	X	
Power Quality and Reliability ESSs can quickly respond to short-duration events that impact power quality and reliability, i.e., local variations in voltage and frequency, or service interruptions.		X	X
Demand Charge and Bill Management ESSs can be used to minimize electricity bills by storing electricity bought during times of low prices to be used during times when prices are high, i.e., TOU prices.			X
Increased PV Self-Consumption ESSs can be used to store solar electricity generated BTM for local consumption.			X

Chapter 2

A Brief Introduction to Optimization Theory, Complementarity Constraints, and Stochastic Optimization

In this chapter, the theoretical background in optimization and control is provided. First, the Karush-Kuhn-Tucker conditions will be introduced for a general optimization problem. Following the discussion on optimality conditions, we introduce optimization problems with complementarity constraints and discuss the approaches often used to solve this type of problem. Then, the stochastic optimization methods used in this dissertation are introduced, in particular, we introduce chance (or probability) constrained optimization and two-stage stochastic optimization. Lastly, we present a brief introduction to model predictive control (MPC). The topics explained in this chapter will facilitate the contributions of this thesis presented in Chapters 3, 4, and 5.

2.1 Karush-Kuhn-Tucker Optimality Conditions for Convex Problems

In this section, we introduce the Karush-Kuhn-Tucker (KKT) conditions for a general optimization problem. First, consider an optimization problem where the functions $f : \mathbb{R}^n \to \mathbb{R}$, $g_i : \mathbb{R}^n \to \mathbb{R}$, and $h_j : \mathbb{R}^n \to \mathbb{R}$ are differentiable for all $i \in \{1, \ldots, I\}$ and $j \in \{1, \ldots, J\}$:

$$
\begin{aligned}
(\mathcal{P}) \qquad & \min_{\mathbf{x} \in \mathcal{X}} && f(\mathbf{x}) && && (2.1a)\\
& \text{subject to} && g_i(\mathbf{x}) \leq 0, && \forall i \in \{1, \ldots, I\}, && (2.1b)\\
& && h_j(\mathbf{x}) = 0, && \forall j \in \{1, \ldots, J\}, && (2.1c)
\end{aligned}
$$

where $\mathbf{x} \subseteq \mathbb{R}^n$ and the set of feasible solutions $\mathbf{x} \in \mathcal{X}$ is nonempty. Next, let $\boldsymbol{\lambda} = [\lambda_1, \ldots, \lambda_I]$ denote the vector of Lagrange multipliers corresponding to the inequality constraints in (2.1b) and let $\boldsymbol{\mu} = [\mu_1, \ldots, \mu_J]$ denote the vector of Lagrange multipliers corresponding to the equality constraints in (2.1c). The Lagrange multipliers are also referred to as the dual variables. Then let $\mathbf{x}^*$ denote an optimal primal solution and let $\boldsymbol{\lambda}^*, \boldsymbol{\mu}^*$ denote optimal solutions to the dual problem with zero duality gap (see [22,23] for more details on the dual problem). Then for any optimization problem of the form $(\mathcal{P})$, an optimal solution $(\mathbf{x}^*, \boldsymbol{\lambda}^*, \boldsymbol{\mu}^*)$ must satisfy:

$$\text{Primal Feasibility:} \quad g_i(\mathbf{x}^*) \leq 0, \quad \forall i \in \{1, \ldots, I\}, \tag{2.2a}$$

$$h_j(\mathbf{x}^*) = 0, \quad \forall j \in \{1, \ldots, J\}, \tag{2.2b}$$

$$\text{Dual Feasibility:} \quad \lambda_i^* \geq 0, \quad \forall i \in \{1, \ldots, I\}, \tag{2.2c}$$

$$\text{Complementary Slackness:} \quad \lambda_i^* g_i(\mathbf{x}^*) = 0, \quad \forall i \in \{1, \ldots, I\}, \tag{2.2d}$$

$$\text{Stationarity:} \quad \nabla f(\mathbf{x}^*) + \sum_{i=1}^{I} \lambda_i^* \nabla g_i(\mathbf{x}^*) + \sum_{j=1}^{J} \mu_j^* \nabla h_j(\mathbf{x}^*) \in 0, \tag{2.2e}$$

which are known as the KKT conditions [22, 23]. When the problem $(\mathcal{P})$ in (2.1) is convex, the KKT conditions in (2.2) are sufficient for showing $\mathbf{x}^*$ is a minimizer of $(\mathcal{P})$ [22].

The KKT conditions will be used for the theoretical analysis in Chapter 5. In particular, in Chapter 5, we focus on optimization problems with complementarity constraints, which are introduced in the next section.

2.2 Complementarity Constraints in Optimization Problems

Optimization problems with a complementarity constraint, also referred to as mathematical programs with complementarity constraints (MPCCs) in the applied mathematics literature, are used to model many practical engineering and economic problems. In this thesis, we will focus on complementarity constraints that arise in energy system models. Here, we introduce a general optimization problem with complementarity constraints, and motivate why this is an interesting class of problems and how these constraints are typically handled when solving an optimization problem.

Let $\mathbf{x}, \mathbf{y} \in \mathbb{R}^n$, and let $f : \mathbb{R}^{2n} \to \mathbb{R}$, $g_i : \mathbb{R}^{2n} \to \mathbb{R}$, and $h_j : \mathbb{R}^{2n} \to \mathbb{R}$ be convex functions for all $i \in \{1, 2, \ldots, I\}$ and $j \in \{1, 2, \ldots, J\}$. Also let x_k and y_k denote the kth element of $\mathbf{x}$ and $\mathbf{y}$, respectively, where $k \in \{1, \ldots, n\}$. Then, optimization problems with complementarity constraints, denoted $(\mathcal{P}_{cc})$, are of the form

$$
\begin{aligned}
(\mathcal{P}_{cc}) \qquad & \min_{\mathbf{x},\mathbf{y} \in \mathcal{X}} && f(\mathbf{x}, \mathbf{y}) && && \text{(2.3a)} \\
& \text{subject to} && g_i(\mathbf{x}, \mathbf{y}) \leq 0, && \forall i \in \{1, 2, \ldots, I\}, && \text{(2.3b)} \\
& && h_j(\mathbf{x}, \mathbf{y}) = 0, && \forall j \in \{1, 2, \ldots, J\}, && \text{(2.3c)} \\
& && x_k \cdot y_l = 0,\ x_k \geq 0,\ y_l \geq 0, && \forall (k, l) \in \mathcal{Z}, && \text{(2.3d)}
\end{aligned}
$$

where the set $\mathcal{Z} \subseteq \{1, 2, \ldots, n\}^2$ collects all pairs (k, l) for which the complementarity condition in (2.3d) is enforced. The nonlinear, non-convex complementarity constraint in (2.3d) is an analytic expression for a logical condition which enforces that for a pair of variables x_k, y_l, $x_k \geq 0$, $y_l \geq 0$, it must be that both x_k and y_l cannot be simultaneously non-zero for all $(k, l) \in \mathcal{Z}$ [24–29]. The nonlinear complementarity constraint in (2.3d) renders $(\mathcal{P}_{cc})$, an otherwise convex optimization problem, non-convex.

To further understand the computational challenges posed by the disjunctive and non-convex features of the complementarity constraint in (2.3d), we next introduce the Mangasarian-Fromowitz constraint qualification (MFCQ) in nonlinear programming. Consider the general optimization problem $(\mathcal{P})$ in (2.1), and define the set $A(\mathbf{x}) := \{i \mid g_i(\mathbf{x}) = 0,\ i \in \{1, \ldots, I\}\}$. For the MFCQ to hold at a feasible point $\mathbf{x}$, both of the following must be satisfied [23, 29, 30]:

(1) $\nabla_{\mathbf{x}} h_j(\mathbf{x})$ are linearly independent for all $j \in \{1, \ldots, J\}$,

(2) there exists a vector $p \in \mathbb{R}^n$ such that $\nabla_{\mathbf{x}} g_i(\mathbf{x})^{\mathrm{T}} p < 0$ for all $i \in A(\mathbf{x})$ and $\nabla_{\mathbf{x}} h_j(\mathbf{x})^{\mathrm{T}} p = 0$ for all $j \in \{1, \ldots, J\}$.

Thus, the MPCC given in (2.3), $(\mathcal{P}_{cc})$, violates the MFCQ at any feasible point. As a consequence, most of the classic non-linear programming theory cannot be applied to MPCCs. For example, the constraints for MPCCs are not regular resulting in unstable numerical behavior for algorithms based

on constraint linearizations, such as sequential quadratic programming (SQP) methods [24,25]. This highlights that the classic nonlinear optimization methods are often insufficient for dealing with complementarity constraints [24, 25, 27, 29].

Numerical solution methods for solving MPCCs that guarantee convergence and efficient practical performance often use relaxation approaches and regularization techniques based on an exact penalty reformulation [24, 25, 27, 28, 31]. A standard penalty reformulation of $(\mathcal{P}_{cc})$ in (2.3) is:

$$
\begin{aligned}
(\mathcal{P}_{cc}^{\text{pen}}) \qquad & \min_{\mathbf{x},\mathbf{y}\in\mathcal{X}} && f(\mathbf{x},\mathbf{y}) + \rho \sum_{(k,l)\in\mathcal{Z}} x_k y_l && && \text{(2.4a)}\\
& \text{subject to} && g_i(\mathbf{x},\mathbf{y}) \leq 0, && \forall i \in \{1,2,\ldots,I\}, && \text{(2.4b)}\\
& && h_j(\mathbf{x},\mathbf{y}) = 0, && \forall j \in \{1,2,\ldots,J\}, && \text{(2.4c)}\\
& && x_k \geq 0,\, y_l \geq 0, && \forall (k,l) \in \mathcal{Z}, && \text{(2.4d)}
\end{aligned}
$$

where $\rho > 0$ is the penalty parameter. For some structured classes of objective functions $f(\mathbf{x},\mathbf{y})$ and some set of parameters $\rho > 0$, this leads to a convex problem. Then, $(\mathcal{P}_{cc}^{\text{pen}})$ is iteratively solved for increasing values of ρ until $\sum_{(k,l)\in\mathcal{Z}} x_k y_l < \epsilon$, where ϵ is some small tolerance (e.g., 1e-04) [28]. In [29], a penalty reformulation of an optimization problem with complementarity constraints is proposed for using smooth nonlinear programming algorithms, in particular sequential quadratic programming (SQP) algorithms. In [31], the authors use a penalty reformulation, in addition to reformulating the complementarity constraint as a system of "semismooth" equations, to achieve a globally convergent SQP algorithm for solving MPCCs.

Another common approach to solve models that have non-convex complementarity constraints is reformulating the problem as a $\{0,1\}$ mixed integer problem and solving such problems using mixed integer solvers [26], which can be computationally limiting for large optimization problems. However, we propose a convex relaxation of $(\mathcal{P}_{cc})$ in (2.3) since an optimal solution to a convex model is guaranteed to be a global minimum, and also, convex problems are often computationally tractable. Thus, in Chapter 5, we propose a specific linear penalty reformulation for complemen-

tarity constraints that occur in energy system models and prove that the resulting relaxed convex energy system model only produces optimal solutions that satisfy the original complementarity constraint.

2.3 Stochastic Optimization Methods

Stochastic optimization seeks to determine an optimal control strategy given some objective function subject to uncertainty in either the constraint set or the objective function. Stochastic optimization methods are commonly used to account for the fluctuating and intermittent nature of renewable energy generation in power grid research. The authors of [32] provide a recent survey of stochastic optimization methods used in power systems research. In this section, we provide an overview of the stochastic optimization methods employed in this dissertation. First, chance constrained optimization is introduced, with some key results that will be leveraged in the work presented in Chapters 3 and 4. Then, sampling-based stochastic optimization methods are presented, followed by the sample average approximation (SAA) for integer chance constraints, which are used in Chapter 4.

2.3.1 Chance Constrained Optimization

Chance constrained programming, i.e., determining a solution to an optimization problem that satisfies stochastic constraints with some prescribed probability, was first introduced in [33–35]. Since then, chance constrained optimization has been proposed for many engineering applications. Within power system optimization, chance constraints have been proposed in optimal power flow settings [36–38], behind-the-meter settings [17, 18, 39, 40], transmission planning and line capacity limits [41–46], and energy storage sizing [47], among many others, which are of particular interest in this dissertation. Here, we provide a brief introduction to chance constrained optimization.

Consider the following general chance constrained problem [48, 49]:

$$\min_{\mathbf{x}\in\mathcal{X}} \quad f(\mathbf{x}) \tag{2.5a}$$

$$\text{subject to} \quad g_i(\mathbf{x}) \leq 0, \qquad \forall i \in \{1, 2, \ldots, I\}, \tag{2.5b}$$

$$h_j(\mathbf{x}) = 0, \qquad \forall j \in \{1, 2, \ldots, J\}, \tag{2.5c}$$

$$\Pr(G_k(\mathbf{x}, \xi) \leq 0) \geq 1 - \epsilon, \qquad \forall k \in \{1, 2, \ldots, K\}, \tag{2.5d}$$

where $\mathcal{X} \subseteq \mathbb{R}^n$ is a nonempty convex set, $\epsilon \in (0, 1)$, the functions $f : \mathbb{R}^n \to \mathbb{R}$, $g_i : \mathbb{R}^n \to \mathbb{R}$, and $h_j : \mathbb{R}^n \to \mathbb{R}$ are convex for all $i \in \{1, \ldots, I\}$ and $j \in \{1, \ldots, J\}$, ξ is a random vector with probability distribution P supported on set $\Xi \subset \mathbb{R}^d$, $G_k(\mathbf{x}, \xi) : \mathbb{R}^n \times \Xi \to \mathbb{R}$ for all $k \in \{1, \ldots, K\}$ is a function of a random variable, and $\Pr(A)$ denotes the probability of event A. Constraints of the form in (2.5d) are referred to as chance (or probabilistic) constraints. Chance constraints represent the condition that the inequality constraint $G_k(\mathbf{x}, \xi) \leq 0$ must be satisfied with some prescribed probability $1 - \epsilon$ for each $k \in \{1, \ldots, K\}$. Note that ϵ is usually a small number (e.g., 0.05). In this thesis, the chance constraint will be used in both a BTM energy management system setting (Chapter 3) and within transmission grid operation to account for uncertainty in renewable energy integration (Chapter 4).

The chance constraint in (2.5d) can present many computational challenges. In particular, even when $G_k(\mathbf{x}, \xi)$ is affine in both $\mathbf{x}$ and ξ for all $k \in \{1, \ldots, K\}$, the feasible set of this constraint may still be non-convex depending on the distribution of ξ [48]. One way to handle the potential non-convexity of the chance constraint is to use a sampling-based approach since it is distribution agnostic. We discuss sampling-based approaches further in Section 2.3.2. Alternatively, the authors of [48] propose conservative convex approximations to replace the chance constraint in problems of the form (2.5).

However, there are distributions of ξ where the feasible set of $G_k(\mathbf{x}, \xi) \leq 0$ is convex for all $k \in \{1, \ldots, K\}$. Prékopa showed that if the functions $G_k(\mathbf{x}, \xi)$ are quasi-concave for all $k \in \{1, \ldots, K\}$ and ξ has a continuous distribution with a logarithmically concave (or log-concave) probability density, then the set $\mathbf{x}$ that satisfies (2.5d) is convex [49, Theorem 10.2.1]. Note that

many common distributions satisfy the log-concavity requirement, such as the multivariate Normal distribution, the exponential distribution on $\mathbb{R}^n_+$, and the Wishart distribution [22].

When ξ is a random vector with a Normal probability density, then the set of $\mathbf{x} \in \mathbb{R}^n$ that satisfy (2.5d) is the same as those satisfying

$$\mu^{\mathrm{T}}\mathbf{x} + \Phi^{-1}(1-\epsilon)\sqrt{\mathbf{x}^{\mathrm{T}}\Sigma\mathbf{x}} \leq 0, \tag{2.6}$$

where the vector μ is the expected value of ξ, i.e., $\mathbb{E}[\xi]$, Σ is the covariance of the random vector ξ, and $\Phi^{-1}(1-\epsilon)$ is the inverse cumulative distribution function (CDF) of the standard Normal distribution $\mathcal{N}(0,1)$ at the fixed probability $1-\epsilon$ [49, Theorem 10.4.1]. When ξ is a random vector with a Normal probability density and $\epsilon \leq \frac{1}{2}$, then the set of vectors satisfying (2.5d) is convex [49, Corollary 10.4.2]. In Chapter 3, we use (2.6) to obtain a convex reformulation for a chance constrained energy management system optimization framework.

2.3.2 Two-Stage Stochastic Optimization

One general way to formulate computationally tractable stochastic optimization problems is to adopt a scenario-based approach [48, 50–52]. The main advantage of this approach is that it does not limit the distribution of the random variable; it only requires being able to sample from the distribution.

Consider the functions $f : \mathbb{R}^n \to \mathbb{R}$, $g_i : \mathbb{R}^n \to \mathbb{R}$, and $h_j : \mathbb{R}^n \to \mathbb{R}$ for all $i \in \{1, \ldots, I\}$ and $j \in \{1, \ldots, J\}$ and let $\mathbf{x} \in \mathbb{R}^n$ and $\mathbf{y} \in \mathbb{R}^m$ be vectors of the first and second stage variables, respectively. Let $\Xi \in \mathbb{R}^d$ denote the support of probability distribution of ξ. Then, define the functions $\hat{f} : \mathbb{R}^m \to \mathbb{R}$, $G_{i'} : \mathbb{R}^n \times \mathbb{R}^m \times \Xi \to \mathbb{R}$, and $H_{j'} : \mathbb{R}^n \times \mathbb{R}^m \times \Xi \to \mathbb{R}$ for all $i' \in \{1, \ldots, I'\}$ and $j' \in \{1, \ldots, J'\}$. In two-stage stochastic programming, we first determine the first stage variables. Then after observing uncertainty ξ, the second stage variables are decided given the decisions in the first stage. In this thesis, we are mainly concerned with observing uncertainty in renewable energy generation over some planning horizon, which impacts the first-stage dispatch decision for conventional generators. Let $\mathbb{E}[X]$ denote the expectation of X. Then, the two-stage

stochastic optimization problem is given by [50–52]:

$$\min_{\mathbf{x}} \quad f(\mathbf{x}) + \mathbb{E}[F(\mathbf{x}, \xi)] \tag{2.7a}$$

$$\text{subject to} \quad g_i(\mathbf{x}) \leq 0, \qquad \forall i \in \{1, 2, \ldots, I\}, \tag{2.7b}$$

$$h_j(\mathbf{x}) = 0, \qquad \forall j \in \{1, 2, \ldots, J\}, \tag{2.7c}$$

where $F(\mathbf{x}, \xi)$ is the optimal value of the second stage problem:

$$F(\mathbf{x}, \xi) \quad = \min_{\mathbf{y}} \quad \hat{f}(\mathbf{y}) \tag{2.8a}$$

$$\text{subject to} \quad G_{i'}(\mathbf{x}, \mathbf{y}, \xi) \leq 0 \qquad \forall i' \in \{1, \ldots, I'\}, \tag{2.8b}$$

$$H_{j'}(\mathbf{x}, \mathbf{y}, \xi) = 0 \qquad \forall j' \in \{1, \ldots, J'\}, \tag{2.8c}$$

To obtain a scenario-based approach for solving the above two-stage problem in (2.7), we assume the random vector ξ has finite support and that $\omega \in \Omega$ index the realizations (called scenarios) of ξ, each with probability p_ω. Then the deterministic form of the problem in (2.7) can be written as [50–52]:

$$\min_{\mathbf{x}} \quad f(\mathbf{x}) + \sum_{\omega=1}^{N} p_\omega F(\mathbf{x}, \xi(\omega)) \tag{2.9a}$$

$$\text{subject to} \quad g_i(\mathbf{x}) \leq 0, \qquad \forall i \in \{1, 2, \ldots, I\}, \tag{2.9b}$$

$$h_j(\mathbf{x}) = 0, \qquad \forall j \in \{1, 2, \ldots, J\}, \tag{2.9c}$$

$$G_{i'}(\mathbf{x}, \mathbf{y}, \xi(\omega)) \leq 0 \qquad \forall i' \in \{1, \ldots, I'\}, \forall \omega \in \Omega, \tag{2.9d}$$

$$H_{j'}(\mathbf{x}, \mathbf{y}, \xi(\omega)) = 0 \qquad \forall j' \in \{1, \ldots, J'\}, \forall \omega \in \Omega. \tag{2.9e}$$

When the two-stage stochastic optimization problem is formulated in its deterministic form as in (2.9), depending on the size of the problem (determined by the number of scenarios N and the size of $\mathbf{x}$) and the degree of the functions, solving (2.9) may be computationally limiting. In these cases, decomposition methods such as Dantzig-Wolfe and Benders decomposition may be used [50, 51]. However, the two-stage stochastic optimization we consider in Chapter 4 is a mixed-integer linear program that is small enough such that we are able to solve the extensive form of the problem.

2.3.3 Integer Chance Constraints

In Chapter 4, the two-stage stochastic optimization model we propose includes an integer joint chance constraint on a second stage variable, i.e., a decision variable in the sample space Ω, which we refer to as the set of scenarios. Thus, in this section, we derive the sample average approximation (SAA) of a joint chance constraint. The SAA results in a deterministic approximation of the joint chance constraint that can be included as a constraint in an optimization problem.

Motivated by [46, 53], we first introduce some nomenclature. Define the following:

$$E_t = \{\omega \in \Omega : \ y_{\omega,t} = 0\}, \quad \forall t \in \mathcal{T}, \tag{2.10a}$$

$$E_t^{\mathrm{C}} = \{\omega \in \Omega : \ y_{\omega,t} = 1\}, \quad \forall t \in \mathcal{T}, \tag{2.10b}$$

$$F = \bigcap_{t \in \mathcal{T}} E_t, \tag{2.10c}$$

$$F^{\mathrm{C}} = \bigcup_{t \in \mathcal{T}} E_t^{\mathrm{C}}, \tag{2.10d}$$

where $(\cdot)^{\mathrm{C}}$ denotes the complement, event E_t is a set of scenarios such that $y_{\omega,t} = 0$ at time $t \in \mathcal{T}$, and event E_t^{C} is the complement. Then F is a collection of scenarios in the intersection of E_t for all $t \in \mathcal{T}$, and F^{C} is collection of scenarios in the union of E_t^{C}. Then, in this dissertation, we are interested in the following joint chance constraint:

$$\Pr(F^{\mathrm{C}}) \leq \epsilon, \tag{2.11}$$

where $0 < \epsilon < 1$, which will be the focus of the following SAA derivation based on [46]. Using the union bound, we have:

$$\Pr(F^{\mathrm{C}}) = \Pr\left(\bigcup_{t \in \mathcal{T}} E_t^{\mathrm{C}}\right) \leq \sum_{t \in \mathcal{T}} \Pr\left(E_t^{\mathrm{C}}\right),$$

so the following inequality constraint:

$$\sum_{t \in \mathcal{T}} \Pr\left(E_t^{\mathrm{C}}\right) \leq \epsilon, \tag{2.12}$$

will imply (2.11). Next, we seek the SAA of the chance constraints in (2.11) and (2.12) for a two-stage stochastic optimization problem with $|\Omega|$ scenarios. To do this, first define a new binary

variable $z_\omega \in \{0,1\}$ where

$$z_\omega = \begin{cases} 0, & \omega \in F, \\ 1, & \omega \in F^{\mathrm{C}}. \end{cases} \tag{2.13}$$

Then we relate the variables z_ω and $y_{\omega,t}$ with the equations:

$$z_\omega \leq \sum_{t\in\mathcal{T}} y_{\omega,t}, \quad \forall \omega \in \Omega \tag{2.14a}$$

$$y_{\omega,t} \leq z_\omega, \quad \forall t \in \mathcal{T}, \forall \omega \in \Omega. \tag{2.14b}$$

Using the new variables z_ω together with (2.14), we plug these into (2.11) and (2.12) to obtain the following SAA of (2.11) and (2.12), respectively:

$$\frac{1}{|\Omega|}\sum_{\omega\in\Omega} z_\omega \leq \epsilon, \tag{2.15a}$$

$$\frac{1}{|\Omega|}\sum_{\omega\in\Omega}\sum_{t\in\mathcal{T}} y_{\omega,t} \leq \epsilon. \tag{2.15b}$$

Then, notice that (2.14) and (2.15) imply

$$\frac{1}{|\Omega|}\frac{1}{|\mathcal{T}|}\sum_{\omega\in\Omega}\sum_{t\in\mathcal{T}} y_{\omega,t} \leq \epsilon, \tag{2.16}$$

because $\frac{1}{|\mathcal{T}|}\sum_{t\in\mathcal{T}} y_{\omega,t} \leq z_\omega$ for all $\omega \in \Omega$, which is weaker than (2.15b). Thus, the SAA in (2.16) is the inequality constraint included in the two-stage stochastic optimization problem. Note that (2.16) is an approximation of (2.12) as the name SAA implies. We use this general derivation to aid the presentation of the SAA for an integer chance constraint in Chapter 4.

2.4 Model Predictive Control

Model predictive control (MPC), or receding horizon control, is a control algorithm where an optimal control strategy is determined at each time step t over a finite prediction horizon T_h subject to constraints that define the system dynamics and constraints. MPC is widely used in many engineering applications because after each iteration, updated information (such as updated weather forecasts and electricity demand) can be incorporated into the model.

To aid in the discussion of MPC, consider a generic MPC formulation [54, 55]:

$$\min_{\mathbf{x}_t, \mathbf{u}_t} \quad \sum_{t=1}^{T_h} J(\mathbf{x}_t, \mathbf{u}_t) \tag{2.17a}$$

$$\text{subject to} \quad g_i(\mathbf{x}_t, \mathbf{u}_t) \leq 0, \qquad \forall i \in \{1, \ldots, I\}, \forall t \in \{1, \ldots, T_h\}, \tag{2.17b}$$

$$h_j(\mathbf{x}_t, \mathbf{u}_t) = 0, \qquad \forall j \in \{1, \ldots, I\}, \forall t \in \{1, \ldots, T_h\}, \tag{2.17c}$$

$$\mathbf{x}_{t+1} = f_t(\mathbf{x}_t, \mathbf{u}_t) \qquad \forall t \in \{1, \ldots, T_h - 1\}, \tag{2.17d}$$

where the vectors $\mathbf{x}_t$ and $\mathbf{u}_t$ collect the state decision variables and input decision variables at time t, respectively. The objective function is given in (2.17a). The constraints in (2.17b)-(2.17c) describe the system at each time t in the prediction horizon. With respect to energy systems, the inequality constraints in (2.17b) ensure that various states of the system, such as indoor temperature or capacity of a battery, stay within some prescribed limits for comfort or safety and reliability. In this dissertation, the equality constraint in (2.17c) is used to describe the power balance. Lastly, the constraint in (2.17d) describes the evolution of the state variables over time, which, for example, can be used to describe indoor temperature dynamics and energy storage system state of charge. After each iteration of the MPC algorithm, only the optimal control policy $(\mathbf{x}_1^*, \mathbf{u}_1^*)$ at the first time step is implemented, and the new current state is used as the starting point of the next iteration of the algorithm. Then, the model is moved forward one step in time with updated model parameter information and resolved [54, 55]. Thus, after k iterations of the MPC algorithm, the terminal time is $k + T_h$. In this dissertation, an MPC-based algorithm is used for a behind-the-meter energy management system framework in Chapter 3.

Chapter 3

Stochastic Energy Management Systems

This chapter studies the performance of two chance constrained MPC-based home energy management system (HEMS) algorithms for demand response (DR) that optimally coordinate home appliances, residentially-owned renewable energy resources, and battery energy storage given user comfort preferences, energy cost sensitivity, and uncertainty in available PV generation and outdoor temperature forecast. In both algorithm formulations, chance constraints are included for handling uncertainty in weather forecasts which impact the indoor temperature dynamics and renewable energy generation. The performance of both HEMS algorithms will be demonstrated through a series of case studies.

3.1 Behind-the-Meter Home Energy Management Systems

As mentioned in Section 1.1.1, residential demand-side energy management can be used to partially address stable renewable energy integration since residential buildings account for 37.6% of total electricity consumption in the U.S., which is more than the commercial building sector, industrial building sector, or transportation sector [5]. Home energy management systems (HEMS) provide demand-side energy management by coordinating multiple residential appliances in real-time given user preferences and renewable energy resource forecasts [6, 7]. HEMS can increase the energy efficiency of a home by leveraging controllable residential devices, such as heating, ventilation, and air-conditioning (HVAC) systems, which account for over 50% of total residential load [5]. The authors in [7] survey various HEMS architectures that have been proposed for increasing resi-

dential energy efficiency. Many of the control methods studied for HEMS applications also include DR grid service capabilities such as real-time pricing and direct load control, which encourage consumers to shift the load of flexible devices away from peak demand periods [6, 7]. Typically, advanced HEMS algorithms use optimization techniques such as MPC [6, 56], mixed-integer linear programming (MILP) [57], or various artificial intelligence techniques [7, 58, 59].

In this chapter, two stochastic HEMS algorithms are proposed for optimally coordinating electricity usage within a home. One approach for using stochastic optimal control methods in HEMS algorithms is the use of Monte Carlo sampling for representing uncertainties in various parameters, such as outdoor temperature and renewable energy source generation [60], which can be computationally restrictive. Another approach for incorporating uncertainty in HEMS algorithms is using the Markov chain modeling framework [61]. Instead, we propose a chance constrained MPC-based optimization formulation to include probabilistic models in a HEMS algorithm. Chance constrained optimization has been used to incorporate uncertainty in renewable energy generation into optimal energy storage sizing problems [62] and AC optimal power flow problems [36]. Chance constrained MPC has also been used to include uncertainty in weather forecasts for energy efficient HVAC system usage in buildings [39]. Chance constraints have also been used to incorporate uncertainty in dynamic pricing and system loads in a HEMS [40]. However, in this work we present two chance constrained MPC-based HEMS algorithms to incorporate uncertainty in the weather forecast and renewable energy generation. In the next section, both chance constrained HEMS algorithms are introduced and their performance is studied.

3.2 Stochastic MPC-based HEMS Algorithms

In this section, the overall chance constrained MPC-based HEMS optimization problem is formulated for two different settings. In each setting the chance constraint considering uncertainty in outdoor weather forecasts is derived. We end with a case study demonstrating the performance of the HEMS algorithm for each setting. The notation used in the HEMS formulations introduced in this section is provided in Table 3.1.

Table 3.1: Notation for HEMS optimization models.

	Parameters
β_i	House model parameters
B^{util}	DR reduction request from utility (kW)
c^e	Cost of P_{grid} (\$/kWh)
$\underline{E}^{\text{b}}/\overline{E}^{\text{b}}$	Minimum/maximum energy storage in battery (kWh)
$\underline{E}^{\text{ev}}/\overline{E}^{\text{ev}}$	Minimum/maximum electric vehicle state of charge (kWh)
$\eta^{\text{ch}}/\eta^{\text{dis}}$	Battery charging/discharging efficiency
η^{ev}	Electric vehicle charging/discharging efficiency
T_h	MPC prediction horizon
$\overline{P}^{\text{b}}$	Maximum battery charging/discharging power (kW)
P^{ac}	Power consumed by HVAC when cooling (kW)
$\overline{P}^{\text{ev}}$	Maximum electric vehicle charging power (kW)
P^{pred}	Predicted P_{grid} consumption with no DR (kW)
P^{uc}	Residential load from uncontrollable devices (kW)
ϵ	Probability that chance constraint is satisfied, $\epsilon \in (0, 1)$
$t^{\text{DR,f}}$	End time of DR period
$t^{\text{DR,n}}$	Time of DR notice
$t^{\text{DR,s}}$	Start time of DR period
$\underline{T}/\overline{T}$	Minimum/maximum indoor air temperature (°F)
	Random Variables
P^{sol}	Available solar power (kW)
T^{out}	Outdoor air temperature (°F)
P^{rad}	Solar Irradiance (W/m^2)
	Decision Variables
d^{hvac}	HVAC control signal (duty cycle)
E^{b}	Battery state of charge (kWh)
E^{ev}	Electric vehicle state of charge (kWh)
P^{curt}	PV curtailment (percent)
P^{ch}	Power injected into battery storage (kW)
P^{dis}	Power drawn from battery storage (kW)
P^{ev}	Power for charging the electric vehicle (kW)
P^{grid}	Power consumed from the grid (kW)
T^{in}	Indoor air temperature (°F)

3.2.1 HEMS with Utility Demand Response Communication

In this section, we provide a chance constrained MPC algorithm for a HEMS capable of satisfying grid DR requests where the use of flexible (i.e., controllable) devices, such as HVAC systems, are shifted away from peak demand periods on the power grid. We assume the DR event is communicated to the HEMS before the DR period begins in the form of a request for some amount of grid power reduction B_{util} relative to the amount of grid power the HEMS predicts the home

requires during the DR period. We consider a HEMS that coordinates a residentially-owned PV array and home battery system (HBS), an HVAC system, and uncontrollable devices. We assume uncontrollable residential devices, such as lighting, television, and plug loads, cannot be controlled with the HEMS. The chance constraints in the HEMS algorithm are used to ensure that both the DR reduction request and the users' thermal comfort are satisfied with high probability given uncertainty in available PV power and outdoor air temperature during the DR period. An overview of the considered HEMS system is shown in Fig. 3.1. This work is based on the published results in [17]; however, minor modifications to the formulation have been made to ensure consistency with results presented later in this thesis.

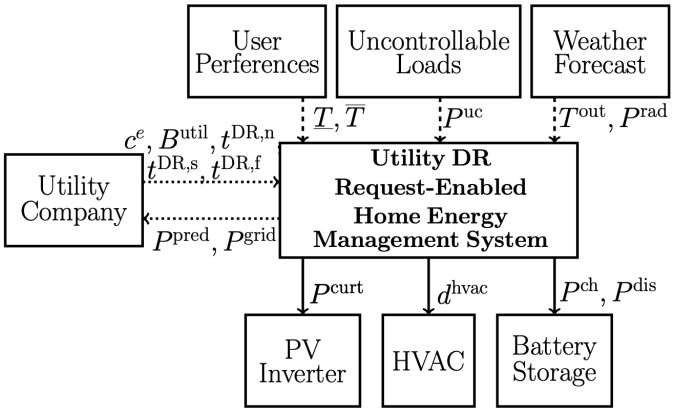

Figure 3.1: Control and data schematic for HEMS with utility demand response communication.

3.2.1.1 Optimization Formulation

Here, we provide the overall chance constrained MPC optimization model for the HEMS algorithm. Let the vectors $\mathbf{u}_t = [P_t^{\text{grid}}, P_t^{\text{curt}}, d_t^{\text{hvac}}, P_t^{\text{ch}}, P_t^{\text{dis}}]$ and $\mathbf{x}_t = [T_t^{\text{in}}, E_t^{\text{b}}]$ be the collection of decision variables and state variables, respectively, at time $t \in \mathcal{T}$ where $\mathcal{T} = \{1, \ldots, T_h\}$. Then,

the overall chance constrained MPC-based convex optimization problem is the following:

$$\min_{\{\mathbf{x}_t,\mathbf{u}_t\}_{t=1}^{T_h}} \sum_{t=1}^{T_h}(c^e P_t^{\text{grid}} + \alpha P_t^{\text{ch}}) \tag{3.1a}$$

$$\text{s.t. } 0 \le P_t^{\text{grid}}, \qquad \forall t \in \mathcal{T}, \tag{3.1b}$$

$$0 \le P_t^{\text{curt}} \le P_t^{\text{sol}}, \qquad \forall t \in \mathcal{T}, \tag{3.1c}$$

$$T_{t+1}^{\text{in}} = T_t^{\text{in}} + \beta_1(T_t^{\text{out}} - T_t^{\text{in}}) - \beta_2 d_t^{\text{hvac}} + \beta_3 P_t^{\text{rad}}, \qquad \forall t \in \mathcal{T}, \tag{3.1d}$$

$$0 \le d_t^{\text{hvac}} \le 1, \qquad \forall t \in \mathcal{T}, \tag{3.1e}$$

$$\underline{T}_{t+1} \le T_{t+1}^{\text{in}} \le \overline{T}_{t+1}, \qquad \forall t \notin \{t^{\text{DR,s}}, t^{\text{DR,f}}\}, \tag{3.1f}$$

$$\Pr(\underline{T}_{t+1} - T_{t+1}^{\text{in}} \le 0) \ge 1 - \epsilon^{\underline{T}}, \qquad \forall t \in \{t^{\text{DR,s}}, t^{\text{DR,f}}\}, \tag{3.1g}$$

$$\Pr(T_{t+1}^{\text{in}} - \overline{T}_{t+1} \le 0) \ge 1 - \epsilon^{\overline{T}}, \qquad \forall t \in \{t^{\text{DR,s}}, t^{\text{DR,f}}\}, \tag{3.1h}$$

$$P_t^{\text{grid}} + (P_t^{\text{sol}} - P_t^{\text{curt}}) + P_t^{\text{dis}} - P_t^{\text{uc}} - P^{\text{ac}} d_t^{\text{hvac}} - P_t^{\text{ch}} = 0, \qquad \forall t \in \mathcal{T}, \tag{3.1i}$$

$$E_{t+1}^{\text{b}} = E_t^{\text{b}} + \eta^{\text{ch}} P_t^{\text{ch}} \Delta t - \tfrac{1}{\eta^{\text{dis}}} \Delta t P_t^{\text{dis}}, \qquad \forall t \in \mathcal{T}, \tag{3.1j}$$

$$\underline{E}^{\text{b}} \le E_{t+1}^{\text{b}} \le \overline{E}^{\text{b}}, \qquad \forall t \in \mathcal{T}, \tag{3.1k}$$

$$0 \le P_t^{\text{dis}} \le \overline{P}^{\text{b}}, \qquad \forall t \in \mathcal{T}, \tag{3.1l}$$

$$0 \le P_t^{\text{ch}} \le \overline{P}^{\text{b}}, \qquad \forall t \in \mathcal{T}, \tag{3.1m}$$

$$\Pr\left(\sum_{t=t^{\text{DR,s}}}^{t^{\text{DR,f}}} P_t^{\text{grid}} - \sum_{t=t^{\text{DR,s}}}^{t^{\text{DR,f}}} P_t^{\text{pred}} + B^{\text{util}} \le 0\right) \ge 1 - \epsilon^{\text{DR}}, \quad \forall t \in \{t^{\text{DR,n}}, t^{\text{DR,f}}\}. \tag{3.1n}$$

The objective function in (3.1a) minimizes the cost of electricity drawn from the grid and has a small penalty on battery usage to capture future replacement costs, where $\alpha = 0.01$ in this work. The constraint in (3.1b) enforces that excess PV generation, i.e., PV generation when the battery is fully charged and all HVAC and uncontrollable loads have been met, cannot be exported to the grid. Note that this equation can be omitted in a situation where there is net metering or feed-in tariffs. Equation (3.1c) limits PV curtailment by the amount of PV generation available. The indoor temperature dynamics model is given in (3.1d), where β_1 represents the building envelope coefficient, β_2 is the cooling gain coefficient, and β_3 is the solar gain coefficient. The limits on the HVAC duty cycle (for cooling) are enforced in (3.1e). Outside the DR period, the

indoor temperature comfort bound is enforced by (3.1f). Notice that the thermal comfort bounds $[\underline{T}_{t+1}, \overline{T}_{t+1}]$ are time-varying to allow the thermal comfort band to be relaxed during times when the home is unoccupied. During the DR period, the chance constraints in (3.1g)-(3.1h) enforce that the upper and lower thermal comfort bounds must be satisfied with a high probability $1-\epsilon^{\overline{T}}$ and $1-\epsilon^{\underline{T}}$, respectively, given uncertainty in the outdoor air temperature forecast, where $\epsilon^{\overline{T}}$ and $\epsilon^{\underline{T}}$ are small numbers (e.g., $\epsilon^{\overline{T}}, \epsilon^{\underline{T}} \leq 0.1$). The power balance within the home is given in (3.1i). The HBS model is given in (3.1j)-(3.1m). Since proper behavior is guaranteed by the structure of the problem (see Chapter 5), we omit the non-convex complementarity constraint $P_t^{\text{ch}} \cdot P_t^{\text{dis}} = 0$ for $t \in \{1, \ldots, T_h\}$ that ensures non-simultaneous HBS charging and discharging. Lastly, (3.1n) ensures that the DR request, i.e., reducing the predicted residential load by some amount B^{util}, is satisfied with a high probability $1-\epsilon^{\text{DR}}$ given uncertainty in available PV generation, where ϵ^{DR} is a small number (e.g., $\epsilon^{\text{DR}} \leq 0.1$).

3.2.1.2 Derivation of the Chance Constraint

Chance constraints are introduced into the problem to ensure the DR request is satisfied and the user thermal comfort is maintained with high probability given uncertainty in forecasting errors in weather parameters that dictate PV power generation and the indoor air temperature. In this section, we derive a convex reformulation of the chance constraints in (3.1g)-(3.1h) and (3.1n) according to the methods provided in 2.3.1. First, we will focus on the constraint that ensures the DR request is satisfied with probability $1-\epsilon^{\text{DR}}$ in (3.1n), where the actual power drawn from the grid is dictated by the power balance constraint in (3.1i), which is subject to uncertainty in available PV generation. The available PV power can be written as $P_t^{\text{sol}} = P_t^{\text{sol,f}} + P_t^{\text{sol,e}}$, where $P_t^{\text{sol,f}}$ and $P_t^{\text{sol,e}}$ are the solar generation forecast and forecast error at time t, respectively. We assume the solar forecast error $P_t^{\text{sol,e}}$ is Normally distributed $P_t^{\text{sol,e}} \sim \mathcal{N}(\mu_t^{\text{S}}, (\sigma_t^{\text{S}})^2)$ and that $P_t^{\text{sol,e}}$ at different times are independent. Then, we obtain the following expression for P_t^{grid} in (3.1n)

using (3.1i):

$$P_t^{\text{grid}} = P_t^{\text{curt}} - P_t^{\text{sol,f}} - P_t^{\text{sol,e}} + P_t^{\text{uc}} + P^{\text{ac}} d_t^{\text{hvac}} + P_t^{\text{ch}} - P_t^{\text{dis}}. \tag{3.2}$$

Notice that the sum of Normally distributed forecast errors will result in another Normally distributed random variable denoted $P^{\text{sol,e}} \sim \mathcal{N}(\mu^{\text{S}}, \sigma^{\text{S}})$ where $\mu^{\text{S}} = \sum_{t=t_{\text{DR,s}}}^{t_{\text{DR,f}}} \mu_t^{\text{S}}$ and $(\sigma^{\text{S}})^2 = \sum_{t=t_{\text{DR,s}}}^{t_{\text{DR,f}}} (\sigma_t^{\text{S}})^2$. We can then write the constraint in (3.1n) as the following:

$$\Pr\left(G_t^{\text{DR}} \leq 0\right) \geq 1 - \epsilon^{\text{DR}}, \tag{3.3}$$

where G_t^{DR} is given by:

$$G_t^{\text{DR}} = \sum_{t=t^{\text{DR,s}}}^{t^{\text{DR,f}}} P_t^{\text{grid}} + B^{\text{util}} - \sum_{t=t^{\text{DR,s}}}^{t^{\text{DR,f}}} P_t^{\text{pred}}, \tag{3.4}$$

and P_t^{grid} is given by (3.2). Since $P^{\text{sol,e}}$ is Normally distributed, G_t^{DR} is also Normally distributed with the following mean μ^{DR} and standard deviation σ^{DR} given by:

$$\begin{aligned} \mu^{\text{DR}} &= \sum_{t=t^{\text{DR,s}}}^{t^{\text{DR,f}}} (P^{\text{ac}} d_t^{\text{hvac}} + P_t^{\text{uc}} + P_t^{\text{ch}} - P_t^{\text{dis}} - P_t^{\text{sol,f}}) - \mu^{\text{S}} + B^{\text{util}} - \sum_{t=t^{\text{DR,s}}}^{t^{\text{DR,f}}} P_t^{\text{pred}}, \\ \sigma^{\text{DR}} &= \sqrt{(\sigma^{\text{S}})^2}. \end{aligned} \tag{3.5}$$

Therefore, the chance constraint in (3.1n) can be written as:

$$\Pr(G_t^{\text{DR}} \leq 0) = \Phi\left(\frac{0 - \mu^{\text{DR}}}{\sigma^{\text{DR}}}\right) \geq 1 - \epsilon^{\text{DR}}, \tag{3.6}$$

where $\Phi(\cdot)$ is the CDF of the Normal distribution $\mathcal{N}(0, 1)$. The chance constraint that ensures the DR request is satisfied with a high probability is obtained by taking the inverse CDF of both sides of (3.6), which is given by:

$$\sum_{t=t^{\text{DR,s}}}^{t^{\text{DR,f}}} P_t^{\text{pred}} - \sum_{t=t^{\text{DR,s}}}^{t^{\text{DR,f}}} (P^{\text{ac}} d_t^{\text{hvac}} + P_t^{\text{uc}} + P_t^{\text{ch}} - P_t^{\text{dis}} - P_t^{\text{sol,f}}) + \mu^{\text{S}} - B^{\text{util}} \geq \Phi^{-1}(1 - \epsilon_{\text{DR}}) \sqrt{(\sigma^{\text{S}})^2}. \tag{3.7}$$

Thus, the constraint in (3.1n) is replaced with the above convex reformulation in (3.7).

Next, we derive the convex reformulation of the chance constraint in (3.1h) that ensures the thermal comfort upper bound is satisfied with high probability given uncertainty in forecasting

errors in weather parameters that influence indoor air temperature, i.e., P_t^{sol} and P_t^{rad}. First, rewrite (3.1h) as

$$\Pr\left(G_{t+1}^{\overline{T}} \leq 0\right) \geq 1 - \epsilon^{\overline{T}}, \tag{3.8}$$

where $G_{t+1}^{\overline{T}} = T_{t+1}^{\text{in}} - \overline{T}_{t+1}$. For the probabilistic equation in (3.8), write the outdoor temperature as $T_t^{\text{out}} = T_t^{\text{out,f}} + T_t^{\text{out,e}}$, where $T_t^{\text{out,f}}$ is the forecasted outdoor temperature and $T_t^{\text{out,e}}$ is the outdoor temperature forecast error, and similarly write the solar irradiance as $P_t^{\text{rad}} = P_t^{\text{rad,f}} + P_t^{\text{rad,e}}$, where $P_t^{\text{rad,f}}$ is the forecast solar irradiance and $P_t^{\text{rad,e}}$ is the solar irradiance forecast error. Both the outdoor temperature forecast error and solar irradiance error are assumed to be Normally distributed: $T_t^{\text{out,e}} \sim \mathcal{N}(\mu_t^{\text{T}}, (\sigma_t^{\text{T}})^2)$ and $P_t^{\text{rad,e}} \sim \mathcal{N}(\mu_t^{\text{P}}, (\sigma_t^{\text{P}})^2)$ [63]. Then the function $G_{t+1}^{\overline{T}}$ becomes:

$$G_{t+1}^{\overline{T}} = T_t^{\text{in}} + \beta_1(T_t^{\text{out,f}} + T_t^{\text{out,e}} - T_t^{\text{in}}) - \beta_2 d_t^{\text{hvac}} + \beta_3(P_t^{\text{rad,f}} + P_t^{\text{rad,e}}) - \overline{T}_{t+1}. \tag{3.9}$$

Since $T_t^{\text{out,e}}$ and $P_t^{\text{rad,e}}$ are Normally distributed, $G_{t+1}^{\overline{T}}$ is also Normally distributed with the following mean $\mu_t^{\overline{T}}$ and standard deviation $\sigma_t^{\overline{T}}$:

$$\mu_t^{\overline{T}} = T_t^{\text{in}} + \beta_1(T_t^{\text{out,f}} + \mu_t^{\text{T}} - T_t^{\text{in}}) - \beta_2 d_t^{\text{hvac}} + \beta_3(P_t^{\text{rad,f}} + \mu_t^{\text{P}}) - \overline{T}_{t+1}, \tag{3.10a}$$

$$\sigma_t^{\overline{T}} = \sqrt{(\beta_1\sigma_t^{\text{T}})^2 + (\beta_3\sigma_t^{\text{P}})^2}. \tag{3.10b}$$

Therefore, the chance constraint in (3.8) can be written as

$$\Pr(G_{t+1}^{\overline{T}} \leq 0) = \Phi\left(\frac{0 - \mu_t^{\overline{T}}}{\sigma_t^{\overline{T}}}\right) \geq 1 - \epsilon^{\overline{T}}, \tag{3.11}$$

where $\Phi(\cdot)$ is the CDF of the standard Normal distribution $\mathcal{N}(0,1)$. The chance constraint for ensuring the indoor air temperature satisfies the upper bound with probability $(1-\epsilon^{\overline{T}})$ is obtained by taking the inverse CDF of both sides of (3.11):

$$\begin{aligned}\overline{T}_{t+1} - T_t^{\text{in}} - \beta_1(T_t^{\text{out,f}} + \mu_t^{\text{T}} - T_t^{\text{in}}) + \beta_2 d_t^{\text{hvac}} - \beta_3(P_t^{\text{rad,f}} + \mu_t^{\text{P}}) \\ \geq \Phi^{-1}(1-\epsilon^{\overline{T}})\sqrt{(\beta_1\sigma_t^{\text{T}})^2 + (\beta_3\sigma_t^{\text{P}})^2},\end{aligned} \tag{3.12}$$

which replaces (3.1h) in the HEMS formulation in (3.1).

Lastly, we consider the chance constraint in (3.1g). Using the same method and assumptions on the uncertainty in outdoor temperature T_t^{out} and solar irradiance P_t^{rad} as in the derivation of (3.12) above, we obtain the following convex reformulation of (3.1g):

$$T_t^{\text{in}} + \beta_1(T_t^{\text{out,f}} + \mu_t^{\text{T}} - T_t^{\text{in}}) - \beta_2 d_t^{\text{hvac}} + \beta_3(P_t^{\text{rad,f}} + \mu_t^{\text{P}}) - \underline{T}_{t+1} \geq -\Phi^{-1}(1-\epsilon^{\underline{T}})\sqrt{(\beta_1\sigma_t^{\text{T}})^2 + (\beta_3\sigma_t^{\text{P}})^2}. \quad (3.13)$$

Thus, (3.13) replaces (3.1g) in the HEMS formulation in (3.1).

3.2.1.3 Case Study

To demonstrate the proposed HEMS algorithm (3.1), we provide simulation results for DR during a summer afternoon for two different houses. The MATLAB-based solver for disciplined convex programs, CVX, is used in this work [64,65]. For all simulations, we assume the DR request notice is received by the HEMS at 2pm, which is 2 hours before the start of the summer load reduction DR event from 4pm to 6pm, and the DR reduction request needs to be satisfied with probability at least $1-\epsilon^{\text{DR}} = 0.95$ while maintaining the thermal comfort bounds with probability at least $1-\epsilon^{\underline{T}} = 1-\epsilon^{\overline{T}} = 0.95$. The preferred indoor thermal comfort band is $68°\text{F} \leq T_t^{\text{in}} \leq 72°\text{F}$ from 9am to 5pm and restricted to $69°\text{F} \leq T_t^{\text{in}} \leq 71°\text{F}$ otherwise, when the residence is assumed to be occupied. The simulation has a 24 hour prediction horizon with 1 hour time steps.

The device models for both houses are assumed to have the same parameters. The residential PV array size is 20m^2 with a tilt of 30° and an efficiency of 16%. The 5 kWh HBS is restricted to 15% to 85% of the maximum state of charge (SOC) to preserve the battery lifetime [66]. The battery inverter power limit is 3 kW with an inverter efficiency of 95%. The battery charging efficiency η^{ch} and the discharging efficiency is η^{dis} are 95%. The power consumption of the HVAC when cooling P^{ac} is 3 kW. The cost of energy c^e from the grid is assumed to be a flat rate of \$0.11/kWh. The outdoor air temperature and solar irradiance forecasts were obtained from NOAA USCRN data [67].

The proposed HEMS algorithm is simulated for two houses, denoted House 1 and House

Table 3.2: House model parameter values for House 1 and House 2.

Parameter	House 1	House 2
β_1	0.03	0.035
β_2	4	3
β_3	0.000163	0.000326

2, which have different house model parameters given in Table 3.2. The model parameters are designed such that House 2 is a less-insulated version of House 1 and has a less efficient HVAC cooling system, and are based on the parameters learned from the study in [6]. The initial battery SOC is 1.5 kWh and initial indoor temperature is 73°F for both homes. Simulation results include cases when the DR reduction request is $B^{\text{util}} = 0.5$ kW and $B^{\text{util}} = 0.75$ kW. The simulations also include cases for varying uncertainty in the random variables, i.e., $T_t^{\text{out,e}} \sim \mathcal{N}(0, (T^{\text{base}}+0.1(t-1))^2)$ where T^{base} =0.5°F and T^{base} =1.0°F, and $P_t^{\text{rad,e}} \sim \mathcal{N}(0, (P^{\text{base}}+5(t-1))^2)$ where P^{base} =15 W/m^2 and P^{base} =30 W/m^2. We relate P_t^{sol} to P_t^{rad} by the following equation:

$$P_t^{\text{sol}} = \frac{A^{\text{PV}} \eta^{\text{PV}} P_t^{\text{rad}}}{1000},$$

where A^{PV} is area of the rooftop PV panels (m^2) and η^{PV} is the PV efficiency. Thus, we use this relation to obtain the distribution $P_t^{\text{sol,e}} \sim \mathcal{N}\left(0, \left(\frac{(P^{\text{base}}+5(t-1))A^{\text{PV}}\eta^{\text{PV}}}{1000}\right)^2\right)$.

First, we focus on the simulation results for House 1 when B^{util}=0.75 kW, P^{base} =30 W/m^2, and T^{base}=1.0°F, which are shown in Figs. 3.2 and 3.3. In Fig. 3.2, the battery is discharging when $P^{\text{batt}} < 0$ and charging when $P^{\text{batt}} > 0$, the HEMS predicted grid power usage is given by P^{pred}, and the actual grid power usage in the DR event case is denoted P^{grid}. Also, let $P_t^{\text{PV}} = P_t^{\text{sol}} - P_t^{\text{curt}}$ be the actual available usable PV power and let $P^{\text{hvac}} = P^{\text{ac}} d_t^{\text{hvac}}$ be the power required for the HVAC load. From Fig. 3.2, we can see that the battery only charges when the available PV power exceeds the base load of the home (including the HVAC load), and is slowly discharging (supplying power to the home) in the morning hours. During the DR period, the HEMS reduces predicted grid power usage of House 1 by leveraging the stored energy in the battery system. The results shown in Fig. 3.3 (top) demonstrate that the indoor air temperature T_t^{in} stays within the preferred thermal comfort band throughout the simulation, where the outdoor air temperature forecast $T^{\text{out,f}}$

is shown for reference. The battery SOC is shown in Fig. 3.3 (middle), which highlights the usage of energy stored in the battery during the DR period. The battery operation is included in Fig. 3.3 (bottom) to show the battery does not simultaneously charge and discharge.

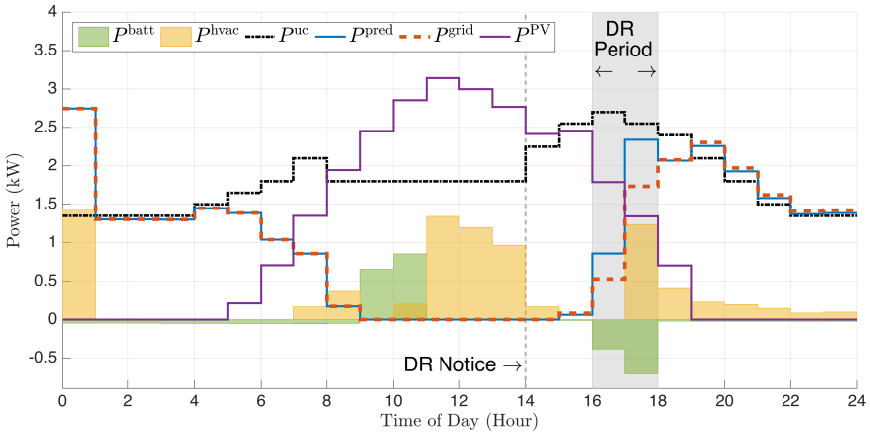

Figure 3.2: Power profiles for House 1 with HEMS algorithm in (3.1) responding to a summer load reduction DR event of $B^{\text{util}} = 0.75$ kW with uncertainty in available PV generation and outdoor air temperature forecast error where P^{base} =30 W/m^2 and T^{base}=1.0°F.

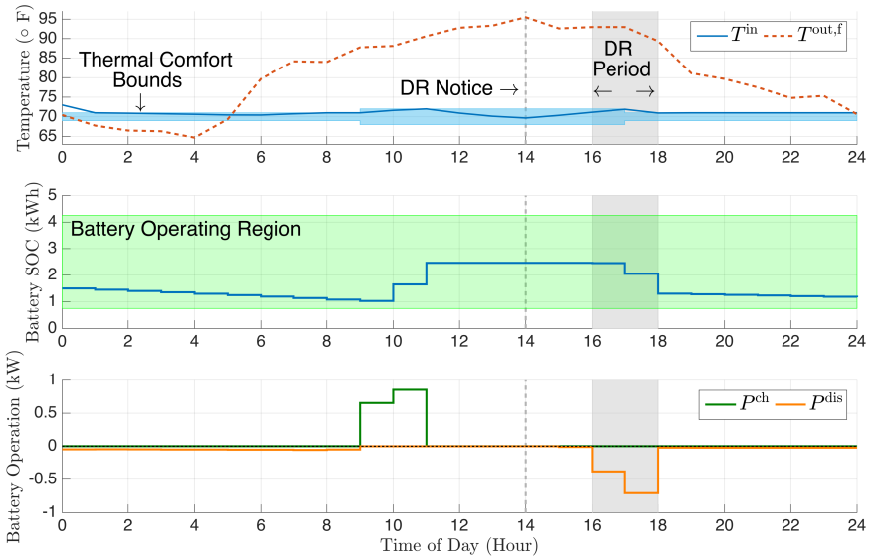

Figure 3.3: House 1 thermal comfort and battery operation results with HEMS algorithm in (3.1) responding to a summer load reduction DR event of $B_{\text{util}} = 0.75$ kW with uncertainty in available PV generation and outdoor air temperature forecast error where P^{base} =30 W/m^2 and T^{base}=1.0°F.

Next, we look at the impact of the house parameters by focusing on the House 2 HEMS simulation results provided in Figs. 3.4 and 3.5. In Fig. 3.4, we see that the HVAC load is much

higher than in House 1 due to House 2's less efficient HVAC system and weaker building envelope. This causes the majority of the available PV generation to be used for the HVAC load instead of charging the battery. After the DR notice occurs, the HEMS in House 2 draws more than the predicted amount of P^{grid} in order to pre-cool the house in order to satisfy the DR request. As in House 1, the HEMS in House 2 leverages the energy stored in the battery during the DR period to reduce the amount of electricity drawn from the grid to meet the DR request. Fig. 3.5 (top) shows that the indoor air temperature T_t^{in} stays within the preferred thermal comfort band throughout the simulation, where the outdoor air temperature forecast $T^{\text{out,f}}$ is shown for reference. Compared to House 1, the indoor temperature is much closer to the upper thermal comfort bound in House 2. The battery SOC is shown in Fig. 3.5 (middle), which highlights the usage of energy stored in the battery during the DR period. The battery operation is included in Fig. 3.5 (bottom) to show the battery does not simultaneously charge and discharge.

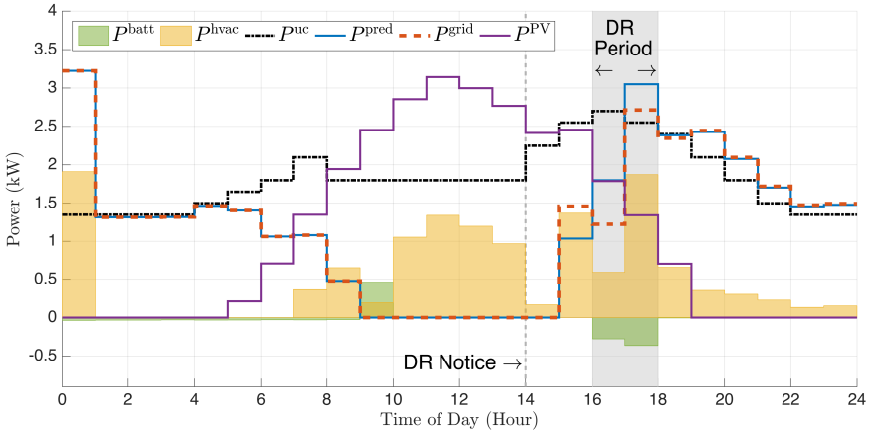

Figure 3.4: Power profiles for House 2 with HEMS algorithm in (3.1) responding to a summer load reduction DR event of $B^{\text{util}} = 0.75$ kW with uncertainty in available PV generation and outdoor air temperature forecast error where P^{base} =30 W/m^2 and T^{base}=1.0°F.

Additional simulation results for both houses with varying DR requests B^{util} and uncertainties with P^{base} and T^{base} are given in Table 3.3. Let B^{H1} and B^{H2} denote the actual reduction in grid power usage that House 1 and House 2 were able to achieve, respectively. From Table 3.3, we can see that B^{H1} and B^{H2} increase as the uncertainty in the solar forecast increases. For House 1 with constant P^{base}, increases in the uncertainty in the outdoor air temperature forecast error result in

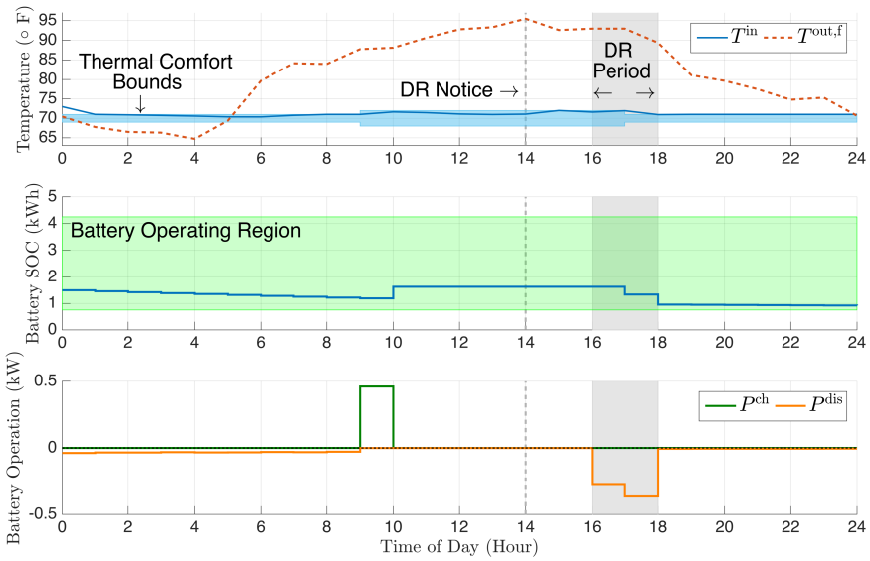

Figure 3.5: House 2 thermal comfort and battery operation results with HEMS algorithm in (3.1) responding to a summer load reduction DR event of $B_{\text{util}} = 0.75$ kW with uncertainty in available PV generation and outdoor air temperature forecast error where P^{base} =30 W/m^2 and T^{base}=1.0°F.

decreases in B^{H1} since more energy is required to maintain the indoor house temperature. For the simulation of House 2 with constant P^{base}, in some cases the HEMS does not need to compensate further as T^{base} varies since the uncertainty in the available PV is more restrictive. House 1 is able to achieve grid power usage reduction greater than or equal to the reduction achieved by House 2 due to the increased cooling efficiency and lower building envelope coefficient of House 1 relative to House 2.

Table 3.3: Additional DR-enabled HEMS algorithm simulation results for House 1 and House 2.

P^{base} (W/m^2)	T^{base} (°F)	B^{util} (kW)	B^{H1} (kW)	B^{H2} (kW)
15	0.5	0.5	0.6211	0.5815
15	1.0	0.5	0.6200	0.5811
30	0.5	0.5	0.6958	0.6609
30	1.0	0.5	0.6949	0.6609
15	0.5	0.75	0.8594	0.8307
15	1.0	0.75	0.8589	0.8307
30	0.5	0.75	0.9366	0.9109
30	1.0	0.75	0.9362	0.9109

Lastly, Monte Carlo simulations were conducted to validate that the chance constrained optimization solutions actually satisfy the DR request with probability at least $1 - \epsilon^{\text{DR}} = 0.95$

and the thermal comfort bounds are satisfied with probability at least $1 - \epsilon^{\overline{T}} = 1 - \epsilon^{\underline{T}} = 0.95$. Monte Carlo simulations use the optimal solution from the chance constrained HEMS formulation in (3.1) and solar forecast error and outdoor temperature forecast error sampled randomly from their respective distributions to check that constraints in (3.1g)-(3.1h) and (3.1n) are satisfied. For each of the eight simulations performed in Table 3.3 for both House 1 and House 2, 5000 Monte Carlo simulations are performed for validating that the optimal HEMS solutions satisfy the constraints in (3.1g)-(3.1h) and (3.1n). The percentages in Table 3.4 represent the empirical distributions of the Monte Carlo simulations that satisfy the DR request in (3.1n) and temperature bounds in (3.1g)-(3.1h) during the DR period. Thus, in view of Table 3.4, the Monte Carlo simulations validate that the solution obtained with the chance constrained MPC optimization problem ensures the DR request and temperature bounds are both satisfied with probability 0.95, respectively.

Table 3.4: Monte Carlo simulation results for validation of the chance constraints in the HEMS formulation in (3.1).

			House 1			House 2		
			Chance Constraint Satisfaction			Chance Constraint Satisfaction		
P^{base}	T^{base}	B^{util}		(3.1g)-(3.1h)			(3.1g)-(3.1h)	
(W/m^2)	(°F)	(kW)	(3.1n)	t=17	t=18	(3.1n)	t=17	t=18
15	0.5	0.50	99.24	100.00	95.32	95.32	95.58	95.14
15	1.0	0.50	99.30	99.92	95.02	95.52	95.22	95.34
30	0.5	0.50	97.62	100.00	95.34	95.50	95.10	95.08
30	1.0	0.50	97.44	99.98	95.36	95.24	95.24	95.10
15	0.5	0.75	98.96	100.00	95.30	95.64	95.10	95.40
15	1.0	0.75	98.76	99.98	95.04	95.72	95.02	95.34
30	0.5	0.75	97.28	100.00	95.56	95.08	95.44	95.60
30	1.0	0.75	97.56	99.92	95.08	95.18	95.02	95.74

3.2.2 HEMS with Varying Controllable Resources

Next, we study the performance of the second MPC-based HEMS algorithm as the set of controllable resources vary in both a flat (or non-time-varying) and time-of-use (TOU) electricity pricing setting. The set of controllable resources includes residentially-owned rooftop PV panels, a HBS, an electric vehicle (EV), and an HVAC system. The HEMS optimally schedules the set

of controllable resources given user preferences such as indoor thermal comfort and electricity cost sensitivity. As in the previous study, the HEMS is also a chance constrained, MPC-based algorithm, where the chance constraint ensures the indoor thermal comfort is satisfied with a high probability given uncertainty in the outdoor temperature and solar irradiance forecasts, which influence indoor air temperature and HVAC usage. Instead of only considering the performance of a HEMS algorithm with a HBS, rooftop PV generation, an EV, and a controllable HVAC system like other research in intelligent building-to-grid optimization literature, this study looks at the performance when a HEMS has a strict subset of those controllable resources. For example, one of the controllable resource scenarios this study considers is when the HEMS only has access to an HVAC system to intelligently control. The overall HEMS control and data schematic for the possible controllable resources is shown in Fig. 3.6. In the next sections, we provide the mathematical formulation of the HEMS, the derivation of the convex reformulation of the chance constraint, and case study results for multiple scenarios where the set of controllable resources is different in each scenario. The HEMS performance is measured with respect to three metrics: HBS operation (daily cycling), electricity cost to the customer, and grid power usage (load factor to measure variation in demand throughout the day). This study is based on my published results in [18].

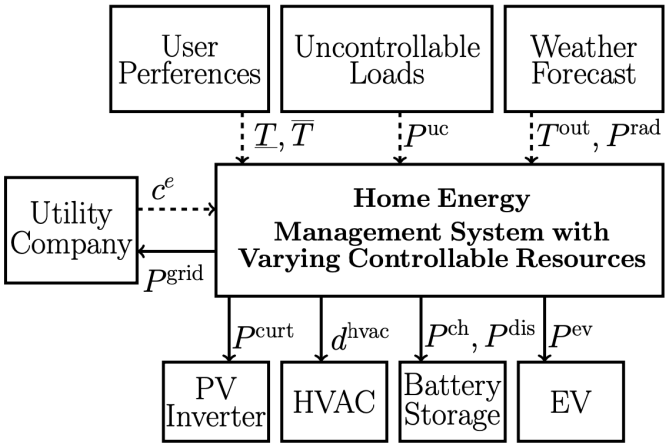

Figure 3.6: Control and data schematic for HEMS with the full set of possible controllable resources.

Table 3.5: Device scenarios for HEMS with varying controllable resources.

Scenario, s	Residentially Owned Devices, Ω_s
1	HVAC, PV, EV, HBS
2	HVAC PV, HBS
3	HVAC, PV, EV
4	HVAC, HBS
5	HVAC, EV
6	HVAC, PV
7	HVAC

3.2.2.1 Optimization Formulation

In this section, the overall chance constrained MPC-based optimization problem for the HEMS is formulated, including the mathematical models for the indoor air temperature dynamics and controllable residential resources. In this study, we assume that the HEMS must coordinate a subset (or all) of the following resources: an HVAC system, residential PV generation, an HBS, and an EV, in addition to satisfying the uncontrollable load using any additional power needed from the grid. Similar to the previous HEMS study in Section 3.2.1, we assume that excess solar is not able to be transported to the grid. We consider different scenarios of controllable resources, given in Table 3.5, to study the effect of available controllable devices on HEMS control performance with respect to HBS operation, electricity cost, and daily grid load factor. Let the set of devices in scenario s be denoted $\Omega_s \subseteq \{\text{HVAC}, \text{PV}, \text{EV}, \text{HBS}\}$.

Let the vectors $\mathbf{u}_t = [P_t^{\text{grid}}, P_t^{\text{curt}}, d_t^{\text{hvac}}, P_t^{\text{ch}}, P_t^{\text{dis}}, P_t^{\text{ev}}]$ and $\mathbf{x}_t = [T_t^{\text{in}}, E_t^{\text{b}}, E_t^{\text{ev}}]$ be the collection of decision variables and state variables, respectively, at time $t \in \mathcal{T}$, where $\mathcal{T} = \{1, \ldots, T_h\}$.

Then, the overall chance constrained HEMS optimization problem is the following:

$$\min_{\{\mathbf{x}_t,\mathbf{u}_t\}_{t=1}^{T_h}} \quad \sum_{t=1}^{T_h} c_t^e\left(P_t^{\text{grid}} + \alpha P_t^{\text{ch}}\right) \tag{3.14a}$$

$$\text{s.t.} \quad 0 \le P_t^{\text{grid}}, \qquad \forall t \in \mathcal{T}, \tag{3.14b}$$

$$0 \le P_t^{\text{curt}} \le P_t^{\text{sol}}, \qquad \forall t \in \mathcal{T}, \text{PV} \in \Omega_s, \tag{3.14c}$$

$$0 \le d_t^{\text{hvac}} \le 1, \qquad \forall t \in \mathcal{T}, \text{HVAC} \in \Omega_s, \tag{3.14d}$$

$$T_{t+1}^{\text{in}} = T_t^{\text{in}} + \beta_1(T_t^{\text{out}} - T_t^{\text{in}}) - \beta_2 d_t^{\text{hvac}} + \beta_3 P_t^{\text{rad}}, \qquad \forall t \in \mathcal{T}, \text{HVAC} \in \Omega_s, \tag{3.14e}$$

$$\Pr(T_{t+1}^{\text{in}} - \overline{T}_{t+1} \le 0) \ge 1 - \epsilon^{\overline{T}}, \qquad \forall t \in \mathcal{T}, \text{HVAC} \in \Omega_s, \tag{3.14f}$$

$$E_{t+1}^{\text{b}} = E_t^{\text{b}} + \Delta t \eta^{\text{ch}} P_t^{\text{ch}} - \Delta t \frac{1}{\eta^{\text{dis}}} P_t^{\text{dis}}, \qquad \forall t \in \mathcal{T}, \text{HBS} \in \Omega_s, \tag{3.14g}$$

$$\underline{E}^{\text{b}} \le E_{t+1}^{\text{b}} \le \overline{E}^{\text{b}}, \qquad \forall t \in \mathcal{T}, \text{HBS} \in \Omega_s, \tag{3.14h}$$

$$0 \le P_t^{\text{ch}} \le \overline{P}^{\text{b}}, \qquad \forall t \in \mathcal{T}, \text{HBS} \in \Omega_s, \tag{3.14i}$$

$$0 \le P_t^{\text{dis}} \le \overline{P}^{\text{b}}, \qquad \forall t \in \mathcal{T}, \text{HBS} \in \Omega_s, \tag{3.14j}$$

$$E_{t+1}^{\text{ev}} = E_t^{\text{ev}} + \Delta t \eta^{\text{ev}} P_t^{\text{ev}}, \qquad \forall t \in \mathcal{T}, \text{EV} \in \Omega_s, \tag{3.14k}$$

$$\underline{E}^{\text{ev}} \le E_{t+1}^{\text{ev}} \le \overline{E}^{\text{ev}}, \qquad \forall t \in \mathcal{T}, \text{EV} \in \Omega_s, \tag{3.14l}$$

$$0.9\overline{E}^{\text{ev}} \le E_t^{\text{ev}}, \qquad \forall t \in \mathcal{T}^{\text{f}}, \text{EV} \in \Omega_s, \tag{3.14m}$$

$$E_t^{\text{ev}} = 0.2\overline{E}^{\text{ev}}, \qquad \forall t \in \mathcal{T}^{\text{a}}, \text{EV} \in \Omega_s, \tag{3.14n}$$

$$P_t^{\text{ev}} = 0, \qquad \forall t \in \mathcal{T}^{\text{a}}, \text{EV} \in \Omega_s, \tag{3.14o}$$

$$0 \le P_t^{\text{ev}} \le \overline{P}^{\text{ev}}, \qquad \forall t \in \mathcal{T}, \text{EV} \in \Omega_s, \tag{3.14p}$$

$$0 = P_t^{\text{grid}} + P_t^{\text{sol}} - P_t^{\text{curt}} + P_t^{\text{dis}} - P_t^{\text{uc}} - P^{\text{ac}} d_t^{\text{hvac}} - P_t^{\text{ch}} \; - P_t^{\text{ev}}, \qquad \forall t \in \mathcal{T}. \tag{3.14q}$$

The objective function in (3.14a) minimizes the cost of electricity drawn from the grid and has a small penalty on battery usage to capture future replacement costs, where $\alpha = 0.01$ in this study. Here, the cost of electricity is time-varying to allow for TOU prices. The constraint in (3.14b) enforces that PV generation must be consumed locally and excess cannot be exported to the grid. As mentioned in the previous HEMS formulation in Section 3.2.1, this equation could be omitted in a situation where there is net metering or feed-in tariffs. If the HEMS coordinates rooftop PV,

the equation (3.14c) limits PV curtailment by the amount of PV generation available. If the HEMS coordinates HVAC usage, equations (3.14d)-(3.14f) model the indoor temperature dynamics, where β_1 represents the building envelope coefficient, β_2 is the cooling gain coefficient, and β_3 is the solar gain coefficient. The limits on the HVAC duty cycle (for cooling) are enforced in (3.14d). The chance constraint in (3.14f) enforces that the upper thermal comfort bound must be satisfied with a high probability $1 - \epsilon^{\overline{T}}$ given uncertainty in the outdoor air temperature forecast and solar irradiance, where $\epsilon^{\overline{T}}$ is a small number like 0.05 or 0.1. The derivation of the convex reformulation of the chance constriant in (3.14f) is provided in the next section. If the HEMS is able to control a HBS, the optimization uses the battery model constraints given in (3.1j)-(3.1m). We again omit the non-convex complementarity constraint $P_t^{\text{ch}} \cdot P_t^{\text{dis}} = 0, \ \forall t \in \{1, \ldots, T_h\}$ since proper HBS charging and discharging behavior is guaranteed by the structure of the problem, i.e., the small penalty on battery usage in the objection in (3.14a) (see Chapter 5). If an EV is included in the set of controllable resources, the HEMS algorithm includes the EV charging constraints in (3.14k)-(3.14p). For constraints (3.14m)-(3.14o), let $\mathcal{T}^{\text{f}}$ be the set time periods where the EV must be $\geq$90% charged and let $\mathcal{T}^{\text{a}}$ be the set of time periods when the EV is unavailable for charging (away from the home). Then, (3.14m) ensures the EV is charged for the next trip and (3.14n)-(3.14o) enforces that the EV cannot be charged by the HEMS while away from the home. Lastly, the power balance (PB) within the home is given in (3.14q). Note that terms in (3.14q) are omitted as necessary if their corresponding device is not applicable to the HEMS algorithm in scenario s.

3.2.2.2 Derivation of the Chance Constraint

Now, we derive the convex reformulation of the chance constraint in (3.14f) that ensures the user thermal comfort is maintained with high probability given uncertainty in forecasting errors in weather parameters that influence indoor air temperature. Notice that this constraint is the same as the chance constraint in (3.1h). Using the same assumptions and derivation for (3.1h) in

Section 3.2.1.2, we obtain the following convex reformulation:

$$\overline{T}_{t+1} - T_t^{\text{in}} - \beta_1(T_t^{\text{out,f}} + \mu_t^{\text{T}} - T_t^{\text{in}}) + \beta_2 d_t^{\text{hvac}} - \beta_3(P_t^{\text{rad,f}} + \mu_t^{\text{P}}) \geq \Phi^{-1}(1-\epsilon^{\overline{T}})\sqrt{(\beta_1\sigma_t^{\text{T}})^2 + (\beta_3\sigma_t^{\text{P}})^2}, \quad (3.15)$$

which replaces (3.14f) in the HEMS formulation in (3.14).

3.2.2.3 Case Study

Case study results demonstrate the dependence of the chance constrained MPC-based HEMS performance on the set of available controllable resources. For each scenario in Table 3.5, we provide simulation results for a home subject to a constant electricity price of $c^e = \$0.11$/kWh and when subject to a TOU pricing schedule. The TOU rates in Table 3.6 are based on Xcel Energy's summer TOU rates [68]. The problem is implemented in MATLAB and the convex optimization solver CVX [64,65] is used in this work. For all simulations, we assume the thermal comfort bound must be satisfied with probability 0.95 ($\epsilon^{\overline{T}} = 0.05$). The preferred indoor thermal comfort requires the indoor temperature to be below 72°F for all times t in each scenario s. The simulation is run for 7 days with a prediction horizon of $H = 12$ hours with 1 hour time steps. The weather and uncontrollable load data were obtained from the RBSA data set [69].

The residential PV array size is 16m^2 with an efficiency of 16%. The HBS has a rated storage capacity of 5 kWh and the inverter power limit is 3 kW. The HBS has a charging and discharging efficiency $\eta^{\text{ch}} = \eta^{\text{dis}} = 95\%$. The HBS SOC limits $\underline{E}^{\text{b}}$ and $\overline{E}^{\text{b}}$ are 15% and 85% of the rated energy storage capacity, respectively, which limits battery degradation when operating in this region [6]. The power consumption of the HVAC when cooling is $P^{\text{ac}} = 3$ kW. The EV has a 14.5 kWh battery capacity, a charging inverter limit of 3.5 kW, and charging efficiency $\eta^{\text{ev}} = 95\%$. Based on a standard work schedule, we assume that the EV must be charged to $\geq 90\%$ by 9am daily, the EV is away from the home (not able to be charged) from 9am to 5pm daily, and the EV returns at 5pm daily with the EV battery at 20% capacity.

The chance constrained MPC-based algorithm for a HEMS is simulated using the same house

Table 3.6: TOU rates for HEMS performance study.

Period	Time	Price, c_t^e
Off Peak	9pm-9am	\$0.08/kWh
Shoulder	9am-2pm,6pm-9pm	\$0.13/kWh
On-Peak	2pm-6pm	\$0.18/kWh

for each of the 7 device scenarios in Table 3.5 in a constant electricity price schedule and a TOU varying price schedule. The house has model parameters $\beta_1 = 0.03$, $\beta_2 = 4$, and $\beta_3 = 1.63 \times 10^{-4}$. The initial battery SOC is 1.5 kWh, the initial EV SOC is 7.25 kWh, and the initial indoor temperature is 70°F. The outdoor temperature forecast error at each time $t \in \{1, \ldots, T_h\}$ is assumed to be $T_t^{\text{out,e}} \sim \mathcal{N}(0, (0.5 + 0.1(t-1))^2)$ and the solar irradiance forecast error is assumed to be $P_t^{\text{rad,e}} \sim \mathcal{N}(0, (15 + 5(t-1))^2)$. We perform receding horizon MPC, where we implement the first hour of the control strategy, and then repeat the optimization starting from the next hour where the initial indoor temperature at the next step includes added sampled Gaussian noise from the weather forecast uncertainty.

Three metrics are used to evaluate HEMS performance. The first metric is average daily HBS cycling over the 7 day simulation, since battery lifetime is often measured in cycles, which we define as:

$$\text{average daily HBS cycling} = \frac{1}{7} \frac{\Delta t \sum_{t=1}^{7 \cdot 24} P_t^{\text{ch}}}{\overline{E}^{\text{b}} \cdot 85\%}. \tag{3.16}$$

The second metric is total cost to the customer, which is minimized by the HEMS algorithm objective according to the electricity pricing schedule. The third metric is daily load factor for each day i in the simulation, which is given by:

$$\text{load factor for day } i = \frac{\max(\{P_t^{\text{grid}}\}_{t=24(i-1)+1}^{t=24i})}{\text{mean}(\{P_t^{\text{grid}}\}_{t=24(i-1)+1}^{t=24i})}, \tag{3.17}$$

which we use to capture the variation in P_t^{grid} each day, i.e., "peakiness" of electricity demand from the grid.

First, we show the simulation results for Scenario 1, a house with an HVAC system, an HBS, rooftop PV panels, and an EV, in Figs. 3.7 and 3.8. In Fig. 3.7 (top), we highlight the difference in

the electricity drawn from the grid for the different electricity pricing schedules. In a TOU pricing situation, we see that there is a spike in the amount of P_t^{grid} consumed before the price of electricity increases at 9 AM daily. Since Scenario 1 includes rooftop PV generation that is able to satisfy the load during the next price increase at 2 PM daily, we generally do not see the new peaks arise at the 2 PM price increase time (except in Day 2). In Fig. 3.7 (middle), we provide the indoor air temperature to show the differences in pre-cooling trends. In the constant electricity price case, the HEMS pre-cools the home before the hottest part of each day (the outdoor air temperature is provided in Fig. 3.7 (bottom) for reference). Conversely, in the TOU electricity price case the HEMS pre-cools the home in the hours leading up to the daily price increases. In Fig. 3.8, we show the HBS operation in both pricing situations. From Fig. 3.8 (both middle plots), we can see that in a constant electricity price setting, the HBS generally charges when there is excess solar; whereas, in the TOU electricity price setting, the HBS is charged when the electricity is least expensive and discharges to meet the total load when the price of electricity more expensive. This operation also impacts the HBS cycling pattern as shown in Fig. 3.8 (top).

Next, we provide simulation results in terms of the three metrics described above for each of the 7 scenarios listed in Table 3.5 with both a constant electricity price and a TOU electricity price. These results are summarized in Table 3.7, where **bolded** values indicate an increase from the constant electricity price case to the TOU pricing case. In Table 3.7, for all scenarios except Scenarios 3 and 6, we see that the daily load factor is generally larger in the TOU electricity pricing case than the constant electricity price case. The TOU electicity pricing case for Scenarios 3 and 6 generally do not experience increased daily load factors due to the lack of battery-like devices (HBS and EV) in these scenarios. In scenarios with battery-like devices, the HEMS charges these before the daily price increases at 9 AM and 2 PM resulting in higher daily load factors. Additionally, the average daily HBS cycling increases in a TOU price setting in all scenarios with an HBS. This further shows that TOU pricing leads to HBS charging patterns where the HBS will charge using power from the grid during off-peak periods, instead of utilizing the battery to store excess solar. In all scenarios, the TOU electricity schedule decreases the customer electricity price compared

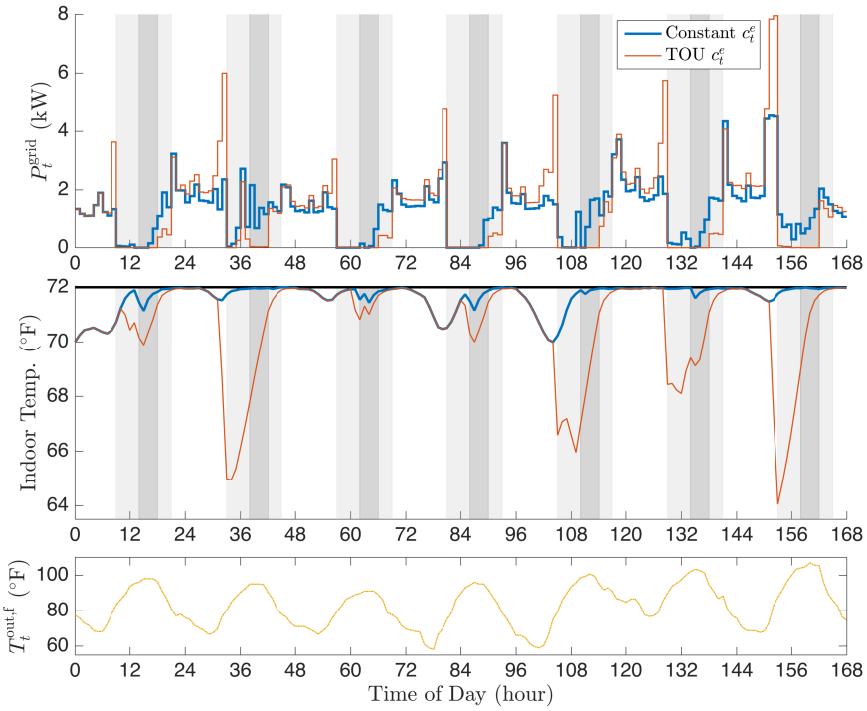

Figure 3.7: Simulation results for for P^{grid} and T^{in} in Scenario 1 for HEMS algorithm with varying controllable resources. Top: Profiles of power drawn from the grid for both pricing schedules with the proposed HEMS algorithm. Middle: Average hourly indoor air temperature for both pricing schedules with the proposed HEMS algorithm. Bottom: Outdoor air temperature forecast.

to a constant price; however, that is often at the cost of increased HBS cycling and daily load factor. For comparison, a baseline simulation was performed where the HEMS operates without the chance constrained MPC and the only controllable resource is HVAC. This highlights that, in most scenarios, the HEMS control using an MPC-based algorithm results in a lower electricity cost, except in Scenario 4 with a constant electricity price and Scenario 5. In Scenario 4 with a constant electricity cost, the total electricity price was higher than the baseline case since the inclusion of chance constraints results in a slightly more conservative HVAC control solution to account for the uncertainty. In Scenario 5, the total electricity cost is the largest due to the increased load resulting from the EV and the lack of a coupled HBS or PV system. However, in Scenario 5 the HEMS was able to reduce the total electricity cost in the TOU price case compared to the constant price case. Thus, in most scenarios, the HEMS utilizing an MPC-based algorithm was able to leverage the controllable resources to provide a cost reduction to the consumer, even if HVAC is the only

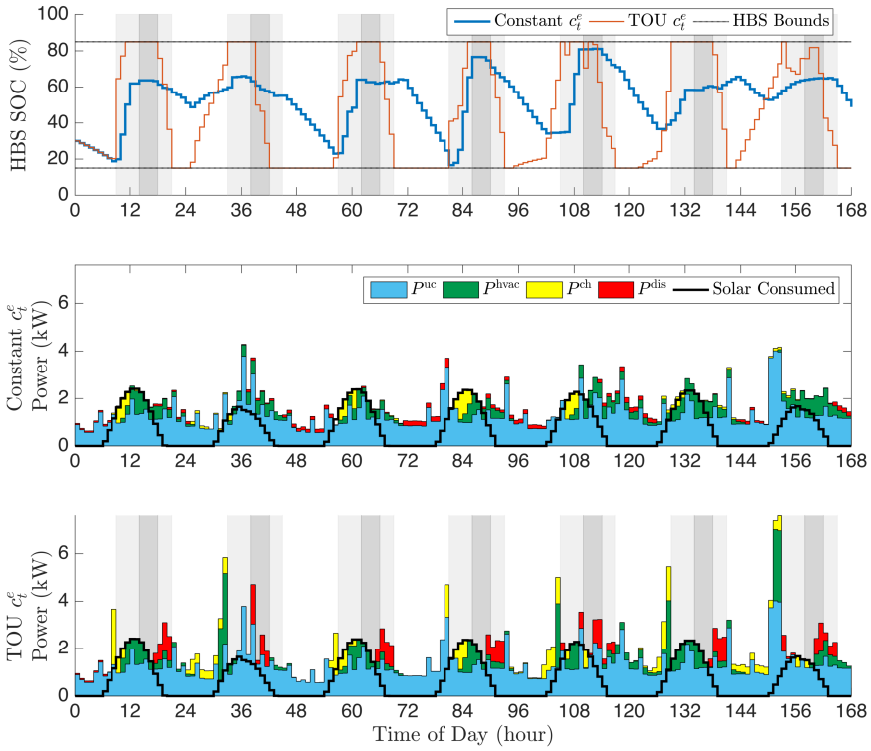

Figure 3.8: Simulation results for HBS usage in Scenario 1 for HEMS algorithm with varying controllable resources. Top: HBS SOC under both pricing schedules with the proposed HEMS algorithm. Middle(both): Stacked area plot showing HBS charging and discharging behavior with respect to total load (uncontrollable load and HVAC load) and consumed solar power: $P^{\text{PV}} = P^{\text{sol}} - P^{\text{curt}}$. (bottom) EV charging profile under both pricing schedules with the proposed HEMS algorithm.

controllable resource available.

3.3 Discussion and Conclusions

In this chapter, two chance constrained MPC-based optimization models were proposed for a HEMS algorithm that coordinates appliances, customer preferences, and BTM controllable resources such as generation from rooftop PV panels and an HBS. These algorithms aim to improve the flexibility of residential electricity usage to aid the integration of renewable energy onto the grid.

The first chance constrained MPC-based HEMS algorithm is capable of responding to utility-requested DR events. Chance constraints were incorporated into the optimization problem to ensure

Table 3.7: HEMS performance for each varying controllable resource scenario. 'C' and 'TOU' denote scenario s under a constant electricity price and TOU electricity price, respectively. HBS cycling is the average daily HBS cycling, calculated using (3.16). The baseline scenario is a HEMS controlling only an HVAC system without chance constrained MPC.

Scenario, s	Total Cost ($)	HBS Cycling	Load Factor						
			Day 1	Day 2	Day 3	Day 4	Day 5	Day 6	Day 7
1 - C	24.12	0.45	3.16	1.83	2.41	3.05	2.65	3.09	2.70
1 - TOU	18.82	0.92	**3.81**	**3.87**	**3.19**	**3.94**	**3.63**	**3.98**	**4.54**
2 - C	16.44	0.41	3.34	2.61	2.87	3.51	2.97	3.47	2.70
2 - TOU	13.23	0.90	**4.24**	**4.30**	**3.36**	**4.68**	**3.95**	**4.62**	**4.91**
3 - C	24.15	–	3.30	1.82	2.25	2.96	2.86	3.06	2.60
3 - TOU	20.28	–	3.14	**3.46**	**2.31**	2.81	2.78	2.96	**4.20**
4 - C	29.90	0.20	1.69	2.61	1.93	2.18	2.01	1.90	2.11
4 - TOU	28.41	0.86	**3.28**	**3.42**	**3.29**	**4.30**	**2.70**	**2.83**	**3.70**
5 - C	37.35	–	1.85	2.07	1.49	2.25	1.87	1.96	2.28
5 - TOU	37.14	–	**2.84**	**3.01**	**2.82**	**3.69**	**2.44**	**2.56**	**3.45**
6 - C	16.46	–	3.55	2.59	2.70	3.28	3.31	3.45	2.60
6 - TOU	14.69	–	3.55	**3.75**	2.70	3.28	3.26	3.31	**4.55**
7 - C	29.64	–	1.76	2.64	2.02	2.16	2.02	1.88	2.09
7 - TOU	28.41	–	**2.92**	**3.12**	**2.92**	**3.99**	**2.40**	**2.68**	**3.47**
Baseline - C	29.67	–	1.61	2.50	1.80	2.26	1.87	1.86	2.20

the DR request and home indoor air temperature preferences are satisfied with a high probability given uncertainty in both the solar and weather forecasts. Simulation results demonstrate the proposed HEMS algorithm responded to the DR request by coordinating flexible devices during the DR notice period prior to DR event, even when the uncertainty in the solar generation and weather forecasts is increased. Monte Carlo simulations were performed to validate the satisfaction of the chance constraints.

In the second chance constrained MPC-based HEMS study, the performance of the HEMS algorithm is compared across multiple scenarios, each with different sets of controllable BTM resources, under a constant electricity price and a TOU electricity price. Similar to the first HEMS optimization model that was proposed, chance constraints ensured the indoor thermal comfort was maintained with high probability given uncertainty in the weather forecast. The HEMS performance is measured in terms of total electricity cost, HBS cycling, and daily load factor. Simulation results showed that in most scenarios with a TOU electricity price, the HBS usage and the daily load factor increased. While an increase in load factor may not be significant on its own, with

aggregations of many homes, it could require an increase in ramping capacity from generators in the grid, and potentially have a higher peak load than when HEMS are not present. Although TOU electricity pricing did impact HBS usage and daily load factor, the HEMS was able to optimally coordinate the available controllable resources in each scenario to decrease the total electricity cost for the consumers.

Chapter 4

Flexible Line Flow Ratings for Minimizing Wind Power Curtailment in Transmission Grids

This chapter presents a two-stage stochastic optimization model to determine the optimal economic generator dispatch while minimizing the amount of curtailed wind power across possible generation scenarios. The model includes a novel chance constrained flexible transmission line capacity rating model that allows line capacities to be temporarily increased in areas of the network experiencing congestion to minimize available wind power generation curtailment. The proposed two-stage optimization model's performance with flexible line capacity ratings is demonstrated on the three-area RTS-GMLC data set [70], where wind power curtailment is reduced by 40% compared to when line capacity ratings are fixed.

4.1 Transmission Line Capacity Ratings and Wind Power Curtailment Trends

As mentioned in Section 1.1.2, there is currently over 103,700 MW of installed wind capacity in the United States [8] (as of July 2020). This growing amount is challenging how our transmission grid is operated. As the penetration of wind power increases, more situations arise where wind power must be curtailed in order to minimize transmission congestion [9, 10]. Wind curtailment primarily occurs due to limited available transmission during a particular time to incorporate some or all of the wind, or high wind power availability at times of low load and when excess generation cannot be exported to other areas due to transmission constraints [9, 10]. In this chapter, we propose

an optimization framework for flexible transmission line capacity ratings to minimize wind power curtailment by temporarily and safely increasing line ratings.

Line rating constraints are used by transmission operators to ensure that flows (power carrying capacity) on transmission lines do not result in damage to the lines or equipment or cause reliability issues. Today, most regional transmission organizations/independent system operators (RTOs/ISOs) use either static line ratings or seasonal line ratings [71, 72]. Included in these ratings are a continuous rating (indefinitely), a long-term rating (hours), and a short-term emergency rating (minutes) [72, 73]. However, many RTOs/ISOs are researching dynamic line ratings (DLR) that reflect weather conditions and line congestion in real-time [71].

Incorporating DLR with chance constraints has been considered to address transmission line congestion and uncertainty in renewable generation forecasts and weather conditions [42–45]. A chance constrained congestion management problem is proposed in [43] to ensure the probability that a line is overloaded is less than some prescribed value. In a security constrained optimal power flow setting with DLR, chance constraints are used to incorporate uncertainty in weather conditions that impact the line ratings [45].

Additionally, chance constraints have been used to address uncertainty in wind power generation. In [42], chance constraints are used in a two-stage stochastic unit commitment problem to ensure that the available wind power is utilized with a high probability. Similar to our use of chance constraints for line capacity limits in this study, chance constraints have been used to ensure those line ratings are satisfied with a high probability in a security constrained optimal power flow setting [44]. In [74], the authors propose a stochastic two-stage program that minimizes congestion due to uncertain wind generation in the network by allowing stochastic variation in line ratings.

Optimal transmission switching has been proposed as another approach for mitigating line congestion in transmission networks. In [75], the authors propose a security constrained optimal power flow model with transmission switching and DLR that is based on real-time weather conditions and conductor properties in order to alleviate transmission congestion and ensure power flows in the network are more homogeneous. In [76], a sample average approximation of a chance

constraint is proposed to ensure available wind power is utilized with high probability in a day ahead economic dispatch with optimal transmission switching.

Using integer chance constraints to model flexible system limits, similar to those we present in this study, has been proposed within a unit commitment setting. In [46], chance constraints are used to ensure that the generators operating limits are violated with a low probability when uncertainty in wind power availability is considered. In this study, we use a similar approach where we use an integer chance constraint to ensure the probability of line capacity limit violations is less than some prescribed value in solving the optimal power flow with uncertain wind generation.

This chapter proposes a two-stage stochastic optimal power flow model with flexible transmission line capacity ratings to account for variability in wind power generation and alleviate line congestion. We formulate an integer joint chance constraint to limit the probability of continuous line rating violations across all considered wind scenarios, all times, and all lines in the network. During violations, the rating is increased to the long-term line limit. We use a sample average (SAA) approximation for the joint chance constraint in order to render it computationally tractable. This chapter is based on my published work in [19].

4.2 Two-Stage Stochastic Optimization Model for Flexible Line Flow Ratings

This section discusses the flexible line flow ratings we use in this study and provides the overall formulation for the two-stage stochastic problem. Then the uncertainty in wind forecast errors is discussed, and we derive the SAA of the chance constraint, using the method described in Section 2.3.3, that captures uncertainty in the forecasted wind output.

4.2.1 Flexible Line Flow Ratings

In this work, we assume the line flow rating must nominally be at the continuous rating. As mentioned in Section 4.1, a line can safely and reliably be at its continuous rating, denoted $\overline{F}_l$, for an indefinite amount of time. However, to mitigate congestion in the network and minimize curtailment of available wind generation, a line flow rating can be increased temporarily to its long

Table 4.1: Notation for flexible line flow rating model.

	Sets
$l \in \mathcal{L}$	Set of lines $l = (i, j)$
$b \in \mathcal{B}$	Set of buses
$g \in \mathcal{G}$	Set of thermal, dispatchable generators
$r \in \mathcal{R}$	Set of renewable sources (PV and hydro)
$w \in \mathcal{W}$	Set of wind sources
$s \in \mathcal{S}$	Set of scenarios
$h \in \mathcal{H}_g$	Set of cost function sample points for generator g
$t \in \mathcal{T}$	Hourly time steps: $1, \ldots, T$
$\mathcal{R}_b$	Set of renewable sources r at bus b
$\mathcal{W}_b$	Set of wind sources w at bus b
$\mathcal{G}_b$	Set of generators at bus b
$\mathcal{L}_b^{\mathrm{o}}$	Set of lines with origin bus b
$\mathcal{L}_b^{\mathrm{d}}$	Set of lines with destination bus b
	First Stage Decision Variables
$P_{g,t}^{\mathrm{G}}$	Real power dispatch of generator g
$c_{g,t}^{\mathrm{G}}$	Generation cost of generator g
$a_{g,h,t}$	Coefficient of sample point h for generator g solution as a point on generator cost function
	Second Stage Decision Variables
$y_{l,t,s}$	Binary indicating line rating violation of line l
$\sigma_{l,t,s}$	Continuous line flow rating violation amount
$\theta_{b,t,s}$	Voltage angle at bus b
$P_{l,t,s}$	Power flow on line l
$P_{r,t,s}^{\mathrm{c}}$	Curtailment of renewable source r
$P_{w,t,s}^{\mathrm{c}}$	Curtailment of wind source w

	Parameters
$\overline{F}_l$	Continuous line power flow rating
$\overline{\overline{F}}_l$	Long term line power flow rating
B_l	Susceptance of line l
$P_{b,t}^{\mathrm{L}}$	Active power consumed at bus b
$\underline{P}^{\mathrm{G}}$	Minimum real power dispatch of generator g
$\overline{P}^{\mathrm{G}}$	Maximum real power dispatch of generator g
$c_{g,h}$	Generation cost of generator g at sample point h (USD/hr)
ϵ	Probability line flow violation limit is satisfied
i	Origin bus of line l
j	Destination bus of line l
$P_{r,t}^{\mathrm{res}}$	Available power from renewable source r
P_t^{f}	Forecasted available power from wind source w
$P_{r,t}^{\mathrm{c}}$	Maximum curtailment of renewable source r
$P_{w,t}^{\mathrm{c}}$	Maximum curtailment of from wind source w
g_b^{FS}	Bus b fixed shunt conductance
p_s	Probability of scenario s
$p_{g,h}$	Real power output of generator g at sample point h
	Random Variables
$P_{w,t,s}^{\mathrm{e}}$	Forecast error of wind source w
$\tilde{P}_{w,t,s}^{\mathrm{wind}}$	Available power from wind source w

term rating, denoted $\overline{\overline{F}}_l$, for a maximum of some given number of consecutive hours. Here, we assume that a line can be at its long term rating for a maximum of 24 consecutive hours [73], and the ratings are naturally such that $\overline{\overline{F}}_l > \overline{F}_l$ for all lines $l \in \mathcal{L}$. We propose a chance constraint to ensure that the continuous line flow rating is violated (up to a maximum of the long term rating) with a low probability across all lines in the network, all time steps in the simulation, and all considered wind scenarios.

4.2.2 Two-Stage Stochastic Optimization Model

Next, we introduce the two-stage stochastic program with flexible line flow ratings to minimize wind power curtailment. The relevant notation is given in Table 4.1. In the first stage, we decide the optimal economic dispatch of the thermal generators subject to a linear power flow model with network constraints, i.e., DC OPF. We then observe the error in the available wind power forecast. Then in the second stage, we determine the curtailment of power generated from wind sources. The overall flexible line capacity rating optimization problem is:

$$\min \qquad \sum_{t\in T}\left[\sum_{g\in\mathcal{G}} c^{\mathrm{G}}_{g,t} + p_s \sum_{s\in\mathcal{S}}\sum_{w\in\mathcal{W}} P^{\mathrm{c}}_{w,t,s}\right] \tag{4.1a}$$

subject to:

$$c^{\mathrm{G}}_{g,t} = \sum_{g\in\mathcal{G}}\sum_{h\in\mathcal{H}_g} c_{g,h}a_{g,h,t}, \qquad \forall g\in\mathcal{G},\forall t\in\mathcal{T}, \tag{4.1b}$$

$$P^{\mathrm{G}}_{g,t} = \sum_{h\in\mathcal{H}_g} p_{g,h}a_{g,h,t}, \qquad \forall g\in\mathcal{G},\forall t\in\mathcal{T}, \tag{4.1c}$$

$$0 \le a_{g,h,t}, \qquad \forall g\in\mathcal{G},\forall t\in\mathcal{T},\forall h\in\mathcal{H}_g, \tag{4.1d}$$

$$\sum_{h\in\mathcal{H}_g} a_{g,h,t} = 1, \qquad \forall g\in\mathcal{G},\forall t\in\mathcal{T}, \tag{4.1e}$$

$$\sum_{g\in\mathcal{G}_b} P^{\mathrm{G}}_{g,t} + \sum_{l\in\mathcal{L}^{\mathrm{d}}_b} P_{l,t,s} - \sum_{l\in\mathcal{L}^{\mathrm{o}}_b} P_{l,t.s} - g^{\mathrm{FS}}_b + \sum_{r\in\mathcal{R}_b}(P^{\mathrm{res}}_{r,t} - P^{\mathrm{c}}_{r,t,s}) + \sum_{w\in\mathcal{W}_b}(\tilde{P}^{\mathrm{wind}}_{w,t} - P^{\mathrm{c}}_{w,t,s}) - P^{\mathrm{L}}_{b,t} = 0, \qquad \forall b\in\mathcal{B},\forall t\in\mathcal{T},\forall s\in\mathcal{S}, \tag{4.1f}$$

$$0 \le P^{\mathrm{c}}_{r,t,s} \le \overline{P}^{\mathrm{res}}_{r,t}, \qquad \forall r\in\mathcal{R},\forall t\in\mathcal{T},\forall s\in\mathcal{S}, \tag{4.1g}$$

$$0 \le P^{\mathrm{c}}_{w,t,s} \le \overline{P}^{\mathrm{wind}}_{w,t,s}, \qquad \forall w\in\mathcal{W},\forall t\in\mathcal{T},\forall s\in\mathcal{S}, \tag{4.1h}$$

$$\underline{P}^{\mathrm{G}}_{g} \le P^{\mathrm{G}}_{g,t} \le \overline{P}^{\mathrm{G}}_{g}, \qquad \forall g\in\mathcal{G},\forall t\in\mathcal{T} \tag{4.1i}$$

$$P_{l,t,s} = B_l(\theta_{i,t,s} - \theta_{j,t,s}), \qquad \forall l\in\mathcal{L},\forall t\in\mathcal{T},\forall s\in\mathcal{S}, \tag{4.1j}$$

$$-(\overline{F}_l + \sigma_{l,t,s}) \leq P_{l,t,s} \leq \overline{F}_l + \sigma_{l,t,s}, \qquad \forall l \in \mathcal{L}, \forall t \in \mathcal{T}, \forall s \in \mathcal{S}, \quad (4.1k)$$

$$0 \leq \sigma_{l,t,s} \leq y_{l,t,s}(\overline{\overline{F}}_l - \overline{F}_l), \qquad \forall l \in \mathcal{L}, \forall t \in \mathcal{T}, \forall s \in \mathcal{S}, \quad (4.1l)$$

$$\frac{1}{|\mathcal{T}||\mathcal{L}||\mathcal{S}|} \sum_{s \in \mathcal{S}} \sum_{t \in \mathcal{T}} \sum_{l \in \mathcal{L}} y_{l,t,s} \leq \epsilon \quad (4.1m)$$

$$y_{l,t,s} \in \{0, 1\}, \qquad \forall l \in \mathcal{L}, \forall t \in \mathcal{T}, \forall s \in \mathcal{S}. \quad (4.1n)$$

The objective function in (4.1a) ensures that the generator dispatch is economical and expected curtailment of wind sources is minimized. Constraints (4.1b)-(4.1e) model the generator dispatch cost as a linear interpolation of $|\mathcal{H}_g|$-many sample points $(p_{g,h}, c_{g,h})$ of the generator dispatch and corresponding cost. The power balance at each bus is enforced in (4.1f). Equations (4.1g) and (4.1h) limit the curtailable power from renewable energy sources and wind sources, respectively, since curtailment can be at most the available power. In the RTS-GMLC dataset [70], it is assumed that hydroelectric generation units are self scheduling and any rooftop photovoltaic (PV) generation is must-take; thus, for these renewable sources $\overline{P}^{\text{res}}_{r,t} = 0$ for all times $t \in \mathcal{T}$. However, wind and utility PV are fully curtailable; thus, for utility PV sources $\overline{P}^{\text{res}}_{r,t} = P^{\text{res}}_{r,t}$ and wind sources $\overline{P}^{\text{wind}}_{w,t,s} = \tilde{P}^{\text{wind}}_{w,t,s}$ for all times $t \in \mathcal{T}$ and scenarios $s \in \mathcal{S}$. In this work, we assume that the available wind power $\tilde{P}^{\text{wind}}_{w,t,s}$ is a random variable and is a function of the wind forecast and forecast error. The uncertainty in available wind power will be discussed further in Section 4.2.3. The real power dispatch for thermal generators is limited in (4.1i). The DC OPF power flow equations are given in (4.1j)-(4.1k). Equation (4.1k) allows the continuous line flow limits to be violated by some amount $\sigma_{l,t,s}$. The magnitude of the line flow violation can be at most the difference between the continuous line flow rating $\overline{F}_l$ and the long term line rating $\overline{\overline{F}}_l$ when the binary variable $y_{l,t,s} = 1$, which is enforced by (4.1l). The chance constraint in (4.1m) ensures that lines only violate their nominal continuous line capacity rating with probability at most ϵ across all lines, time steps, and considered wind scenarios. In Section 4.2.4, the chance constraint in (4.1m) will be further discussed. Lastly, (4.1n) enforces that $y_{l,t,s}$ is a binary variable.

4.2.3 Wind Forecast Uncertainty

As mentioned in Section 4.2.2, the available wind power $\tilde{P}^{\text{wind}}_{w,t,s}$ can be represented as:

$$\tilde{P}^{\text{wind}}_{w,t,s} = P^{\text{f}}_{w,t} + P^{\text{e}}_{w,t,s}, \tag{4.2}$$

where $P^{\text{f}}_{w,t}$ is the wind forecast and $P^{\text{e}}_{w,t,s}$ is the forecast error. We assume the hourly wind forecast error is a random variable captured by a truncated Cauchy distribution, as demonstrated in [77, 78]. The Cauchy distribution is truncated such that its support is $[-C_w, +C_w]$, where C_w is the rated capacity of wind source $w \in \mathcal{W}$ (in MW). For each wind source $w \in \mathcal{W}$, the Cauchy distribution describing the wind forecast error has location parameter $x_0 = 0$ and scale parameter $\gamma_{w,t} = 0.15 \cdot P^{\text{f}}_{w,t}$. Note that the two-stage stochastic framework for flexible line limits we propose in this thesis is distribution agnostic due to the use of the SAA method.

4.2.4 Integer Chance Constraint Derivation

Next, we derive the SAA of the joint chance constraint in (4.1m) using the method described in Section 2.3.3. As in Section 2.3.3, we begin by defining the following events and their complements:

$$\begin{aligned}
E_{l,t} &= \{s \in \mathcal{S} :\ y_{l,t,s} = 0\}, && \forall l \in \mathcal{L}, \forall t \in \mathcal{T}, \\
E^{\text{C}}_{l,t} &= \{s \in \mathcal{S} :\ y_{l,t,s} = 1\}, && \forall l \in \mathcal{L}, \forall t \in \mathcal{T}, \\
H &= \bigcap_{t \in \mathcal{T}, l \in \mathcal{L}} E_{l,t}, \\
H^{\text{C}} &= \bigcup_{t \in \mathcal{T}, l \in \mathcal{L}} E^{\text{C}}_{l,t},
\end{aligned}$$

where $\mathcal{S}$ is the sample space, which we refer to as the set of scenarios, and $(\cdot)^{\text{C}}$ denotes the complement. Thus, $E_{l,t}$ is the set of wind scenarios such that line $l \in \mathcal{L}$ does not violate the continuous line rating at time $t \in \mathcal{T}$, and $E^{\text{C}}_{l,t}$ is the complement. Then, H is the collection of scenarios in the intersection of $E_{l,t}$ for all $l \in \mathcal{L}$ and $t \in \mathcal{T}$, and H^{C} is the collection of scenarios in the union of $E^{\text{C}}_{l,t}$ for all $l \in \mathcal{L}$ and $t \in \mathcal{T}$. In this work, we want to ensure that the probability

of nominal continuous line capacity rating $\overline{F}_l$ violations is limited to at most ϵ across all lines, all time steps in the simulation, and all possible wind scenarios. As shown in Section 2.3.3, this is equivalent to:

$$\Pr(H^{\mathrm{C}}) \leq \epsilon. \tag{4.3}$$

Then, following the steps for deriving the SAA of an integer chance constraint described in Section 2.3.3, we obtain:

$$\frac{1}{|\mathcal{T}||\mathcal{L}||\mathcal{S}|} \sum_{s\in\mathcal{S}} \sum_{t\in\mathcal{T}} \sum_{l\in\mathcal{L}} y_{l,t,s} \leq \epsilon. \tag{4.4}$$

Thus, we replace (4.1m) with the SAA in (4.4) above.

4.3 Case Study: RTS-GMLC Test System with Flexible Line Flow Ratings

In this section, we provide simulation results for the two-stage stochastic program with 100 wind scenarios on the 73-bus RTS-GMLC test system [70]. We simulate a futuristic high-wind scenario where the system experiences transmission congestion, the active power demand at each bus is increased by 35%, and the capacity of each wind source is doubled. A visualization of the RTS-GMLC test system is shown in Fig. 4.1. For the discussions in this section, and to be consistent with the RTS-GMLC test system, note that buses with labels that begin with a '1', '2', or '3' belong to Area 1, 2, or 3, respectively. Similarly, lines that begin with an 'A', 'B', or 'C' belong to Area 1, 2, or 3, respectively. The RTS-GMLC test system is a natural choice for studying the proposed flexible line flow rating model in (4.1) because Area 3 has a high concentration of renewable energy resources compared to the other two areas. The available wind source forecasts are shown in Fig. 4.2.

The stochastic optimization problem is implemented in Pyomo [79], and uses the RTS-GMLC data parser and other calculation functions from EGRET [80]. We solve the proposed two-stage optimization problem in (4.1), a mixed-integer linear program (MILP), using an academic Gurobi 8.1.1 license [81]. For the simulations provided, we use a 24 hour planning horizon with hourly

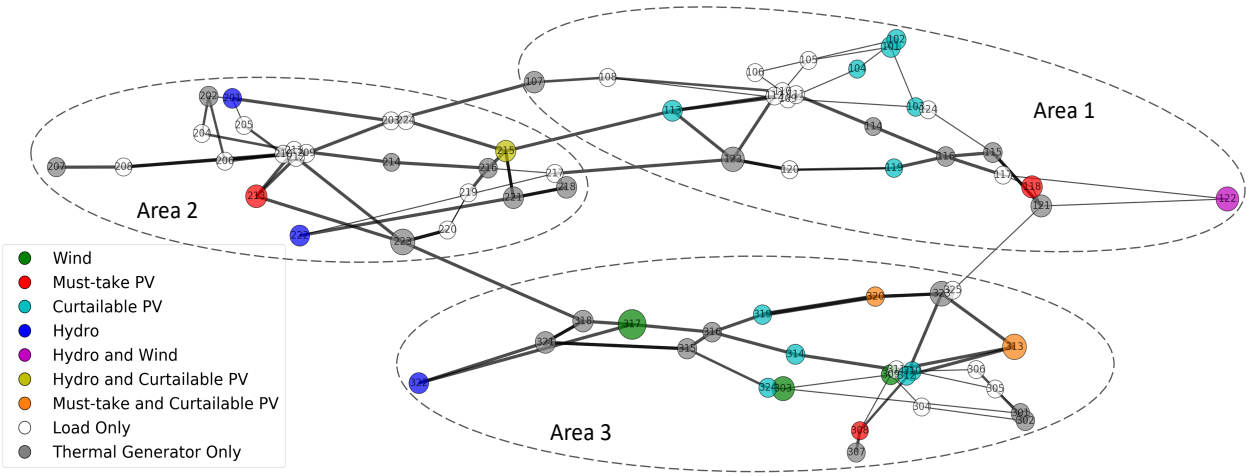

Figure 4.1: The 73-bus RTS-GMLC test system. The network has 3 areas and consists of 120 lines, 76 thermal generators, 76 renewable energy sources, and 4 wind sources. Each node represents a bus, and the node color represents the type of renewable energy source located at that bus. Note that buses can contain multiple types of generation sources. The node size is proportional to the generating capacity at that bus for the August day used in these simulations. The line thickness corresponds to the line rating capacity.

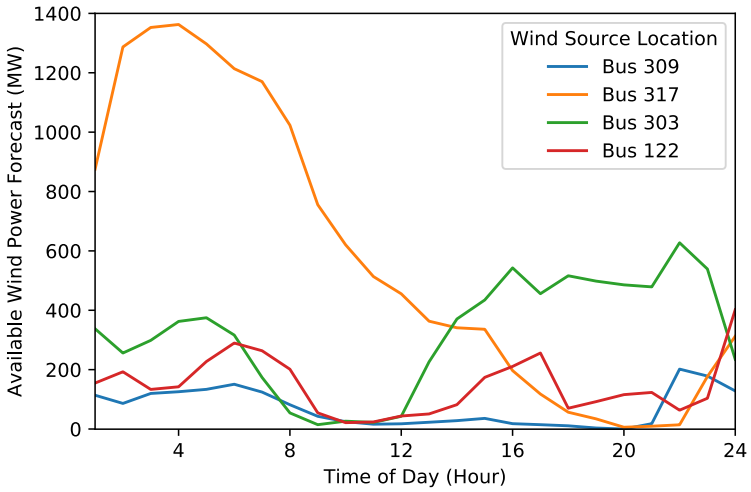

Figure 4.2: Available wind power forecast for each wind source in the RTS GMLC test system.

time steps. The simulations in this work were performed on a computer with a 2.4 GHz Intel core processor with 8 GB of RAM. All simulations are solved to a MIP optimality gap of 0.1% (0.001) and each simulation took less than 10 minutes to complete.

We provide simulations results for the problem formulation in (4.1) for both $\epsilon = 0.01$ and $\epsilon = 0.05$, where ϵ is the probability of continuous power flow rating violations across all lines, time steps, and wind scenarios. In Table 4.2, we compare the number of continuous line rating violations when $\epsilon = 0.01$ and $\epsilon = 0.05$ across all time periods and considered scenarios for each line. Note that lines not included in Table 4.2 never violated their continuous rating, i.e., $-\overline{F}_l \leq p_l^{t,s} \leq \overline{F}_l$ for all times and all considered scenarios. From Table 4.2, we can see that some of the lines that experience temporary line capacity violations connect buses with wind sources. Furthermore, when ϵ is relaxed from 0.01 to 0.05, we see that the total number of violations increase, as expected. The SAA of the joint chance constraint in (4.4) is binding when $\epsilon = 0.01$ since the sum of violations in column 2 of Table 4.2 is equal to $\epsilon|\mathcal{L}||\mathcal{T}||\mathcal{S}|$, and (4.4) is not binding when $\epsilon = 0.05$. Furthermore, Table 4.2 shows that the majority of the violations are lines connected to wind sources and the line CB-1. Line CB-1, which links Area 3 to Area 2, experiences transmission line capacity increases above its nominal limit in order to transport the excess power from wind sources to other areas of the network with less distributed renewable and wind sources. Also in Table 4.2, notice that there are no lines connected to the wind source at bus 122 that experience line violations, which is likely due to the lack of distributed renewable and wind sources in Area 1 compared to Area 3.

Table 4.2: Number of continuous line rating violations across all times and considered wind scenarios for both $\epsilon = 0.01$ and $\epsilon = 0.05$. Both the origin and destination bus labels are given, where **bold** bus labels indicate there is a wind source at that bus.

Line l (origin bus, destination bus)	$\sum_{t\in\mathcal{T}}\sum_{s\in\mathcal{S}} y_{l,t,s}$	
	$\epsilon = 0.01$	$\epsilon = 0.05$
B12-1 (208, 209)	300	300
C6 (**303**, **309**)	708	780
C27 (316, **317**)	165	210
C29 (**317**, 318)	653	698
CB-1 (318, 223)	1054	1099
Total Violations	2880	3087

For the lines in Table 4.2, we show the number of violations as a function of time in Fig. 4.3 for

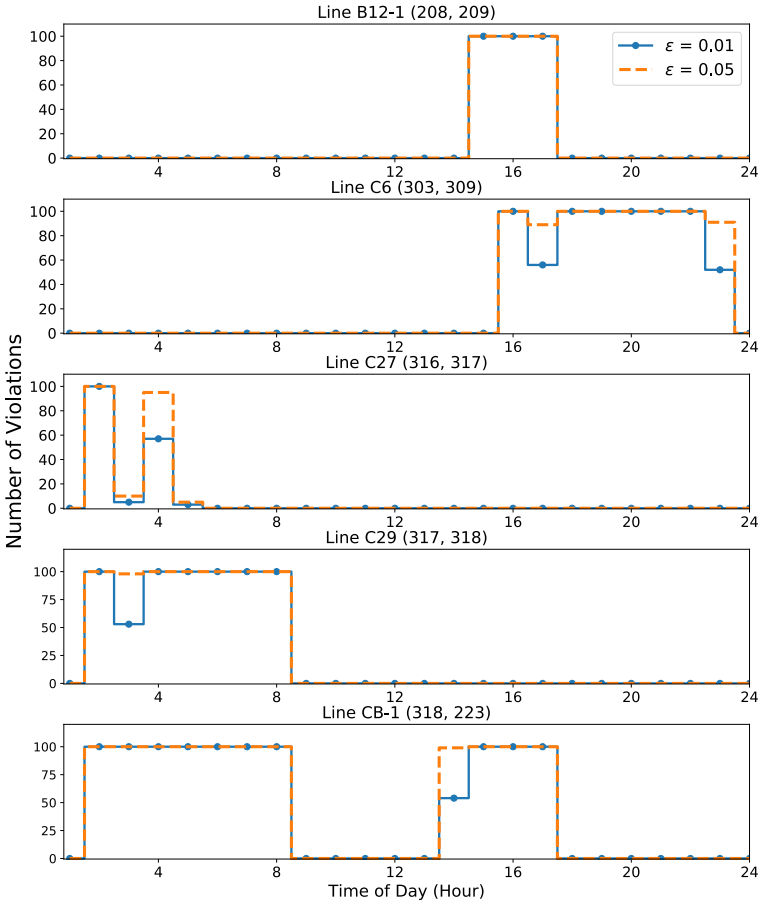

Figure 4.3: Number of continuous line rating violations at each time in the planning horizon for lines when $\epsilon = 0.01$ and $\epsilon = 0.05$. Each of the included lines are also referenced in Table 4.2.

both $\epsilon = 0.01$ and $\epsilon = 0.05$. Fig. 4.3 demonstrates that, as the probability of continuous line rating violations is relaxed, the number of violations increase during times of high wind availability. The violations seen in Fig. 4.3 for lines C27 and C29, which are both connected to bus 317, correlate with times of high wind availability for the wind source at bus 317, as seen in the forecasts in Fig. 4.2. Similarly, the line violations for line C6, which is connected to the wind sources at bus 303 and 309, correspond to times with increased wind generation, as seen from both Figs. 4.2 and 4.3 together. Line CB-1 experiences violations during both times of increased wind generation in the early morning and afternoon hours in order to transport excess wind power generation from

Area 3 to Area 2.

Table 4.3: Comparison of wind power curtailment for each wind source with flexible line capacity ratings and fixed line capacity ratings. Sum of wind power curtailment for each wind source over all scenarios in the simulation planning horizon (MW).

Wind Location (bus)	$\sum_{t\in\mathcal{T}}\sum_{s\in\mathcal{S}} P^{c}_{w,t,s}$		
	$\epsilon = 0.01$	$\epsilon = 0.05$	Fixed Rating: $-\overline{F}_l \leq p_{l,t,s} \leq \overline{F}_l$
303	85.40	19.60	136.10
309	89.12	3.81	143.45
317	1590.77	1534.37	2887.36
122	227.82	435.24	156.68

Next, we demonstrate that allowing temporary violations of continuous line flow ratings minimizes the curtailment of available wind power. We compare the average wind power curtailment with the proposed flexible line flow limits and with the flow limits fixed at the continuous line flow rating $\overline{F}_l$ with the same 100 wind scenarios, i.e., we replace constraints (4.1k)-(4.1n) with $-\overline{F}_l \leq p_l^{t,s} \leq \overline{F}_l$ for all $l \in \mathcal{L},\ t \in \mathcal{T},\ s \in \mathcal{S}$. Table 4.3 gives the sum of the average wind power curtailment over all wind scenarios at each time step in the simulation. For the wind sources in Area 3 shown in Table 4.3, when we allow flexible line flow ratings, we see that the wind curtailment is less than when the line flow ratings are fixed at the continuous rating. In other words, wind curtailment in the flexible line rating cases ($\epsilon = 0.01$ and $\epsilon = 0.05$) is less than the wind curtailment observed with fixed line ratings in the congested area of the network. When we compare the wind curtailment between the flexible line flow cases for $\epsilon = 0.01$ and $\epsilon = 0.05$ in Table 4.3, we see that curtailment decreases when the probability of violating the continuous line rating increases in Area 3, as expected since the number of violations can increase. The wind source at bus 122 in Area 1 does not experience the same curtailment pattern as seen for the wind sources in Area 3 in Table 4.3, which is likely due to less congestion in Area 1 as a result of less distributed renewable energy sources. In total, the proposed method with flexible line flow ratings results in 40.03% less wind energy curtailment and 0.67% reduction in conventional generation dispatch costs compared

to when the line ratings are fixed at their nominal continuous rating.

4.4 Discussion and Conclusions

A two-stage stochastic optimal power flow problem with flexible line ratings is proposed to address uncertainty in wind power forecasts, alleviate line congestion, and minimize wind power curtailment. We use the SAA of a joint chance constraint that limits the probability of continuous line rating violations across all considered wind scenarios, all times in the simulation, and all lines in the network. We provide simulation results on the RTS GMLC test system showing that flexible line limits minimize the wind power curtailment in a congested area of the network with a large amount of distributed renewable and wind sources. By allowing violations of the nominal continuous line rating with some low probability, wind power that would have been otherwise curtailed is exported to other parts of the network to satisfy the power demand. We show that lines that experience violations and the occurrence of those violations correspond to the wind source location and the times of high wind generation. Lastly, the majority of continuous line rating violations occur on lines in Area 3 and on a line that connects Area 3 to Area 2, which transports the excess wind generation to other parts of the network with less distributed renewable sources and wind sources.

Chapter 5

Optimality Guarantees for Models with Complementarity Constraints in Energy Systems

This chapter presents theoretical analysis that guarantees proper model behavior for relaxed convex models commonly found in power and energy optimization problems. The focus of this work is primarily on grid-connected electrical ESS models, where the non-convex complementarity constraint is omitted from the optimization model using a penalty reformulation approach. In a BTM setting, theoretical analysis for omitting the complementarity constraint in feed-in tariff models is also provided. The optimality guarantees for the ESS model are proven for an energy management system setting under various EMS-to-grid interaction scenarios, an transmission setting with a linear power flow approximation (DC OPF), and in a distribution setting with a second-order cone relaxation of AC OPF. For each setting, numerical case studies are provided to demonstrate the proper behavior of the relaxed convex models.

5.1 Models with Complementarity Constraints in Energy Systems

Models commonly found in energy system optimization problems often include a non-convex complementarity constraint, which ensure two modes of operation cannot happen simultaneously in a given model. In particular, we are interested in grid-connected ESS models that include a complementarity constraint to ensure that the optimization does not produce a physically unrealizable control policy where the ESS simultaneously charges and discharges. Ensuring proper ESS model behavior in optimization problems is important because ESSs are widely included in research on

renewable energy integration and power grid resiliency. ESSs are a valuable asset for stable renewable energy integration into the grid since they can act as a generation source and simultaneously provide other valuable demand-side grid services, such as energy arbitrage, power quality and reliability, storing excess renewable energy generation, and electricity bill management [11, 13]. These benefits are driving rapid adoption of ESSs both in front of and behind the meter [82]. And due to recent regulations in the United States [83], ESSs are expected to increasingly participate in grid operations. For all these reasons, it is important to efficiently and accurately compute optimal ESS operation.

Let $t \in \mathcal{T}$ be the set of discrete time steps and let $e \in \mathcal{E}$ be the set of ESSs in a system. The following convex ESS model will be the main focus of the theoretical analysis in this chapter:

$$E_{e,t+1} = E_{e,t} + \Delta t\big(\eta_e^{\text{ch}} P_{e,t}^{\text{ch}} - \tfrac{1}{\eta_e^{\text{dis}}} P_{e,t}^{\text{dis}}\big), \qquad \forall e \in \mathcal{E}, \forall t \in \mathcal{T}, \tag{5.1a}$$

$$\underline{E}_e \leq E_{e,t+1} \leq \overline{E}_e, \qquad \forall e \in \mathcal{E}, \forall t \in \mathcal{T}, \tag{5.1b}$$

$$0 \leq P_{e,t}^{\text{ch}} \leq \overline{P}_e^{\text{ch}}, \qquad \forall e \in \mathcal{E}, \forall t \in \mathcal{T}, \tag{5.1c}$$

$$0 \leq P_{e,t}^{\text{dis}} \leq \overline{P}_e^{\text{dis}}, \qquad \forall e \in \mathcal{E}, \forall t \in \mathcal{T}. \tag{5.1d}$$

The ESS state of charge dynamics is given in (5.1a), where the charging and discharging efficiencies are such that $0 < \eta_e^{\text{ch}}, \eta_e^{\text{dis}} < 1$. Notice that this ESS model has separate terms for ESS charging and discharging, i.e., $P_{e,t}^{\text{ch}}$ and $P_{e,t}^{\text{dis}}$, which captures a more realistic round-trip efficiency by accounting for losses in ESS-to-grid interactions [11]. The ESS state of charge (SOC) is constrained between the minimum and maximum SOC limits in (5.1b). The charging and discharging limits are enforced in (5.1c) and (5.1d), respectively.

Ensuring proper ESS dynamics in (5.1), i.e., ensuring the model does not allow the optimization to produce a physically unrealizable optimal control policy where the ESS simultaneously charges and discharges, is often achieved by including the non-convex complementarity constraint:

$$P_{e,t}^{\text{ch}} \cdot P_{e,t}^{\text{dis}} = 0, \quad \forall e \in \mathcal{E}, \forall t \in \mathcal{T}. \tag{5.2}$$

The complementarity constraint in (5.2) ensures that $P_{e,t}^{\text{ch}}$ and $P_{e,t}^{\text{dis}}$ cannot simultaneously both be

non-zero. The computational challenges associated with including the complementarity constraint in (5.2) are discussed in Section 2.2. Alternatively, the complementarity constraint in (5.2) can be enforced by modifying (5.1) to include binary variables. The authors in [56, 60, 84–88] (and many others) adopt an ESS model with binary variables in their research to guarantee optimal solutions obey proper non-simultaneous charging and discharging constraints. However, introducing binary variables into an optimization problem requires the use of a mixed integer programming (MIP) solver and may be computationally limiting depending on the size of the optimization problem.

The convex ESS model in (5.1) with the complementarity constraint omitted is widely used in power system optimization research, as seen in [6,62,89] (and many others); however, the authors do not comment on whether they can guarantee proper ESS behavior. When the complementarity constraint is omitted, situations arise when the optimization can result in an optimal control policy where the ESS simultaneously charges and discharges. Thus, this chapter focuses on providing theoretical analysis that guarantees an optimization problem that includes the ESS model in (5.1) with the complementarity constraint in (5.2) omitted will not produce an optimal solution with simultaneous ESS charging and discharging. To achieve this, we use a penalty reformulation approach, similar to the penalty reformulation approach introduced in Section 2.2, in order to omit the non-convex complementarity constraint. Thus, the following linear penalty on ESS charging and discharging: $\sum_{e\in\mathcal{E}}\sum_{t\in\mathcal{T}}(\alpha_e P^{\text{ch}}_{e,t}+\beta_e P^{\text{dis}}_{e,t})$, where $\alpha_e \geq 0$, $\beta_e \geq 0$, and $(\alpha_e+\beta_e) > 0$ for all $e \in \mathcal{E}$, is added to the objective in each of the grid settings described in this chapter. Notice that this implies the optimization objective only needs to penalize either charging or discharging in practice. The ESS charging and discharging penalties α_e and β_e can be used to capture the lifetime cost of charging and discharging the ESS, respectively. Other ESS lifetime prediction considerations are presented in [90, 91].

Similarly, in BTM settings, a non-convex complementarity constraint also arises when modeling the electricity price in a feed-in tariff (FiT) pricing situation to ensure that the EMS cannot physically simultaneously buy and sell power through a single service entrance. In Section 5.2, we will provide analysis for omitting the complementarity constraint in this model as well.

Previous studies have shown situations when the complementarity constraint can be omitted in optimization problems that include the ESS model in (5.1) [89,91–95]. A similar penalty reformulation approach was suggested by the authors in [92] for ESS models in a load-leveling optimization model. We extend their work by providing theoretical guarantees for a convex relaxed ESS model in three additional settings beyond load-leveling. In an economic dispatch setting, the authors in [93] present theoretical analysis ensuring non-simultaneous ESS charging and discharging using a similar penalty approach. For an SDP relaxation of the optimal power flow problem (OPF) for transmission, the authors in [94] show that the complementarity constraint in the ESS model can be omitted when the locational marginal prices (LMP's) are positive. This thesis extends the work in [94] by using a linear penalty reformulation approach to guarantee proper convex ESS model behavior even when the LMP's are not strictly positive. The authors in [89] provide analysis on simultaneous charging and discharging for the ESS model in (5.1) for a distributed power system with multiple grid-connected storage systems, but do not model power flows. They also identify the situations where simultaneous ESS charging is observed, i.e., when the optimization cannot further reduce dispatchable generation supply and the ESSs are all at their maximum capacity. For these situations, the penalty approach presented in this thesis is able to successfully guarantee an ESS model will not provide an optimal solution will exhibit simultaneous ESS charging and discharging. In [91], the authors suggest a penalty approach similar to the one we suggest in Section 5.2 in order to omit the complementarity constraint in (5.2). The work in this chapter generalizes the penalty approach suggested in [91] by offering simple conditions the penalty approach must satisfy. The authors in [95] provide similar theoretical results for ESS behavior when the complementarity constraint is omitted in a distribution setting when formulated as a second order cone program (SOCP). This chapter extends the results in [89, 91–95] to BTM EMS settings [21], transmission settings for DC OPF [20], and distribution settings for the SOCP relaxation of AC OPF. In each setting, the theoretical results maintain generality to ensure they can be applied to many situations with various objectives, as well as when there are multiple ESSs in a system or at each bus. In the BTM EMS setting, the omission of a complementarity constraint ensuring proper feed-in tariff

(FiT) model behavior is also studied. Numerical case studies are provided for each situation to highlight the theoretical guarantees.

5.2 Guarantees for Complementarity Constraints in Energy Management Systems

An ESS is often at the core of many EMSs since they can act as a generation source and simultaneously provide other valuable demand-side grid services, such as energy arbitrage, power quality and reliability, storing excess renewable energy generation, and electricity bill management [11, 13]. Thus, we seek to use the convex relaxed ESS model in BTM EMS settings. Similarly, a non-convex complementarity constraint also arises when modeling the electricity price in a feed-in tariff (FiT) pricing situation to ensure that the EMS cannot simultaneously buy and sell power through a single service entrance. To address this, we propose an EMS formulation that includes a relaxed convex ESS model and FiT pricing model, i.e., the non-convex complementarity constraints are omitted from the overall EMS model. We provide theoretical analysis that guarantees proper model behavior for the relaxed convex ESS and FiT models in an EMS. In this work, we adopt a general definition of an EMS, where the EMS manages available renewable energy generation, ESS operation, and electricity drawn from and sold to the grid while satisfying the electricity demand to minimize the cost of electricity. This general definition permits use of the EMS model in diverse settings–such as a home, building, or microgrid–and under various electricity rate/cost structures. In this paper we consider two EMS-to-grid interaction scenarios. In the first, the site is permitted to both draw from and export power to the grid. In the second, the site is prohibited from exporting. These broad scenarios allow us to demonstrate elimination of typical complementarity constraints, modeling of the overall problem, and what guarantees can be provided. Notice that the second scenario captures a situation where the EMS is coordinating electricity for an islanded microgrid, where electricity drawn from the grid represents electricity generated from a dispatchable generation source, for example. For each scenario, we present theoretical analysis for proper relaxed convex model behavior both static and flexible load, and under multiple types of electricity pricing

including time-of-use (TOU) rates, demand charges, net metering, and feed-in tariffs.

5.2.1 Energy Management System Formulation

Next, the general convex EMS formulations are provided for each scenario with both static and flexible load, and under multiple types of electricity pricing. The relevant notation for the following convex EMS models is given in Table 5.1. For the following discussion, let the set of discrete time steps $\{1, \ldots, H\}$ be denoted $\mathcal{T}$. Also let the EMS optimization variables for all time t be collected in the vector $\underline{\mathbf{x}}_H = [\mathbf{x}_1 \ \mathbf{x}_2 \ \ldots \ \mathbf{x}_H]$ where $\mathbf{x}_t$ collects the optimization variables associated to time t.

Table 5.1: Notation for convex EMS models.

	Sets
$e \in \mathcal{E}$	Set of energy storage systems
$t \in \mathcal{T}$	Hourly time steps: $1, \ldots, H$
	Decision Variables
$E_{e,t}$	State of charge of ESS e (kWh)
P_t^{c}	Curtailed renewable power generation (kW)
$P_{e,t}^{\mathrm{ch}}$	Power injected into ESS e (kW)
$P_{e,t}^{\mathrm{dis}}$	Power drawn from ESS e (kW)
P_t^{exp}	Power exported to the grid (kW)
P_t^{grid}	Power drawn from the grid (kW)
P^{flx}	Flexible, shifted load (kW)
	Parameters
c^{d}	Cost of electricity drawn from grid ($/kWh)
c^{e}	Payment for electricity sold to grid ($/kWh)
c^{dc}	Demand charge cost ($/kWh)
γ	Fraction of load that is sheddable
E_e^{init}	Initial state of charge of ESS e (kWh)
$\overline{E}_e$	Maximum energy storage in ESS e (kWh)
$\underline{E}_e$	Minimum energy storage in ESS e (kWh)
η_e^{ch}	Charging efficiency of ESS e
η_e^{dis}	Discharging efficiency of ESS e
H	Optimization planning horizon
$\overline{P}_e$	Maximum charging/discharging power of ESS e (kW)
P_t^{res}	Available power renewable energy source (kW)
P_t^{L}	Total load b (kW)
ρ	Inconvenience penalty for shedding load

5.2.1.1 EMS-to-Grid Scenario 1: Buying and Selling Electricity

EMS-to-grid Scenario 1 is considered in both a net metering and FiT setting. First we model the net metering setting, where we assume the cost of drawing electricity from the grid is equal to the amount the customer is compensated for selling (or exporting) electricity to the grid. Then, the optimization objective function is:

$$f_1^{\text{obj}}(\underline{\mathbf{x}}_H) = \sum_{t=1}^{H} \left(c_t^{\text{d}} P_t^{\text{grid}} + \sum_{e \in \mathcal{E}} \left(\alpha_e P_{e,t}^{\text{ch}} + \beta_e P_{e,t}^{\text{dis}} \right) \right), \tag{5.3}$$

which captures both the cost of electricity and the ESS penalty terms. The overall general EMS formulation for net metering, denoted NM-G, is:

$$\min_{\underline{\mathbf{x}}_H} f_1^{\text{obj}}(\underline{\mathbf{x}}_H) \tag{5.4a}$$

$$\text{s.t. } (5.1\text{a}) - (5.1\text{d}),$$

$$0 \leq P_t^{\text{c}} \leq P_t^{\text{res}}, \qquad \forall t \in \mathcal{T}, \tag{5.4b}$$

$$P_t^{\text{L}} - P_t^{\text{grid}} - P_t^{\text{res}} + P_t^{\text{c}} + \sum_{e \in \mathcal{E}} (P_{e,t}^{\text{ch}} - P_{e,t}^{\text{dis}}) = 0, \qquad \forall t \in \mathcal{T}. \tag{5.4c}$$

The EMS objective function in (5.4a) minimizes the cost of electricity and includes the linear ESS penalty described above, where $c_t^{\text{d}} \geq 0$ is the unit cost or compensation to the customer based on whether the EMS is drawing ($P_t^{\text{grid}} > 0$) or exporting ($P_t^{\text{grid}} < 0$) electricity to the grid. Note that in a net metering setting, $c_t^{\text{e}} = c_t^{\text{d}}$ for all $t \in \mathcal{T}$. The convex ESS model with the complementarity constraint omitted is given by (5.1a)-(5.1d). Curtailment of renewable energy generation is included in (5.4b) and the power balance is enforced in (5.4c).

Next, the EMS is formulated for FiT electricity pricing, where a consumer can provide a grid service by exporting excess electricity produced at a price strictly less than the price of electricity drawn from the grid, i.e., $c_t^{\text{d}} > c_t^{\text{e}} \geq 0$. Then, the optimization objective function is:

$$f_2^{\text{obj}}(\underline{\mathbf{x}}_H) = \sum_{t=1}^{H} \left(c_t^{\text{d}} P_t^{\text{grid}} - c_t^{\text{e}} P_t^{\text{exp}} + \sum_{e \in \mathcal{E}} (\alpha_e P_{e,t}^{\text{ch}} + \beta_e P_{e,t}^{\text{dis}}) \right), \tag{5.5}$$

which captures both the cost of buying electricity and the compensation for selling electricity, and the ESS penalty terms. Then, the overall general EMS formulation under FiT pricing, denoted

FiT-G, is:

$$\min_{\underline{\mathbf{x}}_H} f_2^{\text{obj}}(\underline{\mathbf{x}}_H) \tag{5.6a}$$

$$\text{s.t. } (5.1\text{a}) - (5.1\text{d}),$$

$$0 \leq P_t^{\text{grid}}, \qquad \forall t \in \mathcal{T}, \tag{5.6b}$$

$$0 \leq P_t^{\text{exp}}, \qquad \forall t \in \mathcal{T}, \tag{5.6c}$$

$$0 \leq P_t^{\text{c}} \leq P_t^{\text{res}}, \qquad \forall t \in \mathcal{T}, \tag{5.6d}$$

$$P_t^{\text{L}} + P_t^{\text{exp}} - P_t^{\text{grid}} - P_t^{\text{res}} + P_t^{\text{c}} + \sum_{e \in \mathcal{E}} (P_{e,t}^{\text{ch}} - P_{e,t}^{\text{dis}}) = 0, \qquad \forall t \in \mathcal{T}. \tag{5.6e}$$

The EMS objective function in (5.6a) minimizes the cost of electricity and includes the ESS penalty, where c_t^{d} is the unit cost of drawing electricity from the grid and c_t^{e} is compensation to the customer for exporting electricity to the grid. The convex ESS model with the complementarity constraint omitted is given by (5.1a)-(5.1d). The power drawn from the grid and the excess power exported to the grid is represented by two variables, P_t^{grid} and P_t^{exp}, respectively, as seen in (5.6b)-(5.6c). The power balance is enforced in (5.6e). Furthermore, the EMS formulation should not produce an optimal solution where the EMS draws and exports electricity to the grid simultaneously, which could be enforced by including the constraint:

$$P_t^{\text{grid}} \cdot P_t^{\text{exp}} = 0, \quad \forall t \in \mathcal{T}. \tag{5.7}$$

Notice that (5.7) is a non-convex complementarity constraint and is omitted in (5.6) in order to preserve the convexity of the overall EMS optimization model. As with the ESS complementarity constraint, the FiT constraint in (5.7) can also be enforced by including binary variables [96, 97]; however, we focus on the convex relaxation in this paper where a reformulation with binary variables is not used and (5.7) is omitted. In Section 5.2.2, we formally provide conditions and prove that any optimal solution to (5.6) obeys (5.7) while not explicitly including it in the EMS formulation or introducing binary variables.

5.2.1.2 EMS-to-Grid Scenario 2: Buying Electricity Only

Next, the overall convex EMS optimization model is given for EMS-to-grid Scenario 2, where the EMS can only draw electricity from the grid. The general convex EMS formulation for Scenario 2, denoted S2-G, is:

$$\min_{\underline{\mathbf{x}}_H} f_1^{\text{obj}}(\underline{\mathbf{x}}_H) \tag{5.8a}$$

$$\text{s.t. } (5.1\text{a}) - (5.1\text{d}),$$

$$0 \leq P_t^{\text{grid}}, \qquad \forall t \in \mathcal{T}, \tag{5.8b}$$

$$0 \leq P_t^{\text{c}} \leq P_t^{\text{res}}, \qquad \forall t \in \mathcal{T}, \tag{5.8c}$$

$$P_t^{\text{L}} - P_t^{\text{grid}} - P_t^{\text{res}} + P_t^{\text{c}} + \sum_{e \in \mathcal{E}} (P_{e,t}^{\text{ch}} - P_{e,t}^{\text{dis}}) = 0, \qquad \forall t \in \mathcal{T}. \tag{5.8d}$$

Since excess power generation is not able to be exported to the grid in EMS-to-grid Scenario 2, the power drawn from the grid is constrained to be non-negative in (5.8b) and curtailment of renewable energy generation is included in (5.8c). The power balance is given in (5.8d).

5.2.1.3 EMS Models for Various Electricity Pricing Settings

The theoretical results for omitting complementarity constraints are also presented for the case that the EMS models given in (5.4), (5.6), (5.8) can be modified to capture additional electricity pricing settings. Notice that each EMS model is based on a time-varying cost of electricity, i.e. c_t^{d} and c_t^{e} are indexed by time t. The general EMS models already capture settings where TOU electricity prices, or other time-varying electricity price schedules, are used.

Any of the EMS optimization models in (5.4), (5.6), (5.8) can be slightly modified to accommodate demand charges where customers are charged a separate rate for their peak usage over a given time interval, i.e., a cost of $c^{\text{dc}} \max_{t \in \mathcal{T}} \{P_1^{\text{grid}}, \ldots, P_H^{\text{grid}}\}$ is added to the customer bill where $c^{\text{dc}} > 0$. This max term incorporated into the convex EMS formulation using epigraph form. Define a new decision variable d. Then, for an EMS optimization model with a demand charge, the

objective functions become:

$$f_1^{\text{obj}-\text{D}}(\underline{\mathbf{x}}_H) = \sum_{t=1}^{H} \left(c_t^{\text{d}} P_t^{\text{grid}} + \sum_{e \in \mathcal{E}} \left(\alpha_e P_{e,t}^{\text{ch}} + \beta_e P_{e,t}^{\text{dis}} \right) \right) + c^{\text{dc}} d, \tag{5.9}$$

$$f_2^{\text{obj}-\text{D}}(\underline{\mathbf{x}}_H) = \sum_{t=1}^{H} \left(c_t^{\text{d}} P_t^{\text{grid}} - c_t^{\text{e}} P_t^{\text{exp}} + \sum_{e \in \mathcal{E}} (\alpha_e P_{e,t}^{\text{ch}} + \beta_e P_{e,t}^{\text{dis}}) \right) + c^{\text{dc}} d, \tag{5.10}$$

and the following constraints are added to the overall EMS optimization problem:

$$P_t^{\text{grid}} \leq d, \quad \forall t \in \mathcal{T}. \tag{5.11a}$$

In the net metering case, we add the additional constraint:

$$0 \leq d, \tag{5.11b}$$

to ensure that the demand charge is only applied to power drawn from the grid, i.e., when $P_t^{\text{grid}} \geq 0$. When a general EMS formulation is modified to include demand charges, the resulting overall optimization model is denoted by adding '-D', e.g., NM-G with the demand charge model will be denoted NM-D.

5.2.1.4 EMS Models with Flexible Demand

Lastly, we introduce a further modification to the general convex EMS formulations in (5.4), (5.6), (5.8) where the electrical load is flexible, i.e., some amount of the non-critical load can either be shedded or added at each time step. Our theoretical analysis for convex EMS models without complementarity constraints will also extend to the case when the EMS can coordinate flexible load. To add flexible load scheduling to any of the generic formulations in (5.4), (5.6), (5.8), we first introduce a new variable P_t^{flx}, where load is shed when $P_t^{\text{flx}} > 0$ and load is added when $P_t^{\text{flx}} < 0$. Let $f_t^{\text{pb}}(\mathbf{x}_t)$ denote the left-hand-side of the power balance of the general EMS model that is being modified to include flexible demand constraints. In the flexible demand case, the

following constraints are added to the optimization problem:

$$P_t^{\text{flx}} \leq \gamma_t P_t^{\text{L}}, \qquad \forall t \in \mathcal{T}, \tag{5.12a}$$

$$\sum_{t \in \mathcal{T}} P_t^{\text{flx}} = 0, \tag{5.12b}$$

$$f_t^{\text{pb}}(\mathbf{x}_t) - P_t^{\text{flx}} = 0, \qquad \forall t \in \mathcal{T}. \tag{5.12c}$$

The constraint in (5.12a) ensures that only $\gamma_t \in [0, 1]$ proportion of the load is sheddable at each time step, i.e., $(1 - \gamma_t)$ of the demand is critical and cannot be shed. The constraint in (5.12b) ensures that the shedded loads are shifted to other time steps in the optimization horizon. When an EMS model is modified to allow shiftable load, the left-hand side of the original power balance equality constraint $f_t^{\text{pb}}(\mathbf{x}_t)$ must be modified to include the term $-P_t^{\text{flx}}$, as shown in (5.12c). A penalty ρ_t associated with the inconvenience of shedding load, i.e., when $P_t^{\text{flx}} > 0$, is added to the EMS objective function: $\sum_{t \in \mathcal{T}} \rho_t \max\{0, P_t^{\text{flx}}\}$. This max term is implemented using epigraph form, where a new variable s_t is introduced. Then, for an EMS optimization model with flexible load, the objective functions become:

$$f_1^{\text{obj}-\text{F}}(\underline{\mathbf{x}}_H) = \sum_{t=1}^{H} \left(c_t^{\text{d}} P_t^{\text{grid}} + \rho_t s_t + \sum_{e \in \mathcal{E}} \left(\alpha_e P_{e,t}^{\text{ch}} + \beta_e P_{e,t}^{\text{dis}} \right) \right), \tag{5.12d}$$

$$f_2^{\text{obj}-\text{F}}(\underline{\mathbf{x}}_H) = \sum_{t=1}^{H} \left(c_t^{\text{d}} P_t^{\text{grid}} - c_t^{\text{e}} P_t^{\text{exp}} + \rho_t s_t + \sum_{e \in \mathcal{E}} (\alpha_e P_{e,t}^{\text{ch}} + \beta_e P_{e,t}^{\text{dis}}) \right), \tag{5.12e}$$

and the following constraints are added to the overall EMS optimization problem:

$$0 \leq s_t \qquad \forall t \in \mathcal{T}, \tag{5.12f}$$

$$P_t^{\text{flx}} \leq s_t, \qquad \forall t \in \mathcal{T}. \tag{5.12g}$$

When a general EMS formulation is modified to include flexible demand, the resulting overall optimization model is denoted by adding '-F', e.g., if the flexible demand model is added to NM-G, it will be referred to as NM-F. Further, if both the demand charge model and flexible demand is considered, then the overall model will be referred to as NM-D-F.

5.2.2 Theoretical Guarantees for Relaxed Energy Management System Models with Complementarity Constraints

We formally prove that for each convex EMS formulation provided in Section 5.2.1, the optimal solution will satisfy the omitted non-convex constraints in (5.2) and (5.7) without explicitly including either in the EMS formulation. To aid in our theoretical analysis, we leverage the KKT optimality conditions. The KKT conditions provide necessary conditions that must be satisfied for a solution to a broad range of optimization problems to be optimal. For convex optimization problems with differentiable objective functions, any solution that satisfies the KKT conditions is optimal [22]. These conditions are leveraged to show that the optimal solutions of the convex EMS formulations in NM-all, FiT-all, and S2-all will obey the omitted non-convex constraints in (5.2) and (5.7), i.e., solutions that violate these non-convex constraints will violate the KKT conditions.

To aid in our discussion, let NM-all refer to all the net metering models {NM-G, NM-D, NM-F, NM-D-F}. Similarly, let FiT-all refer to {FiT-G, FiT-D, FiT-F, FiT-D-F} and S2-all refer to {S2-G, S2-D, S2-F, S2-D-F}. Additionally, To aid in the presentation of the KKT conditions, we introduce additional notation for describing the inequality and equality constraints in the convex EMS formulations given in Section 5.2.1. Writing each convex EMS formulation in standard form [22], we introduce the notation for the Lagrange multipliers associated with the inequality and equality constraints (written in standard form) in optimization models:

$$\underline{\lambda}_t^{\text{grid}} : -P_t^{\text{grid}} \leq 0, \tag{5.13a}$$

$$\underline{\lambda}_t^{\text{exp}} : -P_t^{\text{exp}} \leq 0, \tag{5.13b}$$

$$\underline{\lambda}_t^{\text{res}} : -P_t^{\text{c}} \leq 0, \tag{5.13c}$$

$$\overline{\lambda}_t^{\text{res}} : P_t^{\text{c}} - P_t^{\text{res}} \leq 0, \tag{5.13d}$$

$$\underline{\lambda}_{e,t}^{\text{ch}} : -P_{e,t}^{\text{ch}} \leq 0, \tag{5.13e}$$

$$\overline{\lambda}_{e,t}^{\text{ch}} : P_{e,t}^{\text{ch}} - \overline{P}_e^{\text{ch}} \leq 0, \tag{5.13f}$$

$$\underline{\lambda}_{e,t}^{\text{dis}} : -P_{e,t}^{\text{dis}} \leq 0, \tag{5.13g}$$

$$\overline{\lambda}^{\text{dis}}_{e,t} : P^{\text{dis}}_{e,t} - \overline{P}^{\text{dis}}_{e} \leq 0, \tag{5.13h}$$

$$\underline{\lambda}^{\text{soc}}_{e,t} : \underline{E}_{e} - E_{e,0} + \Delta t \sum_{n=1}^{t-1} \left(\tfrac{1}{\eta^{\text{dis}}_{e}} P^{\text{dis}}_{e,t} - \eta^{\text{ch}}_{e} P^{\text{ch}}_{e,t} \right) \leq 0, \tag{5.13i}$$

$$\overline{\lambda}^{\text{soc}}_{e,t} : E_{e,0} + \Delta t \sum_{n=1}^{t-1} \left(\eta^{\text{ch}}_{e} P^{\text{ch}}_{e,t} - \tfrac{1}{\eta^{\text{dis}}_{e}} P^{\text{dis}}_{e,t} \right) - \overline{E}_{e} \leq 0, \tag{5.13j}$$

$$\overline{\lambda}^{\text{flx}}_{t} : P^{\text{flx}}_{t} - \gamma_t P^{\text{L}}_{t} \leq 0, \tag{5.13k}$$

$$\lambda^{\text{flx1}}_{t} : -s_t \leq 0, \tag{5.13l}$$

$$\lambda^{\text{flx2}}_{t} : P^{\text{flx}}_{t} - s_t \leq 0, \tag{5.13m}$$

$$\lambda^{\text{dc1}} : -d \leq 0, \tag{5.13n}$$

$$\lambda^{\text{dc2}}_{t} : P^{\text{grid}}_{t} - d \leq 0, \tag{5.13o}$$

$$\mu^{\text{s}} : \sum_{t \in \mathcal{T}} P^{\text{flx}}_{t} = 0, \tag{5.13p}$$

$$\mu^{\text{pb}}_{t} : (5.4\text{c}), (5.6\text{e}), (5.8\text{d}), (5.12\text{c}), \tag{5.13q}$$

for all $t \in \mathcal{T}$ and $e \in \mathcal{E}$. For the KKT-based theoretical analysis used in our proofs, we write the stationarity constraint for each EMS formulation given in Section 5.2.1. The stationarity constraint for the NM-G EMS model is:

$$c^{\text{d}}_{t} - \mu^{\text{pb}}_{t} = 0, \qquad \forall t \in \mathcal{T}, \tag{5.14a}$$

$$-\underline{\lambda}^{\text{res}}_{t} + \overline{\lambda}^{\text{res}}_{t} + \mu^{\text{pb}}_{t} = 0, \qquad \forall t \in \mathcal{T}, \tag{5.14b}$$

$$\alpha_e - \underline{\lambda}^{\text{ch}}_{e,t} + \overline{\lambda}^{\text{ch}}_{e,t} + \eta^{\text{ch}}_{e} \Delta t \sum_{n=t}^{H} (\overline{\lambda}^{\text{soc}}_{e,n} - \underline{\lambda}^{\text{soc}}_{e,n}) + \mu^{\text{pb}}_{t} = 0, \qquad \forall e \in \mathcal{E}, \forall t \in \mathcal{T}, \tag{5.14c}$$

$$\beta_e - \underline{\lambda}^{\text{dis}}_{e,t} + \overline{\lambda}^{\text{dis}}_{e,t} + \frac{1}{\eta^{\text{dis}}_{e}} \Delta t \sum_{n=t}^{H} (\underline{\lambda}^{\text{soc}}_{e,n} - \overline{\lambda}^{\text{soc}}_{e,n}) - \mu^{\text{pb}}_{t} = 0, \qquad \forall e \in \mathcal{E}, \forall t \in \mathcal{T}. \tag{5.14d}$$

The stationarity constraint for the net metering EMS model with demand charges, NM-D, is:

$$c^{\text{d}}_{t} + \lambda^{\text{dc2}}_{t} - \mu^{\text{pb}}_{t} = 0, \qquad \forall t \in \mathcal{T}, \tag{5.15a}$$

$$c^{\text{dc}} - \lambda^{\text{dc1}} - \lambda^{\text{dc2}}_{t} = 0, \qquad \forall t \in \mathcal{T}, \tag{5.15b}$$

$$(5.14\text{b}) - (5.14\text{d}). \tag{5.15c}$$

The stationarity constraint for the net metering EMS model with flexible demand, NM-F, is:

$$\lambda_t^{\text{flx2}} + \overline{\lambda}_t^{\text{flx}} + \mu^{\text{s}} - \mu_t^{\text{pb}} = 0, \qquad \forall t \in \mathcal{T}, \tag{5.16a}$$

$$\rho_t - \lambda_t^{\text{flx1}} - \lambda_t^{\text{flx2}} = 0, \qquad \forall t \in \mathcal{T}, \tag{5.16b}$$

$$(5.14). \tag{5.16c}$$

The stationarity constraint for the net metering EMS model with both demand charges and flexible demand, NM-D-F, is:

$$(5.15), (5.16a) - (5.16b). \tag{5.17}$$

The stationarity constraint for the general FiT EMS model, FiT-G, is:

$$c_t^{\text{d}} - \underline{\lambda}_t^{\text{grid}} - \mu_t^{\text{pb}} = 0, \qquad \forall t \in \mathcal{T}, \tag{5.18a}$$

$$- c_t^{\text{e}} - \underline{\lambda}_t^{\text{exp}} + \mu_t^{\text{pb}} = 0, \qquad \forall t \in \mathcal{T}, \tag{5.18b}$$

$$(5.14\text{b}) - (5.14\text{d}). \tag{5.18c}$$

The stationarity constraint for the FiT EMS model with demand charges, FiT-D, is:

$$c_t^{\text{d}} - \underline{\lambda}_t^{\text{grid}} + \lambda_t^{\text{dc2}} - \mu_t^{\text{pb}} = 0, \qquad \forall t \in \mathcal{T}, \tag{5.19a}$$

$$c^{\text{dc}} - \lambda_t^{\text{dc2}} = 0, \qquad \forall t \in \mathcal{T}, \tag{5.19b}$$

$$(5.18\text{b}), (5.14\text{b}) - (5.14\text{d}). \tag{5.19c}$$

The stationarity constraint for the FiT EMS model with flexible demand, FiT-F, is given by (5.16a)-(5.16b) and (5.18). The stationary constraint for the FiT EMS model with both demand charges and flexible demand, FiT-D-F, is given by (5.16a)-(5.16b) and (5.19).

Lastly, the stationarity constraint for the Scenario 2 EMS models are given by:

(1) S2-G: (5.14b)-(5.14d),(5.18a),

(2) S2-D: (5.14b)-(5.14d),(5.19a)-(5.19b),

(3) S2-F: (5.14b)-(5.14d),(5.16a)-(5.16b),(5.18a),

(4) S2-D-F: (5.14b)-(5.14d),(5.16a)-(5.16b),(5.19a)-(5.19b).

Next, we provide a lemma to aid us in our theoretical analysis for the ESS model in (5.1). For the following analysis, let the optimal solution at some time $\tau \in \mathcal{T}$ in the planning horizon be denoted by $\tilde{\underline{\mathbf{x}}}_\tau$.

Lemma 5.1 Assume $\alpha_e, \beta_e \geq 0$, $(\alpha_e + \beta_e) > 0$, and $0 < \eta_e^{\text{ch}}, \eta_e^{\text{dis}} < 1$ for some ESS $e \in \mathcal{E}$. If $\mu_t^{\text{pb}} \geq 0$, then an optimal solution to any of the EMS models in NM-all, FiT-all, and S2-all will satisfy (5.2) for some time $t \in \mathcal{T}$, i.e., a solution where $0 < \tilde{P}_{e,t}^{\text{ch}} \leq \overline{P}_e^{\text{ch}}$ and $0 < \tilde{P}_{e,t}^{\text{dis}} \leq \overline{P}_e^{\text{dis}}$ will be suboptimal at time $t \in \mathcal{T}$ for ESS e.

Proof. We prove this claim by contradiction. So, assume an optimal solution to any of the EMS models NM-all, FiT-all, or S2-all is such that the constraint in (5.2) is *not* satisfied at some time $\tau \in \mathcal{T}$ and ESS $e \in \mathcal{E}$, i.e., $0 < \tilde{P}_{e,\tau}^{\text{ch}} \leq \overline{P}_e^{\text{ch}}$ and $0 < \tilde{P}_{e,\tau}^{\text{dis}} \leq \overline{P}_e^{\text{dis}}$. In other words, the convex EMS formulation produced an optimal solution where an ESS e simultaneously charging and discharging. Also, assume that $\mu_\tau^{\text{pb}} \geq 0$, as stated in the statement of the Lemma. By the complementary slackness conditions at time τ, we obtain that $\underline{\lambda}_{e,\tau}^{\text{ch}} = \underline{\lambda}_{e,\tau}^{\text{dis}} = 0$. We also determine that $\overline{\lambda}_{e,\tau}^{\text{ch}} \geq 0$ and $\overline{\lambda}_{e,\tau}^{\text{dis}} \geq 0$ by the dual feasibility property and the assumption that $0 < \tilde{P}_{e,\tau}^{\text{ch}} \leq \overline{P}_e^{\text{ch}}$ and $0 < \tilde{P}_{e,\tau}^{\text{dis}} \leq \overline{P}_e^{\text{dis}}$. Then (5.14c)-(5.14d) become:

$$\alpha_e + \overline{\lambda}_{e,\tau}^{\text{ch}} + \eta_e^{\text{ch}} \Delta t \sum_{n=\tau}^{H} (\overline{\lambda}_{e,n}^{\text{soc}} - \underline{\lambda}_{e,n}^{\text{soc}}) + \mu_\tau^{\text{pb}} = 0, \tag{5.20}$$

$$\beta_e + \overline{\lambda}_{e,\tau}^{\text{dis}} + \tfrac{1}{\eta_e^{\text{dis}}} \Delta t \sum_{n=\tau}^{H} (\underline{\lambda}_{e,n}^{\text{soc}} - \overline{\lambda}_{e,n}^{\text{soc}}) - \mu_\tau^{\text{pb}} = 0. \tag{5.21}$$

Solving for $\mathcal{I} = \sum_{n=\tau}^{H} (\overline{\lambda}_n^{\text{soc}} - \underline{\lambda}_n^{\text{soc}})$ in (5.20), and then replacing $-\mathcal{I}$ in (5.21), we get:

$$\beta_e + \tfrac{1}{\eta_e^{\text{dis}} \eta_e^{\text{ch}}} \alpha_e + \overline{\lambda}_{e,\tau}^{\text{dis}} + \tfrac{1}{\eta_e^{\text{dis}} \eta_e^{\text{ch}}} \overline{\lambda}_{e,\tau}^{\text{ch}} + (\tfrac{1}{\eta_e^{\text{dis}} \eta_e^{\text{ch}}} - 1) \mu_\tau^{\text{pb}} = 0. \tag{5.22}$$

By the assumption that $\alpha_e, \beta_e \geq 0$, $(\alpha_e + \beta_e) > 0$, and $0 < \eta_e^{\text{ch}}, \eta_e^{\text{dis}} < 1$, the sum of the first two terms in (5.22) is positive. Then by dual feasibility, both the third and fourth terms in (5.22) are non-negative. With the assumption that $\mu_\tau^{\text{pb}} \geq 0$, we obtain a contradiction since the left hand side of (5.22) cannot equal zero. Therefore, if $\mu_\tau^{\text{pb}} \geq 0$, then an optimal solution to the convex EMS

models in NM-all, FiT-all, and S2-all will obey (5.2) at some time $\tau \in \mathcal{T}$ for ESS e. □

5.2.2.1 Theoretical Analysis for EMS-to-Grid Scenario 1

In this section, we provide our theoretical result for EMS models for EMS-to-grid Scenario 1, i.e., (5.4), (5.6), as well as their possible demand charge and flexible demand modifications.

Proposition 5.1 Assume $\alpha_e, \beta_e \geq 0$, $(\alpha_e + \beta_e) > 0$, and $0 < \eta_e^{\text{ch}}, \eta_e^{\text{dis}} < 1$ for some ESS $e \in \mathcal{E}$. Further assume that $c_t^{\text{d}} \geq 0$ for the net metering cases (NM-all), and $c_t^{\text{d}} > c_t^{\text{e}} \geq 0$ for the FiT cases (FiT-all) for all $t \in \mathcal{T}$. Then, an optimal solution to any of the EMS models in NM-all and FiT-all will satisfy (5.2) for such as ESS e and for all $t \in \mathcal{T}$. Additionally, an optimal solution to any of the EMS models in FiT-all will satisfy (5.7) for all time $t \in \mathcal{T}$.

Proof. Assume $\alpha_e, \beta_e \geq 0$, $(\alpha_e + \beta_e) > 0$, and $0 < \eta_e^{\text{ch}}, \eta_e^{\text{dis}} < 1$ for some ESS $e \in \mathcal{E}$. Further assume that $c_t^{\text{d}} \geq 0$ for the net metering cases (NM-all), and $c_t^{\text{d}} > c_t^{\text{e}} \geq 0$ for the FiT cases (FiT-all) for all $t \in \mathcal{T}$.

We begin by showing that the optimal solution to any model in NM-all and FiT-all will satisfy the ESS charging and discharging complementarity constraint in (5.2), without explicitly including it in the optimization model. First, we will consider the NM-all models. For NM-G and NM-F, by (5.14a) we have $\mu_t^{\text{pb}} = c_t^{\text{d}} \geq 0$ (since we assume $c_t^{\text{d}} \geq 0$ for all $t \in \mathcal{T}$). Thus, by Lemma 5.1, we know that an optimal solution to NM-G and NM-F will satisfy (5.2) since $\mu_t^{\text{pb}} \geq 0$ for all time $t \in \mathcal{T}$. For NM-D and NM-D-F, by (5.15a) we have $\mu_t^{\text{pb}} = c_t^{\text{d}} + \lambda_t^{\text{dc2}} \geq 0$ since $c_t^{\text{d}} \geq 0$ by our assumption and $\lambda_t^{\text{dc2}} \geq 0$ by dual feasibility. Then, by Lemma 5.1, we know that an optimal solution to NM-D and NM-D-F will satisfy (5.2) since $\mu_t^{\text{pb}} \geq 0$ for all time $t \in \mathcal{T}$ for ESS e.

For the FiT-all models, again by (5.18b), we have $\mu_t^{\text{pb}} = c_t^{\text{e}} + \underline{\lambda}_t^{\text{exp}} \geq 0$ since $c_t^{\text{e}} \geq 0$ by our assumption and $\underline{\lambda}_t^{\text{exp}} \geq 0$ by dual feasibility. Then, by Lemma 5.1, an optimal solution to the EMS models in FiT-all will satisfy (5.2) for ESS e and all $t \in \mathcal{T}$.

Lastly, we show that an optimal solution to the EMS models in FiT-all satisfies (5.7). We

prove this by contradiction, so assume that at some time $\tau \in \mathcal{T}$, the optimal solution to an FiT-all model is such that (5.7) is not satisfied, i.e., $\tilde{P}_\tau^{\text{grid}} > 0$ and $\tilde{P}_\tau^{\text{exp}} > 0$. By the complementary slackness condition at time τ, we obtain $\underline{\lambda}_\tau^{\text{exp}} = \underline{\lambda}_\tau^{\text{grid}} = 0$. For FiT-G and FiT-F, the stationarity constraints in (5.18a)-(5.18b) become:

$$c_\tau^{\text{d}} - \mu_\tau^{\text{pb}} = 0,$$

$$-c_\tau^{\text{e}} + \mu_\tau^{\text{pb}} = 0,$$

implying $\mu_\tau^{\text{pb}} = c_\tau^{\text{d}} = c_\tau^{\text{e}}$, which results in a contradiction due to our assumption that $0 \leq c_t^{\text{e}} < c_t^{\text{d}}$ for all $t \in \mathcal{T}$. Thus, an optimal solution to FiT-G and FiT-D must satisfy (5.7) for all $t \in \mathcal{T}$. Similarly, for FiT-D and FiT-D-F, the stationarity constraints in (5.18b) and (5.19a) become:

$$c_\tau^{\text{d}} + \lambda_\tau^{\text{dc2}} - \mu_\tau^{\text{pb}} = 0,$$

$$-c_\tau^{\text{e}} + \mu_\tau^{\text{pb}} = 0,$$

which imply that $c_\tau^{\text{e}} = c_\tau^{\text{d}} + \lambda_\tau^{\text{dc2}}$, which results in a contradiction since $c_\tau^{\text{d}} + \lambda_\tau^{\text{dc2}} > c_\tau^{\text{e}}$ by our FiT rate assumptions and $\lambda_\tau^{\text{dc2}} \geq 0$ by dual feasibility. Thus, the optimal solution to any convex model in FiT-all will satisfy (5.7) for ESS e for all $t \in \mathcal{T}$. □

Notice that the statement of Proposition 5.1 does not depend on prior knowledge of the optimal solutions to the EMS models. This distinguishes the strength of the Proposition 5.1 statement from that of Proposition 5.2 for EMS-to-grid Scenario 2, as well as previous works in this space [20, 89, 91–95].

5.2.2.2 Theoretical Analysis for EMS-to-Grid Scenario 2

In this section, we provide our theoretical result for EMS models for EMS-to-grid Scenario 2, i.e., (5.8) and the possible demand charge and flexible demand modifications.

Proposition 5.2 Assume $\alpha_e, \beta_e \geq 0$, $(\alpha_e + \beta_e) > 0$, and $0 < \eta_e^{\text{ch}}, \eta_e^{\text{dis}} < 1$ for some ESS $e \in \mathcal{E}$. Further assume that $c_t^{\text{d}} \geq 0$ at time $t \in \mathcal{T}$. If at least one of the following conditions hold:

C1) $0 < \tilde{P}_t^{\text{grid}}$ at time $t \in \mathcal{T}$,

C2) $0 \leq \tilde{P}_t^{\mathrm{c}} < P_t^{\mathrm{res}}$ at time $t \in \mathcal{T}$,

C3) $\sum_{n=t}^{H}(\overline{\lambda}_{e,n}^{\mathrm{soc}} - \underline{\lambda}_{e,n}^{\mathrm{soc}}) \leq 0$ at time $t \in \mathcal{T}$,

then an optimal solution to any of the EMS models in S2-all will satisfy (5.2) for ESS $e \in \mathcal{E}$ and time t.

Proof. Assume $\alpha_e, \beta_e \geq 0$, $(\alpha_e + \beta_e) > 0$, and $0 < \eta_e^{\mathrm{ch}}, \eta_e^{\mathrm{dis}} < 1$ for some ESS $e \in \mathcal{E}$. Also assume that $c_t^{\mathrm{d}} \geq 0$ at time $t \in \mathcal{T}$.

For each of the three conditions given in Proposition 5.2, we will show that an optimal solution will satisfy (5.2). We begin by assuming that Condition C1 is true, i.e., the optimal solution to a model in S2-all is such that $\tilde{P}_t^{\mathrm{grid}} > 0$ for time $t \in \mathcal{T}$. Then, with the complementary slackness condition, we obtain $\underline{\lambda}_t^{\mathrm{grid}} = 0$. For S2-G and S2-F, by the stationarity condition in (5.18a) we have $\mu_t^{\mathrm{pb}} = c_t^{\mathrm{d}} \geq 0$ by our assumption that $c_t^{\mathrm{d}} \geq 0$. Then, by Lemma 5.1, the optimal solution to S2-G and S2-F will satisfy (5.2) for ESS e if $\tilde{P}_t^{\mathrm{grid}} > 0$. For S2-D and S2-D-F, by the stationarity condition in (5.19a) we have $\mu_t^{\mathrm{pb}} = c_t^{\mathrm{d}} + \lambda_t^{\mathrm{dc2}} \geq 0$ by our assumption that $c_t^{\mathrm{d}} \geq 0$ and $\lambda_t^{\mathrm{dc2}} \geq 0$ by dual feasibility. Then, by Lemma 5.1, the optimal solution to S2-D and S2-D-F will satisfy (5.2) for ESS e if $\tilde{P}_t^{\mathrm{grid}} > 0$. Thus, if the optimal solution to a model in S2-all is such that $\tilde{P}_t^{\mathrm{grid}} > 0$ for time $t \in \mathcal{T}$, the optimal solution will satisfy (5.2) for ESS e.

Next, assume that Condition C2 is true, i.e., the optimal solution to a model in S2-all is such that $0 \leq \tilde{P}_t^{\mathrm{c}} < P_t^{\mathrm{res}}$ for time $t \in \mathcal{T}$. By the complementary slackness condition, we obtain $\overline{\lambda}_t^{\mathrm{res}} = 0$. Then, for each model in S2-all, by (5.14b) we have $\mu_t^{\mathrm{pb}} = \underline{\lambda}_t^{\mathrm{res}} \geq 0$ because of dual feasibility. Therefore, by Lemma 5.1, the EMS models in S2-all will satisfy (5.2).

Lastly, we consider Condition C3. Assume that Condition C3 is true at time $t \in \mathcal{T}$, i.e., $\sum_{n=t}^{H}(\overline{\lambda}_{e,n}^{\mathrm{soc}} - \underline{\lambda}_{e,n}^{\mathrm{soc}}) \leq 0$ at time $t \in \mathcal{T}$. Assume that the optimal solution to any of the EMS models in S2-all is such that the constraint in (5.2) is *not* satisfied at time $t \in \mathcal{T}$ and ESS $e \in \mathcal{E}$, i.e. $0 < \tilde{P}_{e,t}^{\mathrm{ch}} \leq \overline{P}_e^{\mathrm{ch}}$ and $0 < \tilde{P}_{e,t}^{\mathrm{dis}} \leq \overline{P}_e^{\mathrm{dis}}$. By the complementary slackness conditions at time t, we obtain that $\underline{\lambda}_{e,t}^{\mathrm{ch}} = \underline{\lambda}_{e,t}^{\mathrm{dis}} = 0$. We also determine that $\overline{\lambda}_{e,t}^{\mathrm{ch}} \geq 0$ and $\overline{\lambda}_{e,t}^{\mathrm{dis}} \geq 0$ by the dual feasibility property and the assumption that $0 < \tilde{P}_{e,t}^{\mathrm{ch}} \leq \overline{P}_e^{\mathrm{ch}}$ and $0 < \tilde{P}_{e,t}^{\mathrm{dis}} \leq \overline{P}_e^{\mathrm{dis}}$. Then (5.14c)-(5.14d)

become (5.20)-(5.21). Adding (5.20) and (5.21) together, we obtain:

$$\alpha_e + \beta_e + \overline{\lambda}^{\text{ch}}_{e,t} + \overline{\lambda}^{\text{dis}}_{e,t} + \Delta t(\eta^{\text{ch}}_e - \tfrac{1}{\eta^{\text{dis}}_e}) \sum_{n=t}^{H} (\overline{\lambda}^{\text{soc}}_{e,n} - \underline{\lambda}^{\text{soc}}_{e,n}) = 0. \tag{5.23}$$

By the assumption that $\alpha_e, \beta_e \geq 0$, $(\alpha_e + \beta_e) > 0$, and $0 < \eta^{\text{ch}}_e, \eta^{\text{dis}}_e < 1$, together with dual feasibility, the sum of the first four terms in (5.23) is positive. Since $(\eta^{\text{ch}}_e - \frac{1}{\eta^{\text{dis}}_e}) < 0$ and our assumption that $\sum_{n=t}^{H} (\overline{\lambda}^{\text{soc}}_{e,n} - \underline{\lambda}^{\text{soc}}_{e,n}) \leq 0$, we obtain a contradiction since the left hand side of (5.23) cannot equal zero. Thus, if Condition C3 is satisfied, an optimal solution to any of the models in S2-all will satisfy (5.2) at time $t \in \mathcal{T}$ for ESS e. □

5.2.2.3 Applying Our Theoretical Results in Practice

Lastly, we discuss cases when the penalty approach for guaranteeing proper ESS model behavior is not necessary. For each EMS optimization model, we summarize our results for various electricity prices and under the presence or absence of our proposed penalty approach in Table 5.2. Notice in Table 5.2, it is possible to ensure physically possible ESS optimal control strategies without the penalty approach as long as the electricity price is strictly positive for all time $t \in \mathcal{T}$. In the case that an energy utility charges $c^t_e = \$0/\text{kWh}$ for some time $t \in \mathcal{T}$ to flatten grid power demand over time [98], our results guaranteeing proper ESS model behavior will hold as long as the penalty approach is adopted where we require $\alpha_e, \beta_e \geq 0$ such that $(\alpha_e + \beta_e) > 0$. Importantly, Table 5.2 also highlights situations where simultaneous ESS charging and discharging will happen if our proposed penalty approach is not used.

5.2.3 Numerical Results: Case Study with Various EMS Models

Case studies that capture the behavior each proposed relaxed convex EMS model are provided to highlight our theoretical results. We also show a case study to demonstrate physically unrealizable ESS behavior (simultaneous charging and discharging EMS solution) when the linear penalty approach is not used. The EMS models are simulated for 24 hours with 1 hour time

Table 5.2: Summary of results. Assume $\alpha_e \geq 0$ and $\beta_e \geq 0$ for some $e \in \mathcal{E}$.

EMS-to-Grid Scenario	Penalty Sum	Electricity Cost	Guaranteed Proper ESS Model Behavior?
Scenario 1: Net Metering	$0 < (\alpha_e + \beta_e)$	$0 \leq c_t^{\mathrm{d}}\ \forall t \in \mathcal{T}$	Yes
	$0 = (\alpha_e + \beta_e)$	$c_t^{\mathrm{d}} = 0$ for some $t \in \mathcal{T}$	No
	$0 = (\alpha_e + \beta_e)$	$0 < c_t^{\mathrm{d}},\ \forall t \in \mathcal{T}$	Yes
Scenario 1: FiT	$0 < (\alpha_e + \beta_e)$	$0 < c_t^{\mathrm{e}} < c_t^{\mathrm{d}}$ $\forall t \in \mathcal{T}$	Yes
	$0 = (\alpha_e + \beta_e)$	$0 = c_t^{\mathrm{e}} < c_t^{\mathrm{d}}$ for some $t \in \mathcal{T}$	Yes
Scenario 2	$0 < (\alpha_e + \beta_e)$	$0 \leq c_t^{\mathrm{d}}\ \forall t \in \mathcal{T}$	Yes
	$0 = (\alpha_e + \beta_e)$	$c_t^{\mathrm{d}} = 0$ for some $t \in \mathcal{T}$	No

Table 5.3: ESS parameters for EMS case studies. The symbol '–' indicates a penalty parameter that is not applicable to the case study.

ESS e	Efficiency η_e^{ch} $(= \eta_e^{\mathrm{dis}})$	Penalty Parameter α_e		
		NM	FiT	Scenario 2
1	0.97	0.010	0.010	0.010
2	0.95	0.010	0.010	0.000
3	0.93	0.015	–	–

steps in Python using CVXPY [99, 100]. The electricity demand data and weather data (for PV generation) are from different days in the RBSA dataset [69], and are increased for this study to capture futuristic situations with high renewable energy generation. The ESS parameters used in the EMS case studies are given in Table 5.3, where each ESS is assumed to have a capacity $\overline{E}_e$ of 5 kWh, maximum charging and discharging power $\overline{P}_e^{\mathrm{ch}} = \overline{P}_e^{\mathrm{dis}} = 3$kW, initial ESS state of charge 2.5 kWh, and discharging penalty $\beta_e = 0$ for each ESS $e = \{1, 2, 3\}$. The shiftable proportion of the flexible load γ_t and the load shedding inconvenience parameter ρ_t are given in Fig. 5.1.

For showing that the complementarity constraints in (5.2) and (5.7) are satisfied, we define the

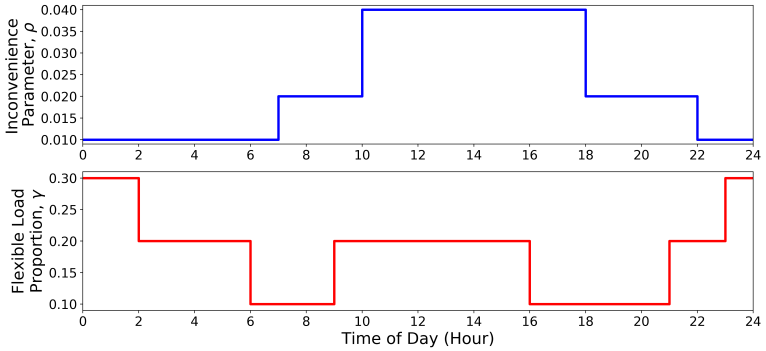

Figure 5.1: Parameter values for ρ_t and γ_t for EMS case studies.

Table 5.4: TOU electricity prices for case studies.

Time of Day	Period	Electricity Price c_t^{d} (\$/kWh)	
		Case 1	Case 2
9PM-9AM	Off-Peak	0.08	0.00
9AM-2PM 6PM-9PM	Shoulder	0.13	0.10
2PM-6PM	On-Peak	0.18	0.15

numerical complementarity gap:

$$\text{Complementarity Gap for ESS } e \text{ at time } t = P_{e,t}^{\mathrm{ch}} \cdot P_{e,t}^{\mathrm{dis}},$$

$$\text{Complementarity Gap for FiT at time } t = P_t^{\mathrm{grid}} \cdot P_t^{\mathrm{exp}},$$

which should be numerically close to zero in our case studies.

First, we consider a case study for NM-G, where the EMS is coordinating three ESSs, PV generation, and buying and selling power to the grid to satisfy the electricity demand and minimize the electricity cost under net metering. In this case study, the TOU pricing (Case 2) schedule in Table 5.4 is used, which captures the case where the cost of electricity is \$0.0/kWh for some time $t \in \mathcal{T}$. The results of this case study are shown in Fig. 5.2. The power profiles shown in Fig. 5.2 (top) demonstrate that the ESSs are charging when the electricity is \$0.0/kWh and discharge when the electricity is most expensive during the peak TOU pricing period. Fig. 5.2 (bottom) shows the penalty approach ensures the complementarity constraint (5.2) is satisfied, even when the price of electricity is \$0.0/kWh, as described in Proposition 5.1.

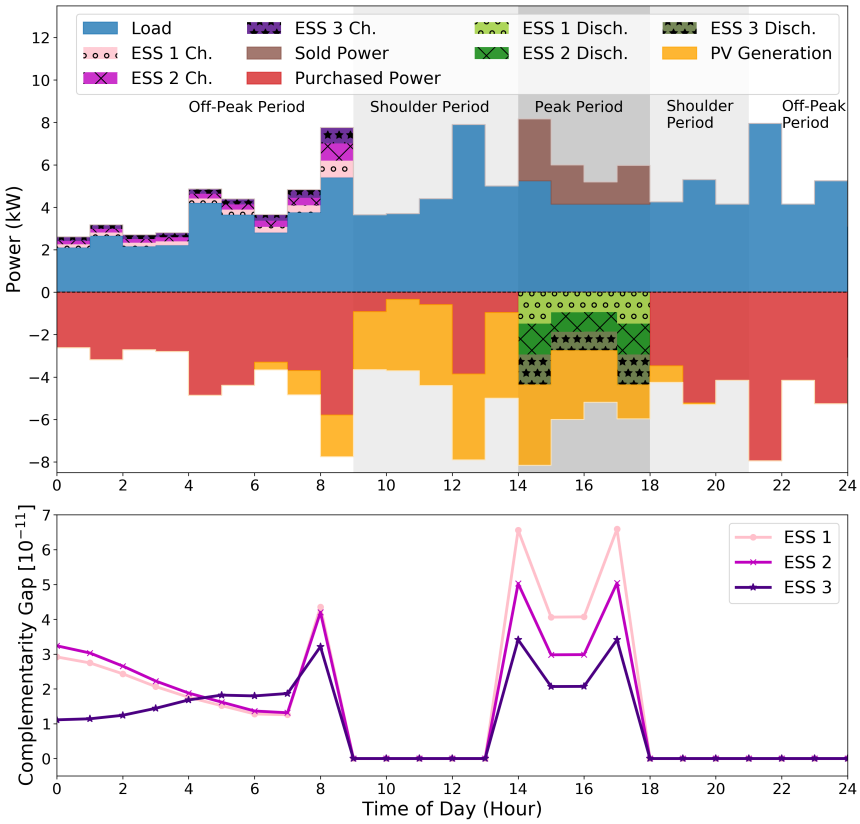

Figure 5.2: Case study results for the NM-G model with TOU pricing Case 2 in Table 5.4. Top: Power balance showing optimal EMS resource coordination. Bottom: Numerical complementarity gap for each ESS.

Next, we consider a second case study for FiT-F, where the EMS is coordinating two ESSs, PV generation, flexible load scheduling, and buying and selling power to the grid in order to minimize the overall cost of electricity under FiT electricity pricing, where c_t^{e} =\$0.08/kWh and c_t^{d} =\$0.11/kWh for all $t \in \mathcal{T}$. The results of this case study are shown in Fig. 5.3. In Fig. 5.3 (top), the power profiles show that excess PV generation (after the load is met) is either sold back to the grid or used to charge the ESS. Otherwise, the EMS is using power drawn from the grid and the ESS to satisfy the load. The forecasted load profile is depicted with the black dash-dotted line to illustrate the load shifting results. In Fig. 5.3 (bottom), the complementarity gap for both the ESS and FiT model are shown to highlight that the complementarity constraints in (5.2) and (5.7) are numerically satisfied without explicitly including these constraints in the optimization problem, as proven in Proposition 5.1.

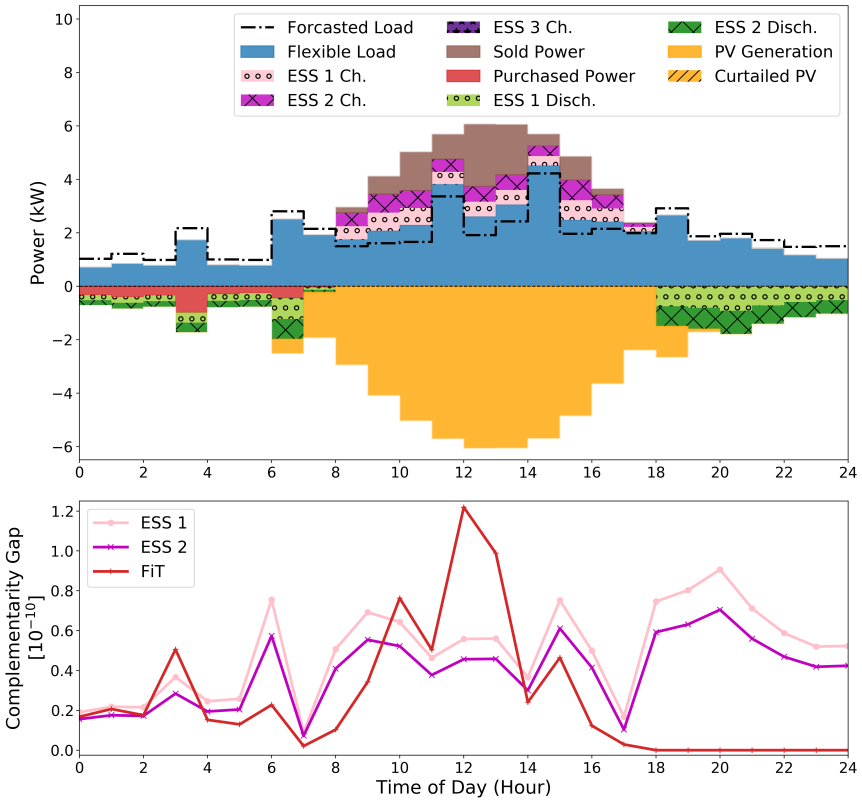

Figure 5.3: Case study for the FiT-F model where c_t^{e} =\$0.08/kWh and c_t^{d} =\$0.11/kWh for all $t \in \mathcal{T}$. Top: Power balance showing optimal EMS resource coordination. Bottom: Numerical complementarity gap for both ESS 1 and 2 operation and FiT pricing variables.

Lastly, we consider a case study for S2-D-F, where the EMS is coordinating 2 ESSs, PV generation, flexible load scheduling, and buying power from the grid in order to meet the electricity demand and minimize the overall cost of electricity under demand charges and a TOU pricing (Case 1) schedule in Table 5.4. In this case study, ESS 1 is incorporated into the EMS using the proposed penalty approach, while ESS 2 does not use the penalty approach ($\alpha_2 = 0$), as seen in Table 5.3 (Scenario 2). The results of this case study are shown in Fig. 5.4, where the top plot shows the EMS draws power from the grid and the ESSs to satisfy the demand when there is no PV generation. When the PV generation exceeds the load and the ESS capacity, we see that without the penalty approach, ESS 2 simultaneously charges and discharges in order to waste energy since excess power cannot be exported to the grid. When the penalty approach is used, the excess PV generation is curtailed properly, instead of using the ESS charging and discharging losses

to "curtail" power. The complementarity gap for ESS 1 and 2, Fig. 5.4 (middle) and (bottom), respectively, demonstrate that ESS 1 satisfies (5.2) ensuring proper ESS model behavior when the penalty approach is used and ESS 2 does not satisfy (5.2) since the penalty approach was not adopted in the EMS formulation, as expected from our results in Proposition 5.2.

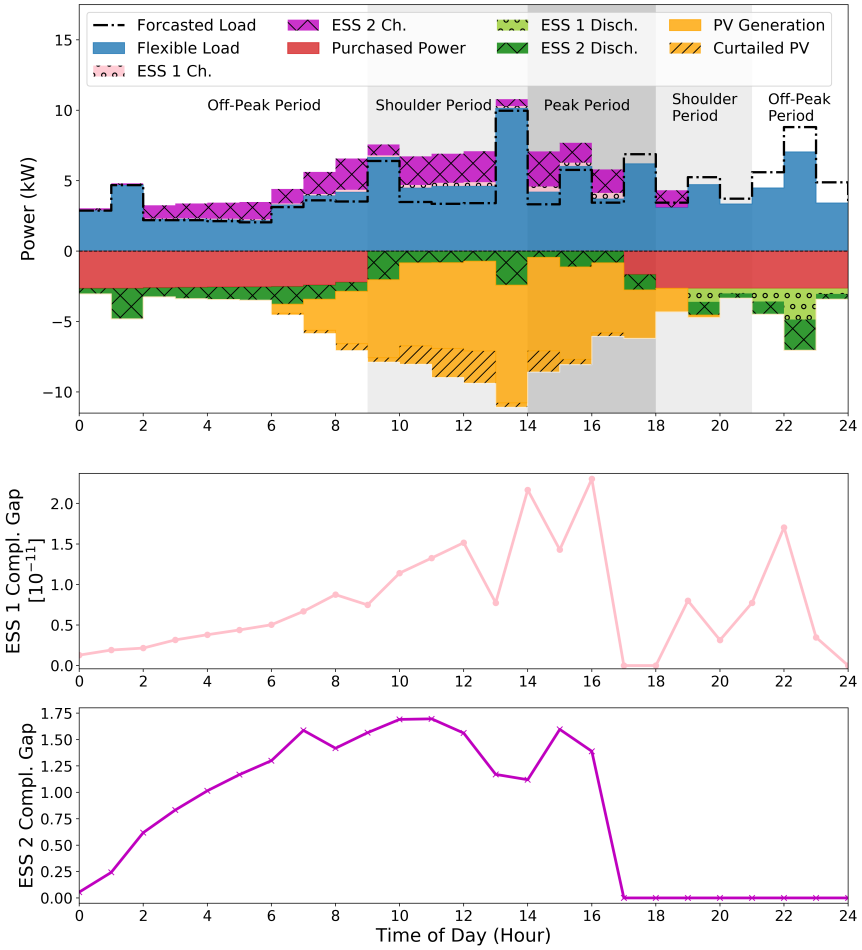

Figure 5.4: Case study results for S2-D-F with TOU electricity pricing schedule in Table 5.4 (Case 1) where penalty approach is not adopted for all ESSs in the EMS formulation. Top: Power balance demonstrating the optimal EMS control strategy. Middle: Numerical complementarity gap for ESS 1. Bottom: Numerical complementarity gap for ESS 2.

5.3 Grid-Connected Energy Storage System Models with Complementarity Constraints in DC OPF

In this section, an exact penalty reformulation approach is presented in order to omit the non-convex complementarity constraints in an ESS model for use in a general DC OPF problem

in a transmission setting. The reformulation consists of modifying the cost function to include a penalty function with an associated penalty parameter with the complementarity constraint omitted. The KKT conditions are used to show that solutions to the convex relaxed problem satisfy the complementarity constraints without explicitly including them in the optimization model. The DC OPF setting has increased complexity compared to the EMS setting described above in Section 5.2 due to the introduction of power flows in the network, adoption of a general optimization objective function, and the consideration of various possible resources (multiple generators, renewable sources, and/or ESSs) at each bus. Next, the DC OPF optimization model with a relaxed convex grid-connected ESS model is introduced. Then, the theoretical analysis for guaranteeing a solution with non-simultaneous charging and discharging presented. Lastly, extensive simulation results for various IEEE test systems are provided to demonstrate the sensitivity of the optimal solution to the penalty reformulation approach and the computational savings with the proposed convex ESS model versus the non-convex ESS model. The relevant notation for this section is given in Table 5.5.

5.3.1 DC OPF Formulation with Renewables and Grid-Connected Energy Storage Systems

Next, we provide the mathematical formulation for the DC OPF problem and the conditions that guarantee non-simultaneous charging and discharging behavior in a linear ESS model. We consider a DC OPF problem that optimally coordinates dispatchable and non-dispatchable power sources and energy storage systems to satisfy some load to minimize generation costs in a transmission network given line capacity limits under the assumptions line conductances are negligible, voltage magnitudes are all 1.0 p.u., and voltage angle differences are sufficiently small. In this work, we assume the network consists of dispatchable power sources $g \in \mathcal{G}$ (i.e., coal, gas, nuclear, hydro), non-dispatchable power sources $r \in \mathcal{R}$ (i.e., wind, solar), and energy storage systems $e \in \mathcal{E}$ to satisfy the total network load.

The control variables at each time $t \in \mathcal{T}$ are collected in the vector $\underline{\mathbf{x}}_H = \begin{bmatrix}\mathbf{x}_1 & \mathbf{x}_2 \cdots \mathbf{x}_H\end{bmatrix}^T$

Table 5.5: Notation for DC OPF with ESSs and renewable energy sources.

	Sets
$r \in \mathcal{R}$	Set of non-dispatchable sources (renewable)
$e \in \mathcal{E}$	Set of energy storage systems
$b \in \mathcal{B}$	Set of buses in the network
$g \in \mathcal{G}$	Set of dispatchable sources (thermal, hydro)
$t \in \mathcal{T}$	Hourly time steps: $1, \ldots, H$
$d \in \mathcal{B}_b$	Set of buses connected to bus b
$bd \in \mathcal{L}$	Set of lines in network
$\mathcal{G}_b$	Set of dispatchable power sources at bus b
$\mathcal{R}_b$	Set of non-dispatchable power sources at bus b
$\mathcal{E}_b$	Set of energy storage systems at bus b
	Decision Variables
$E_{e,t}$	State of charge of ESS e (MWh)
$P^{\text{ch}}_{e,t}$	Power injected into ESS e (MW)
$P^{\text{dis}}_{e,t}$	Power drawn from ESS e (MW)
$P^{\text{G}}_{g,t}$	Power generated from the dispatchable source g (MW)
$P^{\text{c}}_{r,t}$	Curtailed power of non-dispatchable source r (MW)
$\theta_{b,t}$	Voltage angle at bus b

	Parameters
H	Prediction horizon
B_{bd}	Susceptence of line connecting bus b and d
$\underline{E}^{\text{init}}_e$	Initial state of charge of ESS e (MWh)
$\overline{E}_e$	Maximum energy storage in ESS e (MWh)
$\underline{E}_e$	Minimum energy storage in ESS e (MWh)
η^{ch}_e	Charging efficiency of ESS e
η^{dis}_e	Discharging efficiency of ESS e
f_{bd}	Capacity of line connecting bus b and d
$\overline{P}_e$	Maximum charging/discharging power of ESS e (MW)
$\underline{P}^{\text{G}}_g$	Minimum real power dispatch of source g (MW)
$\overline{P}^{\text{G}}_g$	Maximum real power dispatch of source g (MW)
$P^{\text{res}}_{r,t}$	Available power from non-dispatchable source r (MW)
$P^{\text{L}}_{b,t}$	Active power demand at bus b (MW)

where $\mathbf{x}_t = [\{P^{\text{G}}_{g,t}\}_{g\in\mathcal{G}}, \{P^{\text{ch}}_{e,t},\ P^{\text{dis}}_{e,t}\}_{e\in\mathcal{E}}, \{P^{\text{c}}_{r,t}\}_{r\in\mathcal{R}}, \{\theta_{b,t}\}_{b\in\mathcal{B}}]^T$. Then, the overall objective function $f_{\text{tot}}(\underline{\mathbf{x}}_H)$ is:

$$f_{\text{tot}}(\underline{\mathbf{x}}_H) = \sum_{t=1}^{H} \left(f_{\text{cost}}(\mathbf{P}^{\text{G}}) + \rho f_{\text{pen}}(\mathbf{P}^{\text{ch}}, \mathbf{P}^{\text{dis}}) \right), \tag{5.24}$$

where $\rho > 0$ is the penalty parameter, $\mathbf{P}^{\text{G}}$ is a vector collecting $P^{\text{G}}_{g,t}$ for all $g \in \mathcal{G}$ and $t \in \{1, \ldots, H\}$, and $\mathbf{P}^{\text{ch}}$ and $\mathbf{P}^{\text{dis}}$ are vectors collecting $P^{\text{ch}}_{e,t}$ and $P^{\text{dis}}_{e,t}$, respectively, for all $e \in \mathcal{E}$ and $t \in \{1, \ldots, H\}$. To enforce the complementarity constraint, we include a penalty function $f_{\text{pen}}(\mathbf{P}^{\text{ch}}, \mathbf{P}^{\text{dis}})$ [24, 25]. We assume $f_{\text{tot}}(\underline{\mathbf{x}}_H)$ is a differentiable, non-decreasing, positive-valued, convex function, which captures the characteristics of common objective functions used in solving the DC OPF problem such as generation costs and future ESS replacement costs [90]. Let $\partial_{x_t} f_{\text{tot}}(\tilde{\underline{\mathbf{x}}}_H)$ denote the partial derivative of $f_{\text{tot}}(\underline{\mathbf{x}}_H)$ with respect to the control variable x_t evaluated at $\tilde{\underline{\mathbf{x}}}_H$. Note that the conditions on (5.24) imply that $\partial_{P^{\text{G}}_{g,t}} f_{\text{tot}}(\tilde{\underline{\mathbf{x}}}_H), \partial_{P^{\text{ch}}_{e,t}} f_{\text{tot}}(\tilde{\underline{\mathbf{x}}}_H), \partial_{P^{\text{dis}}_{e,t}} f_{\text{tot}}(\tilde{\underline{\mathbf{x}}}_H) \geq 0$ for all $g \in \mathcal{G}, e \in \mathcal{E}$ and $\partial_{P^{\text{c}}_{r,t}} f_{\text{tot}}(\tilde{\underline{\mathbf{x}}}_H) = 0$ for all $r \in \mathcal{R}$ and $t \in \{1, \ldots, H\}$. The overall relaxed convex MPC-based DC

OPF problem with ESSs and the objective function in (5.24) is:

$$\min_{\underline{\mathbf{x}}_H} f_{\text{tot}}(\underline{\mathbf{x}}_H) \tag{5.25a}$$

$$\text{s.t. } \underline{P}_g^{\text{G}} \leq P_{g,t}^{\text{G}} \leq \overline{P}_g^{\text{G}}, \qquad \forall g \in \mathcal{G}, \forall t \in \mathcal{T}, \tag{5.25b}$$

$$0 \leq P_{r,t}^{\text{c}} \leq P_{r,t}^{\text{res}}, \qquad \forall r \in \mathcal{R}, \forall t \in \mathcal{T}, \tag{5.25c}$$

$$0 \leq P_{e,t}^{\text{ch}} \leq \overline{P}_e, \qquad \forall e \in \mathcal{E}, \forall t \in \mathcal{T}, \tag{5.25d}$$

$$0 \leq P_{e,t}^{\text{dis}} \leq \overline{P}_e, \qquad \forall e \in \mathcal{E}, \forall t \in \mathcal{T}, \tag{5.25e}$$

$$\underline{E}_e \leq E_{e,t+1} \leq \overline{E}_e, \qquad \forall e \in \mathcal{E}, \forall t \in \mathcal{T}, \tag{5.25f}$$

$$E_{e,t+1} = E_{e,t} + \eta_e^{\text{ch}} \Delta t P_{e,t}^{\text{ch}} - \frac{1}{\eta_e^{\text{dis}}} \Delta t P_{e,t}^{\text{dis}}, \qquad \forall e \in \mathcal{E}, \forall t \in \mathcal{T}, \tag{5.25g}$$

$$-f_{bd} \leq B_{bd}(\theta_{b,t} - \theta_{d,t}) \leq f_{bd}, \qquad \forall d \in \mathcal{B}_b, \forall t \in \mathcal{T}, \tag{5.25h}$$

$$0 = \sum_{e \in \mathcal{E}_b} (P_{e,t}^{\text{ch}} - P_{e,t}^{\text{dis}}) - \sum_{r \in \mathcal{R}_b} (P_{r,t}^{\text{res}} - P_{r,t}^{\text{c}}) + P_{b,t}^{\text{L}} - \sum_{g \in \mathcal{G}_b} P_{g,t}^{\text{G}} + \sum_{d \in \mathcal{B}_b} B_{bd}(\theta_{b,t} - \theta_{d,t}), \qquad \forall b \in \mathcal{B}, \forall t \in \mathcal{T}. \tag{5.25i}$$

The constraint in (5.25b) provides the upper and lower limits on power generation for dispatchable power sources $g \in \mathcal{G}$. In (5.25c), the curtailed power $P_{r,t}^{\text{c}}$ is limited by the available non-dispatchable power $P_{r,t}^{\text{res}}$ for each non-dispatchable power source $r \in \mathcal{R}$. Thus, the supplied non-dispatchable power is given by $(P_{r,t}^{\text{res}} - P_{r,t}^{\text{c}})$ for all $r \in \mathcal{R}$ and $t \in \mathcal{T}$. The constraint in (5.25h) enforces the capacity limits of the line from bus b to bus d, where B_{bd} is the susceptence of the line and f_{bd} is the maximum capacity of line. The power balance constraint at each bus b is given in (5.25i).

The MPC-based DC OPF problem given in (5.25) will be the basis of the analysis presented in Section 5.3.2.2 for the proposed linear ESS model. We use the KKT conditions to determine conditions, together with assumptions on the choice of $f_{\text{cost}}(\mathbf{P}^{\text{G}})$ and $f_{\text{pen}}(\mathbf{P}^{\text{ch}}, \mathbf{P}^{\text{dis}})$, that the DC OPF problem must satisfy such that the optimal solution to $(\mathcal{P}_1)$ does not result in simultaneous charging and discharging, i.e., the complementarity constraints in (5.2) are satisfied.

5.3.2 Theoretical Guarantees for Relaxed Energy Storage System Models in DC OPF

First, we derive the KKT conditions for the optimization problem given in (5.25). The KKT conditions will be used in the proof of Proposition 5.3 where we prove that simultaneous charging and discharging, i.e., $0 < P^{\text{ch}}_{e,t}, P^{\text{dis}}_{e,t} \leq \overline{P}_e$ for any $e \in \mathcal{E}$ and for any time $t \in \mathcal{T}$, in the ESS model in (5.1) is suboptimal in the DC OPF problem given certain conditions are satisfied. To maintain notational consistency with our published results in [20], for the remainder of our discussion in Section 5.3, let $\eta^{\text{d}}_e = \frac{1}{\eta^{\text{dis}}_e}$ for all $e \in \mathcal{E}$.

5.3.2.1 Derivation of the KKT Conditions for the DC OPF Problem

To aid in the presentation of the KKT conditions, we introduce additional notation for describing the inequality and equality constraints in the optimization problem given in (5.25). Writing (5.25) in standard form [22], we denote the functions on the left-hand side of the inequality constraints in (5.25) by:

$$\underline{f}^{\text{gen}}_{g,t}(\underline{\mathbf{x}}_H) = \underline{P}^{\text{G}}_g - P^{\text{G}}_{g,t}, \qquad \forall g \in \mathcal{G}, \forall t \in \mathcal{T}, \tag{5.26a}$$

$$\overline{f}^{\text{gen}}_{g,t}(\underline{\mathbf{x}}_H) = P^{\text{G}}_{g,t} - \overline{P}^{\text{G}}_g, \qquad \forall g \in \mathcal{G}, \forall t \in \mathcal{T}, \tag{5.26b}$$

$$\underline{f}^{\text{res}}_{r,t}(\underline{\mathbf{x}}_H) = -P^{\text{c}}_{r,t}, \qquad \forall r \in \mathcal{R}, \forall t \in \mathcal{T}, \tag{5.26c}$$

$$\overline{f}^{\text{res}}_{r,t}(\underline{\mathbf{x}}_H) = P^{\text{c}}_{r,t} - P^{\text{res}}_{r,t}, \qquad \forall r \in \mathcal{R}, \forall t \in \mathcal{T}, \tag{5.26d}$$

$$\underline{f}^{\text{ch}}_{e,t}(\underline{\mathbf{x}}_H) = -P^{\text{ch}}_{e,t}, \qquad \forall e \in \mathcal{E}, \forall t \in \mathcal{T}, \tag{5.26e}$$

$$\overline{f}^{\text{ch}}_{e,t}(\underline{\mathbf{x}}_H) = P^{\text{ch}}_{e,t} - \overline{P}_e, \qquad \forall e \in \mathcal{E}, \forall t \in \mathcal{T}, \tag{5.26f}$$

$$\underline{f}^{\text{dis}}_{e,t}(\underline{\mathbf{x}}_H) = -P^{\text{dis}}_{e,t}, \qquad \forall e \in \mathcal{E}, \forall t \in \mathcal{T}, \tag{5.26g}$$

$$\overline{f}^{\text{dis}}_{e,t}(\underline{\mathbf{x}}_H) = P^{\text{dis}}_{e,t} - \overline{P}_e, \qquad \forall e \in \mathcal{E}, \forall t \in \mathcal{T}, \tag{5.26h}$$

$$\underline{f}^{\text{soc}}_{e,t}(\underline{\mathbf{x}}_H) = \underline{E}_e - E_{e,0} + \Delta t \sum_{n=1}^{t-1} \left(\eta^{\text{d}}_e P^{\text{dis}}_{e,n} - \eta^{\text{ch}}_e P^{\text{ch}}_{e,n} \right), \qquad \forall e \in \mathcal{E}, \forall t \in \mathcal{T}, \tag{5.26i}$$

$$\overline{f}^{\text{soc}}_{e,t}(\underline{\mathbf{x}}_H) = E_{e,0} + \Delta t \sum_{n=1}^{t-1} \left(\eta^{\text{ch}}_e P^{\text{ch}}_{e,n} - \eta^{\text{d}}_e P^{\text{dis}}_{e,n} \right) - \overline{E}_e, \qquad \forall e \in \mathcal{E}, \forall t \in \mathcal{T}, \tag{5.26j}$$

$$\underline{f}^{\text{bf}}_{bd,t}(\underline{\mathbf{x}}_H) = -f_{bd} - B_{bd}(\theta_{b,t} - \theta_{d,t}), \qquad \forall bd \in \mathcal{L}, \forall t \in \mathcal{T}, \tag{5.26k}$$

$$\overline{f}^{\text{bf}}_{bd,t}(\underline{\mathbf{x}}_H) = B_{bd}(\theta_{b,t} - \theta_{d,t}) - f_{bd}, \qquad \forall bd \in \mathcal{L}, \forall t \in \mathcal{T}. \tag{5.26l}$$

Note that the inequality constraints on the ESS state of charge limits in (5.26i)-(5.26j) are obtained by substituting the ESS dynamics constraint in (5.25g) into the ESS operating bounds in (5.25f) and solving the ESS dynamics model in (5.25g) at the current time step t in terms of all the previous time steps. Similarly, the equality constraint in (5.25i) that enforces the power balance equation at each time t describes H equality constraints. We denote the functions on the right-hand side of the equality constraints in (5.25i) by the function $h_t(\tilde{\underline{\mathbf{x}}}_H)$ for $t = \{1, \ldots, H\}$.

Assume that an optimal solution $\tilde{\underline{\mathbf{x}}}_H$ to (5.25) exists and let $\underline{\lambda}^{\text{part}}_{dev,t}$ and $\overline{\lambda}^{\text{part}}_{dev,t}$ denote the Lagrange multiplier associated with the inequality constraint $\underline{f}^{\text{part}}_{dev,t}(\tilde{\underline{\mathbf{x}}}_H)$ and $\overline{f}^{\text{part}}_{dev,t}(\tilde{\underline{\mathbf{x}}}_H)$, respectively, and let $\mu_{i,t}$ denote the Lagrange multiplier associated with the power balance equality constraint in (5.25i) where the right-hand side is denoted $h_{b,t}(\tilde{\underline{\mathbf{x}}}_H)$ for bus b at time t. Then the KKT conditions are the following:

Primal Feasibility:

$$\underline{f}^{\text{gen}}_{g,t}(\tilde{\underline{\mathbf{x}}}_H), \overline{f}^{\text{gen}}_{g,t}(\tilde{\underline{\mathbf{x}}}_H) \leq 0, \qquad \forall g \in \mathcal{G}, \forall t \in \mathcal{T}, \tag{5.27a}$$

$$\underline{f}^{\text{res}}_{r,t}(\tilde{\underline{\mathbf{x}}}_H), \overline{f}^{\text{res}}_{r,t}(\tilde{\underline{\mathbf{x}}}_H) \leq 0, \qquad \forall r \in \mathcal{R}, \forall t \in \mathcal{T}, \tag{5.27b}$$

$$\underline{f}^{\text{ch}}_{e,t}(\tilde{\underline{\mathbf{x}}}_H), \underline{f}^{\text{dis}}_{e,t}(\tilde{\underline{\mathbf{x}}}_H), \underline{f}^{\text{soc}}_{e,t}(\tilde{\underline{\mathbf{x}}}_H), \overline{f}^{\text{ch}}_{e,t}(\tilde{\underline{\mathbf{x}}}_H), \overline{f}^{\text{dis}}_{e,t}(\tilde{\underline{\mathbf{x}}}_H), \overline{f}^{\text{soc}}_{e,t}(\tilde{\underline{\mathbf{x}}}_H) \leq 0, \qquad \forall e \in \mathcal{E}, \forall t \in \mathcal{T}, \tag{5.27c}$$

$$\underline{f}^{\text{bf}}_{bd,t}(\tilde{\underline{\mathbf{x}}}_H), \overline{f}^{\text{bf}}_{bd,t}(\tilde{\underline{\mathbf{x}}}_H) \leq 0, \qquad \forall bd \in \mathcal{L}, \forall t \in \mathcal{T}, \tag{5.27d}$$

$$h_{b,t}(\tilde{\underline{\mathbf{x}}}_H) = 0, \qquad \forall b \in \mathcal{B}, \forall t \in \mathcal{T}, \tag{5.27e}$$

Dual Feasibility:

$$\underline{\lambda}^{\text{gen}}_{g,t}, \overline{\lambda}^{\text{gen}}_{g,t} \geq 0, \qquad \forall g \in \mathcal{G}, \forall t \in \mathcal{T}, \tag{5.27f}$$

$$\underline{\lambda}^{\text{res}}_{r,t}, \overline{\lambda}^{\text{res}}_{r,t} \geq 0, \qquad \forall r \in \mathcal{R}, \forall t \in \mathcal{T}, \tag{5.27g}$$

$$\underline{\lambda}^{\text{ch}}_{e,t}, \overline{\lambda}^{\text{ch}}_{e,t}, \underline{\lambda}^{\text{dis}}_{e,t}, \overline{\lambda}^{\text{dis}}_{e,t}, \underline{\lambda}^{\text{soc}}_{e,t}, \overline{\lambda}^{\text{soc}}_{e,t} \geq 0, \qquad \forall e \in \mathcal{E}, \forall t \in \mathcal{T}, \tag{5.27h}$$

$$\underline{\lambda}^{\text{bf}}_{bd,t}, \overline{\lambda}^{\text{bf}}_{bd,t} \geq 0, \qquad \forall bd \in \mathcal{L}, \forall t \in \mathcal{T}, \tag{5.27i}$$

Complementary Slackness:

$$\underline{\lambda}^{\text{gen}}_{g,t} \underline{f}^{\text{gen}}_{g,t}(\tilde{\underline{\mathbf{x}}}_H) = \overline{\lambda}^{\text{gen}}_{g,t} \overline{f}^{\text{gen}}_{g,t}(\tilde{\underline{\mathbf{x}}}_H) = 0, \qquad \forall g \in \mathcal{G}, \forall t \in \mathcal{T}, \tag{5.27j}$$

$$\underline{\lambda}^{\text{res}}_{r,t} \underline{f}^{\text{res}}_{r,t}(\tilde{\underline{\mathbf{x}}}_H) = \overline{\lambda}^{\text{res}}_{r,t} \overline{f}^{\text{res}}_{r,t}(\tilde{\underline{\mathbf{x}}}_H) = 0, \qquad \forall r \in \mathcal{R}, \forall t \in \mathcal{T}, \tag{5.27k}$$

$$\begin{aligned} &\underline{\lambda}^{\text{ch}}_{e,t} \underline{f}^{\text{ch}}_{e,t}(\tilde{\underline{\mathbf{x}}}_H) = \underline{\lambda}^{\text{dis}}_{e,t} \underline{f}^{\text{dis}}_{e,t}(\tilde{\underline{\mathbf{x}}}_H) = \underline{\lambda}^{\text{soc}}_{e,t} \underline{f}^{\text{soc}}_{e,t}(\tilde{\underline{\mathbf{x}}}_H) = 0, \\ &\overline{\lambda}^{\text{ch}}_{e,t} \overline{f}^{\text{ch}}_{e,t}(\tilde{\underline{\mathbf{x}}}_H) = \overline{\lambda}^{\text{dis}}_{e,t} \overline{f}^{\text{dis}}_{e,t}(\tilde{\underline{\mathbf{x}}}_H) = \overline{\lambda}^{\text{soc}}_{e,t} \overline{f}^{\text{soc}}_{e,t}(\tilde{\underline{\mathbf{x}}}_H) = 0, \qquad \forall e \in \mathcal{E}, \forall t \in \mathcal{T}, \end{aligned} \tag{5.27l}$$

$$\underline{\lambda}^{\text{bf}}_{bd,t} \underline{f}^{\text{bf}}_{bd,t}(\tilde{\underline{\mathbf{x}}}_H) = \overline{\lambda}^{\text{bf}}_{bd,t} \overline{f}^{\text{bf}}_{bd,t}(\tilde{\underline{\mathbf{x}}}_H) = 0, \qquad \forall bd \in \mathcal{L}, \forall t \in \mathcal{T}, \tag{5.27m}$$

Stationarity:

$$\begin{aligned} &\nabla f_{\text{tot}}(\tilde{\underline{\mathbf{x}}}_H) + \sum_{t=1}^{H} \Bigg(\sum_{g \in \mathcal{G}} (\underline{\lambda}^{\text{gen}}_{g,t} \nabla \underline{f}^{\text{gen}}_{g,t}(\tilde{\underline{\mathbf{x}}}_H) + \overline{\lambda}^{\text{gen}}_{g,t} \nabla \overline{f}^{\text{gen}}_{g,t}(\tilde{\underline{\mathbf{x}}}_H)) \\ &+ \sum_{r \in \mathcal{R}} (\underline{\lambda}^{\text{res}}_{r,t} \nabla \underline{f}^{\text{res}}_{r,t}(\tilde{\underline{\mathbf{x}}}_H) + \overline{\lambda}^{\text{res}}_{r,t} \nabla \overline{f}^{\text{res}}_{r,t}(\tilde{\underline{\mathbf{x}}}_H)) \\ &+ \sum_{e \in \mathcal{E}} (\underline{\lambda}^{\text{ch}}_{e,t} \nabla \underline{f}^{\text{ch}}_{e,t}(\tilde{\underline{\mathbf{x}}}_H) + \overline{\lambda}^{\text{ch}}_{e,t} \nabla \overline{f}^{\text{ch}}_{e,t}(\tilde{\underline{\mathbf{x}}}_H) + \underline{\lambda}^{\text{dis}}_{e,t} \nabla \underline{f}^{\text{dis}}_{e,t}(\tilde{\underline{\mathbf{x}}}_H) + \overline{\lambda}^{\text{dis}}_{e,t} \nabla \overline{f}^{\text{dis}}_{e,t}(\tilde{\underline{\mathbf{x}}}_H) \\ &+ \underline{\lambda}^{\text{soc}}_{e,t} \nabla \underline{f}^{\text{soc}}_{e,t}(\tilde{\underline{\mathbf{x}}}_H) + \overline{\lambda}^{\text{soc}}_{e,t} \nabla \overline{f}^{\text{soc}}_{e,t}(\tilde{\underline{\mathbf{x}}}_H)) \\ &+ \sum_{bd \in \mathcal{L}} (\underline{\lambda}^{\text{bf}}_{bd,t} \nabla \underline{f}^{\text{bf}}_{bd,t}(\tilde{\underline{\mathbf{x}}}_H) + \overline{\lambda}^{\text{bf}}_{bd,t} \nabla \overline{f}^{\text{bf}}_{bd,t}(\tilde{\underline{\mathbf{x}}}_H)) + \sum_{b \in \mathcal{B}} \mu_{b,t} \nabla h_{b,t}(\tilde{\underline{\mathbf{x}}}_H) \Bigg) \in \mathbf{0}, \end{aligned} \tag{5.27n}$$

where $\mathbf{0} \in \mathbb{R}^{H(|\mathcal{G}|+|\mathcal{R}|+2|\mathcal{E}|+|\mathcal{L}|)}$. Recall that for convex optimization problems with differentiable objective functions, any solution that satisfies the KKT conditions given in (5.27a)-(5.27n) is optimal [22]. In the proof of Proposition 5.3, we leverage the KKT conditions to give a series of conditions that must be satisfied to guarantee non-simultaneous ESS charging and discharging in

the DC OPF problem given in (5.25). We decompose the condition in (5.27n) into:

$$\partial_{P^{\mathrm{G}}_{g,t}} f_{\mathrm{tot}}(\tilde{\underline{\mathbf{x}}}_H) - \underline{\lambda}^{\mathrm{gen}}_{g,t} + \overline{\lambda}^{\mathrm{gen}}_{g,t} - \mu_{b,t} = 0, \qquad \forall g \in \mathcal{G}_b, \forall t \in \mathcal{T}, \quad (5.28)$$

$$-\underline{\lambda}^{\mathrm{res}}_{r,t} + \overline{\lambda}^{\mathrm{res}}_{r,t} + \mu_{b,t} = 0, \qquad \forall r \in \mathcal{R}_b, \forall b \in \mathcal{B}, \forall t \in \mathcal{T}, \quad (5.29)$$

$$\partial_{P^{\mathrm{ch}}_{e,t}} f_{\mathrm{tot}}(\tilde{\underline{\mathbf{x}}}_H) - \underline{\lambda}^{\mathrm{ch}}_{e,t} + \overline{\lambda}^{\mathrm{ch}}_{e,t} + \eta^{\mathrm{ch}}_e \Delta t \sum_{n=t}^{H} (\overline{\lambda}^{\mathrm{soc}}_{e,n} - \underline{\lambda}^{\mathrm{soc}}_{e,n}) + \mu_{b,t} = 0, \quad \forall e \in \mathcal{E}_b, \forall b \in \mathcal{B}, \forall t \in \mathcal{T}, \quad (5.30)$$

$$\partial_{P^{\mathrm{dis}}_{e,t}} f_{\mathrm{tot}}(\tilde{\underline{\mathbf{x}}}_H) - \underline{\lambda}^{\mathrm{dis}}_{e,t} + \overline{\lambda}^{\mathrm{dis}}_{e,t} + \eta^{\mathrm{d}}_e \Delta t \sum_{n=t}^{H} (\underline{\lambda}^{\mathrm{soc}}_{e,n} - \overline{\lambda}^{\mathrm{soc}}_{e,n}) - \mu_{b,t} = 0, \quad \forall e \in \mathcal{E}_b, \forall b \in \mathcal{B}, \forall t \in \mathcal{T}, \quad (5.31)$$

$$\sum_{d \in \mathcal{B}_b} B_{bd} (\overline{\lambda}^{\mathrm{bf}}_{bd,t} - \underline{\lambda}^{\mathrm{bf}}_{bd,t} - \mu_{d,t}) + \mu_{b,t} \sum_{d \in \mathcal{B}_b} B_{bd} = 0, \qquad \forall b \in \mathcal{B}, \forall t \in \mathcal{T}. \quad (5.32)$$

5.3.2.2 Relaxed Convex ESS Model Behavior Guarantees in the DC OPF Problem

In Proposition 5.3, we show that solutions with nonzero ESS charging and discharging during the same time step for the model in (5.1) used in the DC OPF problem is suboptimal when certain conditions are satisfied. These conditions ensure that physically unrealizable policies where we simultaneously charge and discharge the ESS are not optimal. Note that the presence or absence of a load at a bus does not have an affect on the results of Proposition 5.3. At the conclusion of the proof, we comment on how the conditions in Proposition 5.3 naturally arise in the DC OPF setting. For the following discussion, the phrase "for some" should be interpreted to mean "at least one."

Proposition 5.3 Let $f_{\mathrm{tot}}(\underline{\mathbf{x}}_H)$ be a differentiable convex cost function where $\partial_{P^{\mathrm{ch}}_{e,t}} f_{\mathrm{tot}}(\tilde{\underline{\mathbf{x}}}_H) \geq 0$, $\partial_{P^{\mathrm{dis}}_{e,t}} f_{\mathrm{tot}}(\tilde{\underline{\mathbf{x}}}_H) \geq 0$ and $(\partial_{P^{\mathrm{ch}}_{e,t}} f_{\mathrm{tot}}(\tilde{\underline{\mathbf{x}}}_H) + \partial_{P^{\mathrm{dis}}_{e,t}} f_{\mathrm{tot}}(\tilde{\underline{\mathbf{x}}}_H)) > 0$ for all $e \in \mathcal{E}_b$ and $t \in \{1, \ldots, H\}$. A solution to (5.25) where $0 < \tilde{P}^{\mathrm{ch}}_{e,t}, \tilde{P}^{\mathrm{dis}}_{e,t} \leq \overline{P}_e$ for some ESS $e \in \mathcal{E}_b$ at bus $b \in \mathcal{B}$ and at some time $t \in \{1, \ldots, H\}$ is suboptimal if at least one of the following conditions is satisfied:

C1) $\partial_{P^{\mathrm{G}}_{g,t}} f_{\mathrm{tot}}(\tilde{\underline{\mathbf{x}}}_H) \geq 0$ and $\underline{P}^{\mathrm{G}}_g < \tilde{P}^{\mathrm{G}}_{g,t} \leq \overline{P}^{\mathrm{G}}_g$ for some $g \in \mathcal{G}_b$,

C2) $0 \leq \tilde{P}^{\mathrm{c}}_{r,t} < P^{\mathrm{res}}_{r,t}$ for some $r \in \mathcal{R}_b$,

C3) $\underline{E}_e \leq \tilde{E}_{e,n} < \overline{E}_e$ for all $n \in \{t+1, \ldots, H\}$ for some $e \in \mathcal{E}_b$, or

C4) $-f_{bd} \leq B_{bd}(\tilde{\theta}_{b,t} - \tilde{\theta}_{d,t}) < f_{bd}$ for all $d \in \mathcal{B}_b$ and $\sum_{d\in\mathcal{B}_b} \mu_{d,t} \geq 0$.

Proof. Let $\tilde{\underline{\mathbf{x}}}_H$ be an optimal solution to $(\mathcal{P}_1)$. We will prove this claim by contradiction. So, assume that the optimal solution $\tilde{\mathbf{x}}_\tau = [\{\tilde{P}^{\mathrm{G}}_{g,\tau}\}_{g\in\mathcal{G}}, \{\tilde{P}^{\mathrm{ch}}_{e,\tau},\ \tilde{P}^{\mathrm{dis}}_{e,\tau}\}_{e\in\mathcal{E}}, \{\tilde{P}^{\mathrm{c}}_{r,\tau}\}_{r\in\mathcal{R}}, \{\tilde{\theta}_{b,\tau}\}_{b\in\mathcal{B}}]^T$ at some time $\tau \in \{1,\ldots,H\}$ is such that for some ESS $\kappa \in \mathcal{E}_b$ there is simultaneous charging and discharging, i.e., $0 < \tilde{P}^{\mathrm{ch}}_{\kappa,\tau}, \tilde{P}^{\mathrm{dis}}_{\kappa,\tau} \leq \overline{P}_\kappa$. We use the complementary slackness conditions at time $\tau \in \{1,\ldots,H\}$ in (5.27l) with our assumption on the operation of ESS κ to determine that $\underline{\lambda}^{\mathrm{ch}}_{\kappa,\tau} = \underline{\lambda}^{\mathrm{dis}}_{\kappa,\tau} = 0$ and $\overline{\lambda}^{\mathrm{ch}}_{\kappa,\tau}, \overline{\lambda}^{\mathrm{dis}}_{\kappa,\tau} \geq 0$. Using the above conditions on the Lagrange multipliers at time τ together with (5.30)-(5.31), we have:

$$\partial_{P^{\mathrm{ch}}_{\kappa,\tau}} f_{\mathrm{tot}}(\tilde{\underline{\mathbf{x}}}_H) + \overline{\lambda}^{\mathrm{ch}}_{\kappa,\tau} + \eta^{\mathrm{ch}}_\kappa \Delta t \sum_{n=\tau}^{H} (\overline{\lambda}^{\mathrm{soc}}_{\kappa,n} - \underline{\lambda}^{\mathrm{soc}}_{\kappa,n}) + \mu_{b,\tau} = 0, \tag{5.33}$$

$$\partial_{P^{\mathrm{dis}}_{\kappa,\tau}} f_{\mathrm{tot}}(\tilde{\underline{\mathbf{x}}}_H) + \overline{\lambda}^{\mathrm{dis}}_{\kappa,\tau} + \eta^{\mathrm{d}}_\kappa \Delta t \sum_{n=\tau}^{H} (\underline{\lambda}^{\mathrm{soc}}_{\kappa,n} - \overline{\lambda}^{\mathrm{soc}}_{\kappa,n}) - \mu_{b,\tau} = 0, \tag{5.34}$$

Solving for $\mathcal{I} = \sum_{n=\tau}^{H} (\overline{\lambda}^{\mathrm{soc}}_{\kappa,n} - \underline{\lambda}^{\mathrm{soc}}_{\kappa,n})$ in (5.33), and then replacing $-\mathcal{I}$ in (5.34), we get:

$$\partial_{P^{\mathrm{dis}}_{\kappa,\tau}} f_{\mathrm{tot}}(\tilde{\underline{\mathbf{x}}}_H) + \frac{\eta^{\mathrm{d}}_\kappa}{\eta^{\mathrm{ch}}_\kappa} \partial_{P^{\mathrm{ch}}_{\kappa,\tau}} f_{\mathrm{tot}}(\tilde{\underline{\mathbf{x}}}_H) + \overline{\lambda}^{\mathrm{dis}}_{\kappa,\tau} + \frac{\eta^{\mathrm{d}}_\kappa}{\eta^{\mathrm{ch}}_\kappa} \overline{\lambda}^{\mathrm{ch}}_{\kappa,\tau} + \mu_{b,\tau} \left(\frac{\eta^{\mathrm{d}}_\kappa}{\eta^{\mathrm{ch}}_\kappa} - 1 \right) = 0. \tag{5.35}$$

Notice that with our assumptions on the cost function $f_{\mathrm{tot}}(\tilde{\underline{\mathbf{x}}}_H)$, the sum of the first two terms in (5.35) is strictly positive. Then with the dual feasibility condition in (5.27h), we obtain a contradiction in (5.35) when $\mu_{b,\tau} \geq 0$. For each condition in the proposition statement, we will show how this affects $\mu_{b,\tau}$ to result in a contradiction proving that a solution with nonzero ESS charging and discharging is suboptimal.

First, we consider Condition C1 where $\partial_{P^{\mathrm{G}}_{g,\tau}} f_{\mathrm{tot}}(\tilde{\underline{\mathbf{x}}}_H) \geq 0$ and $\underline{P}^{\mathrm{G}}_g < \tilde{P}^{\mathrm{G}}_{g,\tau} \leq \overline{P}^{\mathrm{G}}_g$ for some $g \in \mathcal{G}_b$. Using the dual feasibility and complementary slackness conditions in (5.27f) and (5.27j), respectively, and (5.28) with the assumption on $\tilde{P}^{\mathrm{G}}_{g,\tau}$, we determine $\underline{\lambda}^{\mathrm{gen}}_{g,\tau} = 0$ and $\mu_{b,\tau} = \partial_{P^{\mathrm{G}}_{g,\tau}} f_{\mathrm{tot}}(\tilde{\underline{\mathbf{x}}}_H) + \overline{\lambda}^{\mathrm{gen}}_{g,\tau}$. Then $\mu_{b,\tau} \geq 0$, and since the sum of the first two terms in (5.35) are positive by assumption, we obtain a contradiction since the left-hand-side of (5.35) cannot equal 0. Thus, a solution where $0 < \tilde{P}^{\mathrm{ch}}_{e,t}, \tilde{P}^{\mathrm{dis}}_{e,t} \leq \overline{P}_e$ for any ESS $e \in \mathcal{E}_b$ at time t is suboptimal if $\partial_{P^{\mathrm{G}}_{g,\tau}} f_{\mathrm{tot}}(\tilde{\underline{\mathbf{x}}}_H) \geq 0$ and $\underline{P}^{\mathrm{G}}_g < \tilde{P}^{\mathrm{G}}_{g,\tau} \leq \overline{P}^{\mathrm{G}}_g$ for some $g \in \mathcal{G}_b$ at time $t \in \{1,\ldots,H\}$, because it does not satisfy the KKT conditions for the DC OPF problem.

Next, we consider Condition C2 where the optimal solution is such that $0 \leq \tilde{P}^{\mathrm{c}}_{r,\tau} < P^{\mathrm{res}}_{r,\tau}$ for some $r \in \mathcal{R}_b$. Using the dual feasibility and complementary slackness conditions in (5.27g) and (5.27k), respectively, and with (5.29), we determine $\overline{\lambda}^{\mathrm{res}}_{r,\tau} = 0$ and $\mu_{b,\tau} = \underline{\lambda}^{\mathrm{res}}_{r,\tau}$. Then $\mu_{b,\tau} \geq 0$, which again results in a contradiction since the left-hand-side of (5.35) cannot equal 0. Thus, a solution where any ESS $e \in \mathcal{E}_b$ simultaneously charges and discharges at time t is suboptimal if $0 \leq \tilde{P}^{\mathrm{c}}_{r,t} < P^{\mathrm{res}}_{r,t}$ for some $r \in \mathcal{R}_b$, because the KKT conditions for the DC OPF problem are not satisfied at time t.

Next, we consider Condition C3 where $\underline{E}_\kappa \leq \tilde{E}_{\kappa,n} < \overline{E}_\kappa$ for all times $n \in \{\tau+1, \ldots, H\}$ for ESS $\kappa \in \mathcal{E}_b$. Using the dual feasibility and complementary slackness conditions in (5.27h) and (5.27l), respectively, we determine $\sum_{n=\tau}^{H} \overline{\lambda}^{\mathrm{soc}}_{\kappa,n} = 0$. Then (5.34) becomes:

$$\partial_{P^{\mathrm{dis}}_{\kappa,\tau}} f_{\mathrm{tot}}(\tilde{\underline{\mathbf{x}}}_H) + \overline{\lambda}^{\mathrm{dis}}_{\kappa,\tau} + \eta^{\mathrm{d}}_\kappa \Delta t \sum_{n=\tau}^{H} \underline{\lambda}^{\mathrm{soc}}_{\kappa,n} - \mu_{b,\tau} = 0,$$

which implies $\mu_{b,\tau} \geq 0$ by the dual feasibility condition and the assumption $\partial_{P^{\mathrm{dis}}_{\kappa,\tau}} f_{\mathrm{tot}}(\tilde{\underline{\mathbf{x}}}_H) \geq 0$. Since $\mu_{b,\tau} \geq 0$, we obtain a contradiction in (5.35) since the left-hand-side cannot equal zero. Thus, if the solution is such that $\underline{E}_e \leq \tilde{E}_{e,n} < \overline{E}_e$ for all $n \in \{t+1, \ldots, H\}$ for some ESS $e \in \mathcal{E}_b$, then simultaneous charging and discharging, i.e., $0 < \tilde{P}^{\mathrm{ch}}_{e,t}, \tilde{P}^{\mathrm{dis}}_{e,t} \leq \overline{P}_e$, is suboptimal at time t.

Lastly, we consider Condition C4 where $-f_{bd} \leq B_{bd}(\tilde{\theta}_{b,\tau} - \tilde{\theta}_{d,\tau}) < f_{bd}$ for all $d \in \mathcal{B}_b$ and $\sum_{d \in \mathcal{B}_b} \mu_{d,\tau} \geq 0$. Using the dual feasibility and complementary slackness conditions in (5.27i) and (5.27m), respectively, we determine that $\overline{\lambda}^{\mathrm{bf}}_{bd,\tau} = 0$ and $\underline{\lambda}^{\mathrm{bf}}_{bd,\tau} \geq 0$. Then (5.32) becomes:

$$\sum_{d \in \mathcal{B}_b} B_{bd}(-\underline{\lambda}^{\mathrm{bf}}_{bd,\tau} - \mu_{d,\tau}) + \mu_{b,\tau} \sum_{d \in \mathcal{B}_b} B_{bd} = 0,$$

where $B_{bd} \geq 0$, and with the assumption that $\sum_{d \in \mathcal{B}_b} \mu_{d,\tau} \geq 0$, we have $\mu_{b,\tau} \geq 0$. Since $\mu_{b,\tau} \geq 0$, we obtain a contradiction in (5.35) since the left-hand-side must be strictly positive. Thus, if the system is such that $-f_{bd} \leq B_{bd}(\tilde{\theta}_{b,t} - \tilde{\theta}_{d,t}) < f_{bd}$ for all $d \in \mathcal{B}_b$ and $\sum_{d \in \mathcal{B}_b} \mu_{d,t} \geq 0$ at time $t \in \{1, \ldots, H\}$, then a solution where there is simultaneous charging and discharging, i.e., $0 < \tilde{P}^{\mathrm{ch}}_{e,t}, \tilde{P}^{\mathrm{dis}}_{e,t} \leq \overline{P}_e$ for any ESS $e \in \mathcal{E}_b$, is suboptimal.

Thus, if any of the four conditions above are satisfied for all time $t \in \{1, \ldots, H\}$, then a feasible point where there is simultaneous charging and discharging for any ESS $e \in \mathcal{E}_b$ at any time

$t \in \{1, \ldots, H\}$ in the MPC prediction horizon will be suboptimal. □

5.3.2.3 Further Discussion on Proposition 5.3

Conditions C1-C4 given in Proposition 5.3, which ensure an optimal solution with non-simultaneous ESS charging and discharging, naturally arise in the DC OPF problem. Condition C1 captures the situation when the cost function is designed to satisfy $\partial_{P^{\mathrm{G}}_{g,\tau}} f_{\mathrm{tot}}(\underline{\tilde{\mathbf{x}}}_H) \geq 0$ and there is at least one dispatchable energy source $g \in \mathcal{G}_b$ that is operating above its minimum generation output for some time $\tau \in \{1, \ldots, H\}$. A commonly used cost function is a quadratic penalty on dispatchable power generation which satisfies the assumption on the partial derivative of the cost function $\partial_{P^{\mathrm{G}}_{g,\tau}} f_{\mathrm{tot}}(\underline{\tilde{\mathbf{x}}}_H) \geq 0$ [47, 89, 94, 101–103]. Additionally, to satisfy the load throughout the network, it is optimal for the dispatchable generator to be operating above its minimum generation output. Condition C2 is the case where there is at least one non-dispatchable energy source $r \in \mathcal{R}_b$ that is not curtailing all available generation. This condition is commonly met since it is not optimal in this setting to curtail non-dispatchable power sources (such as wind and solar) to meet the network load. Condition C3 captures the situation where the optimal charging and discharging strategy is such that the ESS $\kappa \in \mathcal{E}_b$ will not attain the maximum SOC during times $n \in \{\tau + 1, \ldots, H\}$. Condition C3 will be easily met when the excess solar energy after serving the network load is less than the available ESS capacity for times $n \in \{\tau + 1, \ldots, H\}$. Condition C4 describes when the line congestion does not attain its upper power flow limit for lines connecting adjacent buses $d \in \mathcal{B}_b$ to bus b and the sum of Lagrange multipliers corresponding to the power balance constraint at adjacent buses is non-negative at time $\tau \in \mathcal{T}$.

Next, we provide a remark on when a penalty on ESS charging or discharging does not need to be included in the overall objective function, i.e., when $\partial_{P^{\mathrm{dis}}_{\kappa,\tau}} f_{\mathrm{tot}}(\underline{\tilde{\mathbf{x}}}_H) = \partial_{P^{\mathrm{ch}}_{\kappa,\tau}} f_{\mathrm{tot}}(\underline{\tilde{\mathbf{x}}}_H) = 0$, to ensure non-simultaneous charging and discharging, which follows directly from Proposition 5.3. We also provide a remark on conditions when the penalty reformulation does not ensure proper ESS charging and discharging behavior.

Remark 5.1 If the system is such that for some $g \in \mathcal{G}_b$, $\underline{P}_g^{\mathrm{G}} < \tilde{P}_{g,t}^{\mathrm{G}} \leq \overline{P}_g^{\mathrm{G}}$ and $\partial_{P_{g,t}^{\mathrm{G}}} f_{\mathrm{tot}}(\tilde{\underline{\mathbf{x}}}_H) > 0$ for all $t \in \{1, \ldots, H\}$, then for each ESS $e \in \mathcal{E}_b$ it will be suboptimal to simultaneously charge and discharge for all time $t \in \{1, \ldots, H\}$ without the use of the penalty approach, i.e., the cost function can be chosen such that $\partial_{P_{e,\tau}^{\mathrm{dis}}} f_{\mathrm{tot}}(\tilde{\underline{\mathbf{x}}}_H) = \partial_{P_{e,\tau}^{\mathrm{ch}}} f_{\mathrm{tot}}(\tilde{\underline{\mathbf{x}}}_H) = 0$.

Remark 5.2 If the system is such that for some $g \in \mathcal{G}_b$, $\underline{P}_g^{\mathrm{G}} = \tilde{P}_{g,t}^{\mathrm{G}} \leq \overline{P}_g^{\mathrm{G}}$ or for some $r \in \mathcal{R}_b$, $\tilde{P}_{r,t}^{\mathrm{c}} = P_{r,t}^{\mathrm{res}}$ at time $t \in \{1, \ldots, H\}$, then the penalty reformulation does not ensure that a solution with simultaneous charging and discharging to the DC OPF problem with the convex relaxed ESS model will be suboptimal.

5.3.3 Case Study: Proper Energy Storage System Model Behavior in DC OPF

To demonstrate the charging and discharging behavior of the ESS model, we provide simulation results on the IEEE 14-bus, 57-bus, and 118-bus test systems using MATPOWER's quadratic generation cost parameters [104] for the proposed MPC-based DC OPF problem in (5.25). The system is modified to include non-dispatchable renewable sources, i.e., photovoltaic (PV) sources, and ESSs. We first use the smaller modified IEEE 14-bus test system to highlight the ESS model behavior with respect to the conditions presented in Proposition 5.3. We then provide simulation results on larger, modified IEEE 57-bus and 118-bus test systems to compare the computation time using the proposed linear ESS model in (5.1) versus the same model with the non-convex complementarity constraint in (5.2) included. The network load data is obtained from PJM's publicly available database [105] and the solar data is obtained from NREL's Solar Power Data for Integration Studies [106]. The simulation has a 12-hour prediction horizon ($H = 12$) with 1 hour time intervals ($\Delta t = 1$). The MPC-based DC OPF problem in (5.25) is implemented in Python using the Pyomo [107,108] optimization modeling language, and uses the MATPOWER data parser and other select functions from EGRET [80]. The simulations in this work were performed on a computer with a 2.4 GHz Intel Core i5 processor with 8 GB of RAM. For the following simulations,

we use the quadratic cost function:

$$f_{\text{tot}}(\underline{\mathbf{x}}_H) = \sum_{t=1}^{H} \left(\sum_{g \in \mathcal{G}} (a_g (P_{g,t}^{\text{G}})^2 + b_g P_{g,t}^{\text{G}} + c_g) + \sum_{e \in \mathcal{E}} \rho_e P_{e,t}^{\text{ch}} \right), \tag{5.36}$$

where the generation cost parameters satisfy $a_g > 0$, $b_g > 0$, $c_g \geq 0$ for all $g \in \mathcal{G}$, and $\rho_e > 0$ for each $e \in \mathcal{E}$ will be specified in each simulation. The penalty function is a linear penalty on ESS charging to capture future ESS replacement costs.

5.3.3.1 Simulation Results for IEEE 14-bus Test System

The MPC-based DC OPF problem in (5.25) is first simulated with the convex ESS model in (5.1) and the cost function in (5.36) where $\rho_e = 0.01$ for all $e \in \mathcal{E}$. We modify the IEEE 14-bus test system by adding 7 PV sources and 10 ESSs, as described in Table 5.6. Note that shaded entries in the tables throughout Section 5.3.3 imply "not applicable." Thus, bus 6 reflects the case when any of Conditions C1, C3, or C4 can hold (traditional power generator and ESS); buses 2, 3, and 8 reflect when Conditions C1-C4 can hold (traditional power generator, solar, and ESS); and buses 9, 10, and 12 reflect when Conditions C2-C4 can hold (solar and ESS). The ESS charging efficiency η_e^{ch} is randomly chosen from $[0.92, 0.93, \ldots, 0.97]$, and the ESS capacity $\overline{E}_e$ is randomly chosen from $[20, 25, \ldots, 50]$ for each ESS $e \in \mathcal{E}$. The discharging efficiency for each ESS is $\eta_e^{\text{d}} = \frac{1}{\eta_e^{\text{ch}}}$. The maximum charging/discharging power P_e is chosen to be 60% of the ESS capacity $\overline{E}_e$. The simulation results are provided in Fig. 5.5. The power profiles shown in Fig. 5.5 at three of the modified buses demonstrate non-simultaneous ESS charging and discharging when the conditions in Proposition 5.3 are satisfied. We show power profiles for buses 6, 8, and 12 since they together capture all the conditions possible in Proposition 5.3.

Next, the MPC-based DC OPF problem in (5.25) is simulated with the convex ESS model in (5.1) and with the cost function in (5.36). For this simulation, the penalty parameter for the ESS at bus 12 has been modified to $\rho_e = 0$, i.e., only the ESS at bus 12 is not penalized so $\partial_{P_{e,t}^{\text{ch}}} f_{\text{tot}}(\tilde{\underline{\mathbf{x}}}_H) = \partial_{P_{e,t}^{\text{dis}}} f_{\text{tot}}(\tilde{\underline{\mathbf{x}}}_H) = 0$. The penalty parameter for all ESSs except the one at bus 12 is $\rho_e = 0.01$, as in the previous simulation. The power profiles in Fig. 5.6 show that simultaneous

Table 5.6: Bus locations of PV sources and ESSs in each DC OPF simulation.

Type	14-Bus System	57-Bus System	118-Bus System
PV	2, 3, 5, 8-10, 12	2, 5, 7-9, 14, 17, 25, 29, 31, 32, 37, 42, 45, 49, 52, 53, 55	4, 9, 13, 16, 18, 27, 33, 49, 58, 61, 63, 64, 73, 84, 98, 101, 103, 109
ESS (10)	2, 3, 5-10, 12, 14	7, 9, 12, 14, 25, 30, 42, 49, 52, 56	16, 18, 19, 27, 37, 49, 84, 90, 98, 101
ESS (15)		1-3, 5, 7, 9, 14, 25, 29, 36, 37, 42, 49, 50, 52	3, 5, 9, 16, 18, 27, 49, 58, 73, 83, 84, 98, 99, 101, 103
ESS (20)		1-3, 5, 7-9, 14, 17, 21, 25, 29, 36, 37, 40, 42, 48, 49, 52, 53	2, 9, 13, 16, 18, 27, 33, 35, 49, 57, 58, 63, 73, 83, 84, 98, 99, 101, 103, 105

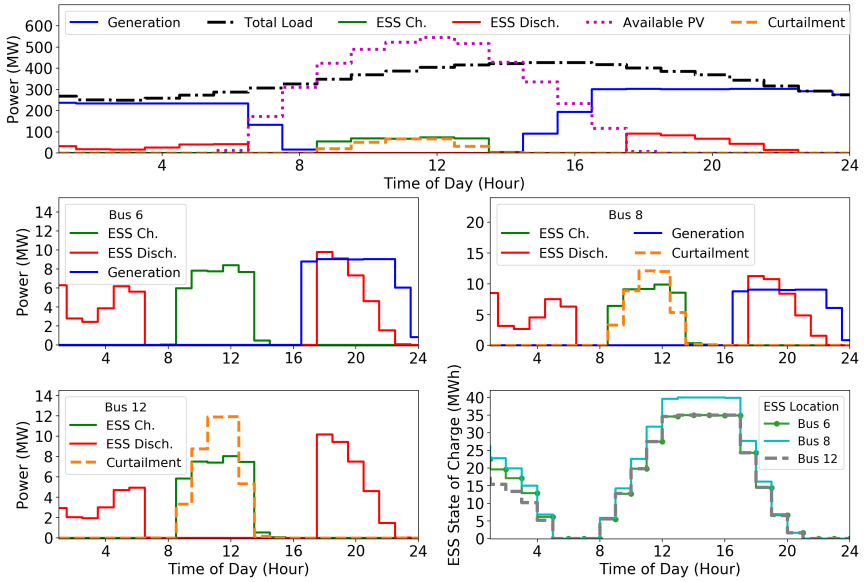

Figure 5.5: Simulation results for the DC OPF when the conditions in Proposition 5.3 are satisfied, highlighting the power profiles for total generation, available solar, total curtailment, and total ESS charging and discharging to optimally satisfy the total network load (top). Power profiles at bus 6 (middle left). Power profiles at bus 8 (middle right). Power profiles at bus 12 (bottom left). SOC of ESSs (bottom right).

ESS charging and discharging at bus 12 does occur from Hour 9 to 14 when the conditions in Proposition 5.3 are not satisfied. The simulation in Fig. 5.6 also shows proper non-simultaneous ESS charging and discharging behavior buses 6 and 8 since the penalty parameter for the ESSs

at those buses ensures the desired ESS model behavior. The difference between Fig. 5.5 and Fig. 5.6 are negligible aside from the charging and discharging strategy for the ESS at bus 12, which demonstrates that changing the penalty parameter on one ESS does not significantly impact the other optimization decisions.

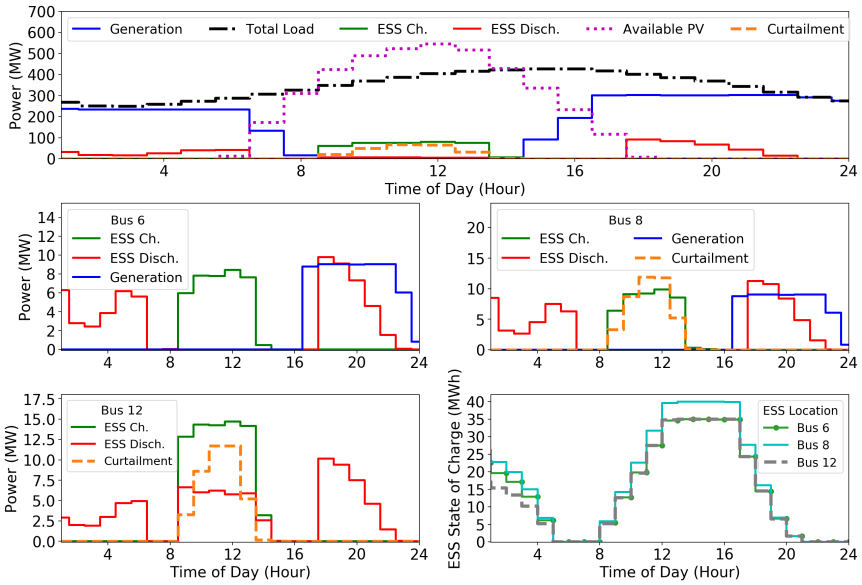

Figure 5.6: Simulation results for the DC OPF when the conditions in Proposition 5.3 are NOT satisfied, highlighting the power profiles for total generation, available solar, total curtailment, and total ESS charging and discharging to optimally satisfy the total network load (top). Power profiles at bus 6 (middle left). Power profiles at bus 8 (middle right). Power profiles at bus 12 (bottom left). SOC of ESSs (bottom right).

Next, we provide simulations to illustrate the relationship between the penalty parameter ρ_e and the numerical complementarity gap, which we define as:

$$\text{Numerical Complementarity Gap} = \sum_{t=1}^{24} \tilde{P}_{e,t}^{\text{ch}} \cdot \tilde{P}_{e,t}^{\text{dis}} \tag{5.37}$$

for an ESS $e \in \mathcal{E}$, which should be numerically close to zero. We again simulate the DC OPF problem in (5.25) with the relaxed convex ESS model and with the cost function as in (5.36) for varying magnitudes of the penalty parameter $\rho_e = [10^{-4},\ 10^{-3}, \ldots, 10^{1}]$ for the ESS at bus 12 and where $\rho_e = 0.01$ for all other ESSs in the network. Similar approaches for tuning the penalty parameter are presented in [24, 28]. The simulation results for the ESS at bus 12 is shown in

Fig. 5.7. In each of the plots showing the ESS behavior at bus 12, ESS behavior does not change

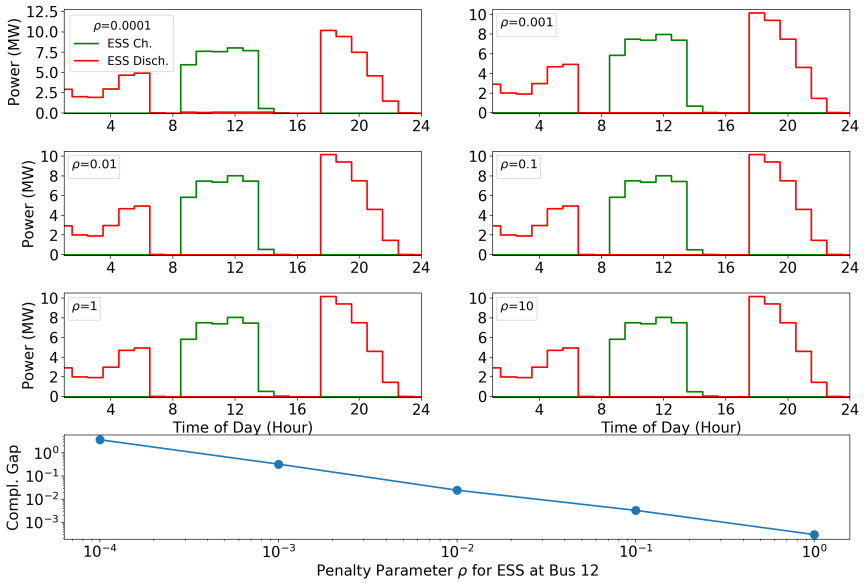

Figure 5.7: Charging and discharging behavior of the ESS located at bus 12 as the penalty parameter ρ_e increases in magnitude. (bottom): Numerical complementarity gap (Compl. Gap) as penalty parameter ρ_e increases in magnitude.

significantly as ρ_e is increased, although simultaneous charging and discharging is observed when $\rho_e = 0.0001$ from Hour 9 to 14. Furthermore, from Fig. 5.7 we can see that including the penalty parameter ρ_e to ensure proper ESS model behavior has a negligible impact on the optimal charging and discharging strategies for various values of ρ_e. In Fig. 5.7 (bottom) we highlight that the numerical complementarity gap decreases as the penalty parameter increases, which demonstrates that tuning may be necessary to ensure the convex relaxation of the ESS model achieves ESS non-simultaneous charging and discharging behavior given a desired numerical complementarity gap tolerance. Note that for $\rho_e = 10^1$, the numerical complementarity gap is equal to zero. The numerical complementarity gap can also be further decreased for a given penalty parameter by tightening the solver termination convergence tolerance.

5.3.3.2 Simulation Results for Larger Networks

In this section, additional simulations on larger networks, i.e., the IEEE 57-bus and 118-bus test systems, were performed for each ESS model - both the convex model in (5.1) and the same model with the complementarity constraint (5.2) included. The simulations with the non-convex ESS model are solved using IPOPT [109]. For each network, it is solved with 10 ESSs, 15 ESSs, and 20 ESSs. The bus locations of the non-dispatchable PV sources and ESSs are given in Table 5.6, and the ESS efficiency and capacity parameters were randomly chosen in the same way as described for the IEEE 14-bus test system study in Section 5.3.3.1. The cost function in (5.36) with the penalty parameter value $\rho_e = 0.01$ is used for each simulation with the RC ESS model. The penalty term in the objective function is omitted when the NC ESS model is used. We first compare the computation time when the proposed relaxed convex, linear (RC) ESS model in (5.1) is used versus when the non-convex (NC) ESS model with the complementarity constraint in (5.2) is used in the MPC-based DC OPF problem. Table 5.7 summarizes the computation time results for both the RC and NC ESS models for each network. Table 5.7 shows both the average computation time for each iteration (24 iterations total) of the MPC-based DC OPF problem with a 12 hour prediction horizon, and the total time the 24 hour simulation took to complete. To measure the computation time savings by using the linear, convex ESS model in (5.1), we define the Speed-up Factor metric as:

$$\text{Speed-up Factor (SF)} = \frac{t_{\text{NC}}}{t_{\text{RC}}},$$

where t_{NC} is the total computation time with the non-convex ESS model with IPOPT and t_{RC} is the total computation time with the linear, convex ESS model. In Table 5.7, we also include the time it takes to solve (5.25) with the linear, convex ESS model with an academic Gurobi license [81] since that is a natural choice when solving a convex optimization problem without the complementarity constraint. From Table 5.7, we can see that using the RC ESS model results in finding an optimal solution approximately three times faster than with the NC ESS model when IPOPT is used, and can be increased to thirty times faster when Gurobi is used. Thus, using the proposed RC ESS

model results in a significant reduction in computation time when solving optimization problems on larger test systems.

Table 5.7: Computation time comparison for the relaxed convex, linear (RC) ESS model in (5.1) versus the non-convex (NC) ESS model with constraint (5.2). The speed-up factor is denoted SF. All times are reported in seconds.

Network	10 ESS			15 ESS			20 ESS		
(ESS Model, Solver)	Avg.	Total	SF	Avg.	Total	SF	Avg.	Total	SF
14-Bus (NC, IPOPT)	0.497	11.937							
14-Bus (RC, IPOPT)	0.196	4.709	2.535						
14-Bus (RC, Gurobi)	0.021	0.492	24.258						
57-Bus (NC, IPOPT)	1.428	34.267		1.577	37.839		1.598	38.350	
57-Bus (RC, IPOPT)	0.406	9.742	3.518	0.467	11.207	3.376	0.495	11.882	3.227
57 Bus (RC, Gurobi)	0.038	0.901	38.014	0.042	1.017	37.190	0.051	1.232	31.133
118-Bus (NC, IPOPT)	2.795	67.077		2.900	69.607		2.932	70.368	
118-Bus (RC, IPOPT)	0.814	19.534	3.434	0.844	20.263	3.435	0.905	21.726	3.239
118-Bus (RC, Gurobi)	0.075	1.799	37.292	0.089	2.143	32.473	0.095	2.275	30.935

In Fig. 5.8, the percent change in the cost function value with respect to solving DC OPF with the non-convex ESS model is given for the IEEE 14-bus, 57-bus, and 118-bus test systems and each ESS scenario at each iteration of the MPC. This highlights that the difference in optimality between the NC and RC ESS models, and between the solution obtained with IPOPT and Gurobi is negligible.

5.4 Relaxed Convex Grid-Connected Energy Storage Models in Distribution Settings

In this section, theoretical guarantees are provided for proper behavior of a grid-connected, convex ESS model in the second order cone (SOC) relaxation of the AC OPF problem in a distribution setting. Similar to the BTM and transmission settings, a penalty reformulation approach is used where the KKT conditions are leveraged in our theoretical analysis in order to omit the ESS complementarity constraint to maintain the convexity of the optimization problem. Compared to the transmission setting in Section 5.3 where the network is a mesh graph, the distribution setting is a radial network where the root node is the point of common coupling (PCC), or the distribution

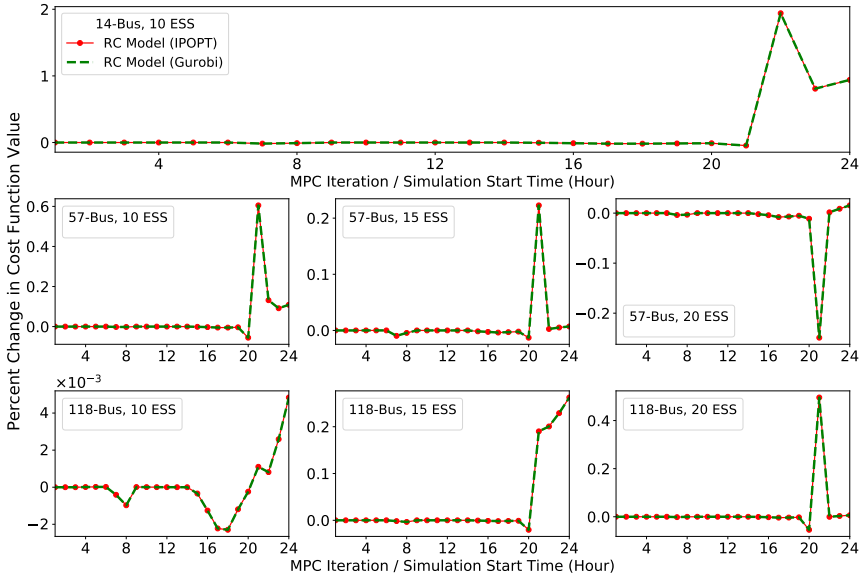

Figure 5.8: Percent change in cost function value for each iteration of the MPC-based DC OPF problem with a 12 hour prediction horizon. The percent change is with respect to the cost function value obtained when solving the MPC-based DC OPF with the NC ESS model. IEEE 14-bus test system (top row). IEEE 57-bus test system for each ESS scenario (middle row). IEEE 118-bus test system for each ESS scenario (bottom row).

substation, where the distribution network is connected to the transmission grid. An additional key difference is that the line capacity limits are not included when considering OPF in distribution settings, since a binding line capacity limit constraint would necessitate load shed downstream in the network. In distribution grids, it is also assumed there is an "infinite" generator at the root node, which represents power supplied to the distribution grid from the transmission grid.

Next, the SOC relaxation of the AC OPF problem with a relaxed convex ESS model is introduced. Then, the theoretical analysis is presented for guaranteeing non-simultaneous charging and discharging. Lastly, simulation results are provided to demonstrate proper charging and discharging behavior with the relaxed convex ESS model, and computation time savings with the relaxed convex ESS model compared to an equivalent mixed-integer ESS model. The relevant notation for this section is given in Table 5.4.

Table 5.8: Notation for SOCP relaxation of the AC OPF model.

	Sets
$b \in \mathcal{B}$	Set of buses
$b \in \mathcal{B}^+$	Set of buses excluding the origin bus $b = 0$
$l \in \mathcal{L}$	Set of lines $l = (b, d)$
$l \in \mathcal{L}_b$	Set of lines connected to bus b
$l \in \mathcal{L}_b^{\mathrm{d}}$	Set of lines with destination bus b
$l \in \mathcal{L}_b^{\mathrm{o}}$	Set of lines with origin bus b
$r \in \mathcal{R}$	Set of distributed energy resources
$r \in \mathcal{R}_b$	Set of distributed energy sources at bus b
$e \in \mathcal{E}$	Set of ESSs
$e \in \mathcal{E}_b$	Set of ESSs at bus b
$t \in \mathcal{T}$	Set of discrete time periods $\{1, 2, \ldots, H\}$
	Parameters
g_l	Conductance of line l
b_l	Susceptance of line l
$\underline{V}_b$	Minimum voltage at bus b (p.u.)
$\overline{V}_b$	Maximum voltage at bus b (p.u.)
P_r^{res}	Available generation from renewable energy source r (kW)
$\overline{P}_e$	Maximum charging/discharging power of ESS e (kW)
$\underline{E}_e$	Minimum ESS e state of charge (kWh)
$\overline{E}_e$	Maximum ESS e state of charge (kWh)
η_e^{ch}	Charging efficiency of ESS e
η_d^{dis}	Discharging efficiency of ESS e
$P_{b,t}^{\mathrm{L}}$	Real power demand at bus b (kW)
$Q_{b,t}^{\mathrm{L}}$	Reactive power demand at bus b (kVar)

	Variables
P_t^{G}	Real power dispatch of generator (kW)
Q_t^{G}	Reactive power dispatch of generator (kVar)
$P_{e,t}^{\mathrm{ch}}$	Power injected into ESS e (kW)
$P_{e,t}^{\mathrm{dis}}$	Power drawn from ESS e (kW)
$E_{e,t}$	State of charge of ESS e (kWh)
$P_{r,t}^{\mathrm{curt}}$	Renewable energy generation curtailment (kW)
$c_{b,t}$	SOCP variable for voltage squared term
$c_{l,t}$	SOCP variable for cosine term
$s_{l,t}$	SOCP variable for sine term
$p_{l(b),t}$	Real power flow on line l leaving bus b at time t (kW)
$q_{l(b),t}$	Reactive power flow on line l leaving bus b at time t (kVar)
$p_{l(d),t}$	Real power flow on line l leaving bus d at time t (kW)
$q_{l(d),t}$	Reactive power flow on line l leaving bus d at time t (kVar)

5.4.1 Second Order Cone Relaxation of AC OPF with Energy Storage

Next, we provide the mathematical formulation of the SOC relaxation of the AC OPF problem with distributed energy resources (renewable generation and ESSs) in a distribution setting. In a distribution network, it is necessary to model power losses and reactive power due to the high R/X ratio; thus a relaxation of AC OPF that captures nodal voltage, and real and reactive power must be used. The general non-convex AC OPF problem seeks to optimize real and reactive power in

a network subject to constraints on voltage magnitude and voltage angle at each bus [110]. The SOC relaxation, which was first proposed in [111, 112], results in a convex optimization problem where the non-convex quadratic terms in AC OPF are replaced with new variables $c_{b,t},\ c_{l,t},\ s_{l,t}$ and associated constraints:

$$c_{b,t} = v_{b,t}^2, \qquad \forall b \in \mathcal{B}, \forall t \in \mathcal{T}, \tag{5.38}$$

$$c_{l,t} = \cos(\theta_{b,t} - \theta_{d,t}) c_{b,t} c_{d,t}, \qquad \forall l \in \mathcal{L}, \forall t \in \mathcal{T}, \tag{5.39}$$

$$s_{l,t} = \sin(\theta_{b,t} - \theta_{d,t}) c_{b,t} c_{d,t}, \qquad \forall l \in \mathcal{L}, \forall t \in \mathcal{T}, \tag{5.40}$$

$$c_{l,t}^2 + s_{l,t}^2 \leq c_{b,t} c_{d,t}, \qquad \forall l \in \mathcal{L}, \forall t \in \mathcal{T}, \tag{5.41}$$

where $v_{b,t}$ is the voltage magnitude and $\theta_{b,t}$ is the voltage angle at each bus $b \in \mathcal{B}$. Let the optimization variables for all time t be collected in the vector $\underline{\mathbf{x}}_H = [\mathbf{x}_1\ \mathbf{x}_2\ \ldots\ \mathbf{x}_H]$ where $\mathbf{x}_t$ collects the optimization variables associated to time t. Then the overall SOC relaxation of the AC OPF problem with distributed energy resources is given by:

$$\min_{\underline{\mathbf{x}}_H} f^{\text{tot}}(\underline{\mathbf{x}}_H) \tag{5.42a}$$

$$\text{s.t. } \underline{V}_b^2 \leq c_{b,t} \leq \overline{V}_b^2, \qquad \forall b \in \mathcal{B}^+, \forall t \in \mathcal{T}, \tag{5.42b}$$

$$c_{l,t}^2 + s_{l,t}^2 \leq c_{b,t} c_{d,t}, \qquad \forall l \in \mathcal{L}, \forall t \in \mathcal{T}, \tag{5.42c}$$

$$E_{e,t+1} = E_{e,t} + \Delta t \eta_e^{\text{ch}} P_{e,t}^{\text{ch}} - \Delta t \tfrac{1}{\eta_e^{\text{dis}}} P_{e,t}^{\text{dis}}, \qquad \forall e \in \mathcal{E}, \forall t \in \mathcal{T}, \tag{5.42d}$$

$$\underline{E}_e \leq E_{e,t+1} \leq \overline{E}_e, \qquad \forall e \in \mathcal{E}, \forall t \in \mathcal{T}, \tag{5.42e}$$

$$0 \leq P_{e,t}^{\text{ch}} \leq \overline{P}_e, \qquad \forall e \in \mathcal{E}, \forall t \in \mathcal{T}, \tag{5.42f}$$

$$0 \leq P_{e,t}^{\text{dis}} \leq \overline{P}_e, \qquad \forall e \in \mathcal{E}, \forall t \in \mathcal{T}, \tag{5.42g}$$

$$0 \leq P_{r,t}^{\text{curt}} \leq P_{r,t}^{\text{res}}, \qquad \forall r \in \mathcal{R}, \forall t \in \mathcal{T}, \tag{5.42h}$$

$$p_{l(b),t} = c_{b,t} g_l - c_{l,t} g_l - s_{l,t} b_l, \qquad \forall l \in \mathcal{L}, \forall t \in \mathcal{T}, \tag{5.42i}$$

$$p_{l(d),t} = c_{b,t} g_l - c_{l,t} g_l + s_{l,t} b_l, \qquad \forall l \in \mathcal{L}, \forall t \in \mathcal{T}, \tag{5.42j}$$

$$q_{l(b),t} = -c_{b,t} b_l + c_{l,t} b_l - s_{l,t} g_l, \qquad \forall l \in \mathcal{L}, \forall t \in \mathcal{T}, \tag{5.42k}$$

$$q_{l(d),t} = -c_{b,t} b_l + c_{l,t} b_l + s_{l,t} g_l, \qquad \forall l \in \mathcal{L}, \forall t \in \mathcal{T}, \tag{5.42l}$$

$$-P_t^{\mathrm{G}} + \sum_{l \in \mathcal{L}_b^{\mathrm{o}}} p_{l(b),t} = 0, \qquad \forall b \notin \mathcal{B}^+, \forall t \in \mathcal{T}, \tag{5.42m}$$

$$-Q_t^{\mathrm{G}} + \sum_{l \in \mathcal{L}_b^{\mathrm{o}}} q_{l(b),t} = 0, \qquad \forall b \notin \mathcal{B}^+, \forall t \in \mathcal{T}, \tag{5.42n}$$

$$P_{b,t}^{\mathrm{L}} + \sum_{l \in \mathcal{L}_b^{\mathrm{o}}} p_{l(b),t} + \sum_{l \in \mathcal{L}_b^{\mathrm{d}}} p_{l(d),t} + \sum_{e \in \mathcal{E}_b} (P_{e,t}^{\mathrm{ch}} - P_{e,t}^{\mathrm{dis}}) - \sum_{r \in \mathcal{R}_b} (P_{r,t}^{\mathrm{res}} - P_{r,t}^{\mathrm{curt}}) = 0, \qquad \forall b \in \mathcal{B}^+, \forall t \in \mathcal{T}, \tag{5.42o}$$

$$Q_{b,t}^{\mathrm{L}} + \sum_{l \in \mathcal{L}_b^{\mathrm{o}}} q_{l(b),t} + \sum_{l \in \mathcal{L}_b^{\mathrm{d}}} q_{l(d),t} = 0, \qquad \forall b \in \mathcal{B}^+, \forall t \in \mathcal{T}. \tag{5.42p}$$

The objective function in (5.42a) is assumed to be differentiable and convex, where the exact objective function is not specified to preserve generality of our results. The node voltage limits are enforced in (5.42b). The second order cone constraint is given by (5.42c). The relaxed convex ESS model is included in (5.42d)-(5.42g). Curtailment of distributed energy resources is enforced in (5.42h). The real and reactive power flow constraints are given in (5.42i)-(5.42l). The real and reactive power balance at the root bus is given by (5.42m) and (5.42n), respectively. The real and reactive power balance for buses $b \in \mathcal{B}^+$ is given by (5.42o) and (5.42p). The overall SOC relaxation of AC OPF optimization model with distributed energy sources and ESSs in (5.42) will be the focus of our analysis for ensuring an optimal solution will satisfy proper ESS charging and discharging behavior in (5.2).

5.4.2 Theoretical Guarantees for Relaxed Energy Storage System Models in the SOC Relaxation of AC OPF in Distribution

For our theoretical analysis, the KKT conditions are again leveraged since the SOC relaxation of AC OPF in (5.42) is a convex SOC program (SOCP). For use in the theoretical analysis, we introduce some notation for the Lagrange multipliers associated with the equality and inequality

constraints in (5.42) (written in standard form):

$$\underline{\lambda}^{\mathrm{v}}_{b,t} : \underline{V}_b^2 - c_{b,t} \leq 0, \qquad \forall b \in \mathcal{B}^+, \forall t \in \mathcal{T}, \quad (5.43a)$$

$$\overline{\lambda}^{\mathrm{v}}_{b,t} : c_{b,t} - \overline{V}_b^2 \leq 0, \qquad \forall b \in \mathcal{B}^+, \forall t \in \mathcal{T}, \quad (5.43b)$$

$$\lambda^{\mathrm{socp}}_{l,t} : c_{l,t}^2 + s_{l,t}^2 - c_{b,t}c_{d,t} \leq 0, \qquad \forall l \in \mathcal{L}, \forall t \in \mathcal{T}, \quad (5.43c)$$

$$\underline{\lambda}^{\mathrm{ch}}_{e,t} : \ - P^{\mathrm{ch}}_{e,t} \leq 0, \qquad \forall e \in \mathcal{E}, \forall t \in \mathcal{T}, \quad (5.43d)$$

$$\overline{\lambda}^{\mathrm{ch}}_{e,t} : P^{\mathrm{ch}}_{e,t} - \overline{P}_e \leq 0, \qquad \forall e \in \mathcal{E}, \forall t \in \mathcal{T}, \quad (5.43e)$$

$$\underline{\lambda}^{\mathrm{dis}}_{e,t} : \ - P^{\mathrm{dis}}_{e,t} \leq 0, \qquad \forall e \in \mathcal{E}, \forall t \in \mathcal{T}, \quad (5.43f)$$

$$\overline{\lambda}^{\mathrm{dis}}_{e,t} : P^{\mathrm{dis}}_{e,t} - \overline{P}_e \leq 0, \qquad \forall e \in \mathcal{E}, \forall t \in \mathcal{T}, \quad (5.43g)$$

$$\underline{\lambda}^{\mathrm{soc}}_{e,t} : \underline{E}_e - E_{e,0} + \Delta t \sum_{n=1}^{t-1} \left(\tfrac{1}{\eta^{\mathrm{dis}}_e} P^{\mathrm{dis}}_{e,t} - \eta^{\mathrm{ch}}_e P^{\mathrm{ch}}_{e,t} \right) \leq 0, \qquad \forall e \in \mathcal{E}, \forall t \in \mathcal{T}, \quad (5.43h)$$

$$\overline{\lambda}^{\mathrm{soc}}_{e,t} : E_{e,0} + \Delta t \sum_{n=1}^{t-1} \left(\eta^{\mathrm{ch}}_e P^{\mathrm{ch}}_{e,t} - \tfrac{1}{\eta^{\mathrm{dis}}_e} P^{\mathrm{dis}}_{e,t} \right) - \overline{E}_e \leq 0, \qquad \forall e \in \mathcal{E}, \forall t \in \mathcal{T}, \quad (5.43i)$$

$$\underline{\lambda}^{\mathrm{res}}_{r,t} : \ - P^{\mathrm{c}}_{r,t} \leq 0, \qquad \forall r \in \mathcal{R}, \forall t \in \mathcal{T}, \quad (5.43j)$$

$$\overline{\lambda}^{\mathrm{res}}_{r,t} : P^{\mathrm{c}}_{r,t} - P^{\mathrm{res}}_{r,t} \leq 0, \qquad \forall r \in \mathcal{R}, \forall t \in \mathcal{T}, \quad (5.43k)$$

$$\mu^{\mathrm{P}}_{0,t} : \ - P^{\mathrm{G}}_t + \sum_{l \in \mathcal{L}^{\mathrm{o}}_b} (c_{b,t} g_l - c_{l,t} g_l - s_{l,t} b_l) = 0, \qquad \forall t \in \mathcal{T}, \quad (5.43l)$$

$$\mu^{\mathrm{Q}}_{0,t} : \ - Q^{\mathrm{G}}_t + \sum_{l \in \mathcal{L}^{\mathrm{o}}_b} (-c_{b,t} b_l + c_{l,t} b_l - s_{l,t} g_l) = 0, \qquad \forall t \in \mathcal{T}, \quad (5.43m)$$

$$\begin{aligned} \mu^{\mathrm{P}}_{b,t} : P^{\mathrm{L}}_{b,t} &+ \sum_{l \in \mathcal{L}^{\mathrm{o}}_b} (c_{b,t} g_l - c_{l,t} g_l - s_{l,t} b_l) + \sum_{l \in \mathcal{L}^{\mathrm{d}}_b} (c_{b,t} g_l - c_{l,t} g_l + s_{l,t} b_l) \\ &+ \sum_{e \in \mathcal{E}_b} (P^{\mathrm{ch}}_{e,t} - P^{\mathrm{dis}}_{e,t}) - \sum_{r \in \mathcal{R}_b} (P^{\mathrm{res}}_{r,t} - P^{\mathrm{curt}}_{r,t}) = 0, \qquad \forall b \in \mathcal{B}^+, \forall t \in \mathcal{T}, \quad (5.43n) \end{aligned}$$

$$\mu^{\mathrm{Q}}_{b,t} : Q^{\mathrm{L}}_{b,t} + \sum_{l \in \mathcal{L}^{\mathrm{o}}_b} (-c_{b,t} b_l + c_{l,t} b_l - s_{l,t} g_l) + \sum_{l \in \mathcal{L}^{\mathrm{d}}_b} (-c_{b,t} b_l + c_{l,t} b_l + s_{l,t} g_l) = 0, \quad \forall b \in \mathcal{B}^+, \forall t \in \mathcal{T}. \quad (5.43o)$$

Notice that, even with the addition of modeling nodal voltage magnitude limits and reactive power, the ESS variables $P^{\mathrm{dis}}_{e,t}$ and $P^{\mathrm{ch}}_{e,t}$ only show up in the real power balance, as in the BTM and transmission setting. Let $\mathcal{B}_r$ denote the set of buses with distributed energy sources and let $\mathcal{B}_e$

denote the set of buses with an ESS. Then, the KKT stationarity conditions of interest are:

$$-\underline{\lambda}^{\text{res}}_{r,t} + \overline{\lambda}^{\text{res}}_{r,t} + \mu^{\text{P}}_{b,t} = 0, \qquad \forall b \in \mathcal{B}_r, \forall t \in \mathcal{T}, \tag{5.44a}$$

$$\partial_{P^{\text{ch}}_{e,t}} f_{\text{tot}}(\tilde{\underline{\mathbf{x}}}_H) - \underline{\lambda}^{\text{ch}}_{e,t} + \overline{\lambda}^{\text{ch}}_{e,t} + \eta^{\text{ch}}_e \Delta t \sum_{n=t}^{H} (\overline{\lambda}^{\text{soc}}_{e,n} - \underline{\lambda}^{\text{soc}}_{e,n}) + \mu^{\text{P}}_{b,t} = 0, \qquad \forall b \in \mathcal{B}_e, \forall t \in \mathcal{T}, \tag{5.44b}$$

$$\partial_{P^{\text{dis}}_{e,t}} f_{\text{tot}}(\tilde{\underline{\mathbf{x}}}_H) - \underline{\lambda}^{\text{dis}}_{e,t} + \overline{\lambda}^{\text{dis}}_{e,t} + \tfrac{1}{\eta^{\text{dis}}_e} \Delta t \sum_{n=t}^{H} (\underline{\lambda}^{\text{soc}}_{e,n} - \overline{\lambda}^{\text{soc}}_{e,n}) - \mu^{\text{P}}_{b,t} = 0, \qquad \forall b \in \mathcal{B}_e, \forall t \in \mathcal{T}. \tag{5.44c}$$

Thus, our following theoretical result is intuitive from our previous analysis for the BTM and transmission setting. For the following discussion, let the vector $\tilde{\underline{\mathbf{x}}}_H$ denote an optimal solution to (5.42).

Proposition 5.4 Assume the objective function $f^{\text{tot}}(\underline{\mathbf{x}}_H)$ is differentiable and convex. Further assume that $\partial_{P^{\text{ch}}_{e,t}} f^{\text{tot}}(\tilde{\underline{\mathbf{x}}}_H) \geq 0$, $\partial_{P^{\text{dis}}_{e,t}} f^{\text{tot}}(\tilde{\underline{\mathbf{x}}}_H) \geq 0$, and $(\partial_{P^{\text{ch}}_{e,t}} f^{\text{tot}}(\tilde{\underline{\mathbf{x}}}_H) + \partial_{P^{\text{dis}}_{e,t}} f^{\text{tot}}(\tilde{\underline{\mathbf{x}}}_H)) > 0$ for all $e \in \mathcal{E}$ and $t \in \mathcal{T}$. A solution satisfies $P^{\text{ch}}_{e,t} \cdot P^{\text{dis}}_{e,t} = 0$ at time $t \in \mathcal{T}$ for ESS $e \in \mathcal{E}_b$ if at least one of the following conditions is satisfied at bus $b \in \mathcal{B}$:

C1) $\mu^{\text{P}}_{b,t} \geq 0$,

C2) $0 \leq \tilde{P}^{\text{c}}_{r,t} < P^{\text{res}}_{r,t}$ for some $r \in \mathcal{R}_b$,

C3) $\sum_{n=t}^{H} (\overline{\lambda}^{\text{soc}}_{e,n} - \underline{\lambda}^{\text{soc}}_{e,n}) \leq 0$.

Proof. Let the assumptions in the proposition statement hold. For each of the three conditions given in Proposition 5.4, we will show that an optimal solution to (5.42) will satisfy (5.2). We begin by assuming that Condition C1 is true, i.e., $\mu^{\text{P}}_{b,t} \geq 0$ at time $t \in \mathcal{T}$ at bus $b \in \mathcal{B}$. Also assume that ESS $e \in \mathcal{E}_b$ is simultaneously charging and discharging at time t. Solving for $\mathcal{I} = \sum_{n=t}^{H} (\overline{\lambda}^{\text{soc}}_{e,n} - \underline{\lambda}^{\text{soc}}_{e,n})$ in (5.44b), and plugging $-\mathcal{I}$ into (5.44c), we obtain:

$$\partial_{P^{\text{dis}}_{e,t}} f^{\text{tot}}(\tilde{\underline{\mathbf{x}}}_H) + \tfrac{1}{\eta^{\text{dis}}_e \eta^{\text{ch}}_e} \partial_{P^{\text{ch}}_{e,t}} f^{\text{tot}}(\tilde{\underline{\mathbf{x}}}_H) + \overline{\lambda}^{\text{dis}}_{e,t} + \tfrac{1}{\eta^{\text{dis}}_e \eta^{\text{ch}}_e} \overline{\lambda}^{\text{ch}}_{e,t} + (\tfrac{1}{\eta^{\text{dis}}_e \eta^{\text{ch}}_e} - 1) \mu^{\text{P}}_{b,t} = 0, \tag{5.45}$$

since $\underline{\lambda}^{\text{ch}}_{e,t} = \underline{\lambda}^{\text{dis}}_{e,t} = 0$ by our assumption that ESS e is simultaneously charging and discharging. Then, the first four terms in (5.45) are strictly greater than 0, by our assumptions on the objection function $f^{\text{tot}}(\underline{\mathbf{x}}_H)$ and the KKT dual feasibility condition. Also, the quantity $(\frac{1}{\eta^{\text{dis}}_e \eta^{\text{ch}}_e} - 1) > 0$ by

our assumptions on the ESS model efficiency parameters. Thus, we obtain a contradiction since (5.45) cannot equal zero when Condition C1 is true. Thus, if an optimal solution to (5.42) satisfies Condition C1, then the optimal solution at time t will satisfy (5.2) for ESS e at bus b.

Next, assume Condition C2 is true, i.e., the optimal solution to (5.42) is such that $0 \leq \tilde{P}^{\mathrm{c}}_{r,t} < P^{\mathrm{res}}_{r,t}$ at time $t \in \mathcal{T}$ for some $r \in \mathcal{R}_b$, that is located with ESS $e \in \mathcal{E}_b$ at bus $b \in \mathcal{B}$. By the KKT complementarity slackness condition, we obtain $\overline{\lambda}^{\mathrm{res}}_{r,t} = 0$. Then, by (5.44a) we have $\mu^{\mathrm{P}}_{b,t} = \underline{\lambda}^{\mathrm{res}}_{r,t} \geq 0$ because of the KKT dual feasibility condition. Therefore, from our analysis for Condition C1 when $\mu^{\mathrm{P}}_{b,t} \geq 0$, ESS e will satisfy the complementarity constraint in (5.2) at time t.

Lastly, assume Condition C3 is true, i.e., $\sum_{n=t}^{H}(\overline{\lambda}^{\mathrm{soc}}_{e,n} - \underline{\lambda}^{\mathrm{soc}}_{e,n}) \leq 0$ at time $t \in \mathcal{T}$ for ESS $e \in \mathcal{E}_b$.But, ESS e is simultaneously charging and discharging at time t, i.e., $0 < \tilde{P}^{\mathrm{ch}}_{e,t} \leq \overline{P}_e$ and $0 < \tilde{P}^{\mathrm{dis}}_{e,t} \leq \overline{P}_e$. By the KKT complementary slackness condition, we obtain that $\underline{\lambda}^{\mathrm{ch}}_{e,t} = \underline{\lambda}^{\mathrm{dis}}_{e,t} = 0$. Then, adding (5.44b) and (5.44c) together, we obtain:

$$\partial_{P^{\mathrm{ch}}_{e,t}} f^{\mathrm{tot}}(\tilde{\underline{\mathbf{x}}}_H) + \partial_{P^{\mathrm{dis}}_{e,t}} f^{\mathrm{tot}}(\tilde{\underline{\mathbf{x}}}_H) + \overline{\lambda}^{\mathrm{ch}}_{e,t} + \overline{\lambda}^{\mathrm{dis}}_{e,t} + \Delta t\left(\eta^{\mathrm{ch}}_e - \frac{1}{\eta^{\mathrm{dis}}_e}\right)\sum_{n=t}^{H}(\overline{\lambda}^{\mathrm{soc}}_{e,n} - \underline{\lambda}^{\mathrm{soc}}_{e,n}) = 0. \tag{5.46}$$

By the assumption that $\partial_{P^{\mathrm{ch}}_{e,t}} f^{\mathrm{tot}}(\tilde{\underline{\mathbf{x}}}_H) \geq 0$, $\partial_{P^{\mathrm{dis}}_{e,t}} f^{\mathrm{tot}}(\tilde{\underline{\mathbf{x}}}_H) \geq 0$, $(\partial_{P^{\mathrm{ch}}_{e,t}} f^{\mathrm{tot}}(\tilde{\underline{\mathbf{x}}}_H) + \partial_{P^{\mathrm{dis}}_{e,t}} f^{\mathrm{tot}}(\tilde{\underline{\mathbf{x}}}_H)) > 0$, and $0 < \eta^{\mathrm{ch}}_e, \eta^{\mathrm{dis}}_e < 1$, together with $\overline{\lambda}^{\mathrm{ch}}_{e,t} \geq 0$ and $\overline{\lambda}^{\mathrm{dis}}_{e,t} \geq 0$ by the KKT dual feasibility condition, the sum of the first four terms in (5.46) is positive. Since $(\eta^{\mathrm{ch}}_e - \frac{1}{\eta^{\mathrm{dis}}_e}) < 0$ and our assumption that $\sum_{n=t}^{H}(\overline{\lambda}^{\mathrm{soc}}_{e,n} - \underline{\lambda}^{\mathrm{soc}}_{e,n}) \leq 0$, we obtain a contradiction since the left-hand side of (5.46) cannot equal zero. Thus, if Condition C3 is satisfied, an optimal solution to (5.42) will satisfy (5.2) at time t for ESS e. □

5.4.3 Case Study: Proper Energy Storage System Model Behavior in Distribution

To demonstrate the optimal charging and discharging behavior of the ESS model, simulation results are provided on the IEEE 18-bus test feeder [104] for the SOC relaxed OPF model in (5.42). The 18-bus test feeder is modified to include distributed renewable sources, i.e., PV sources, and ESSs at arbitrary nodes, as shown in Table 5.9. Simulation results are provided for (5.42) when

$|\mathcal{E}|$ is 5, 10, and 15. The ESS charging efficiency η_e^{ch} is randomly chosen from $[0.92, 0.93, \ldots, 0.97]$, and the ESS capacity $\overline{E}_e$ is randomly chosen from $[40, 45, \ldots, 100]$ for each ESS $e \in \mathcal{E}$. The discharging efficiency for each ESS is $\eta_e^{\text{dis}} = \eta_e^{\text{ch}}$. The maximum charging/discharging power P_e is chosen to be 60% of the ESS capacity $\overline{E}_e$. The network load data is obtained from PJM's publicly available database [105] and the solar data is obtained from NREL's Solar Power Data for Integration Studies [106]. The model in (5.42) is simulated for 24 hours ($H = 24$) with 1 hour time intervals ($\Delta t = 1$). The model in (5.42) is implemented in Python using the Pyomo [107,108] optimization modeling language, using the MATPOWER data parser and other select functions from EGRET [80], and solved using an academic Gurobi 8.1.1 license [81]. The simulations in this work were performed on a computer with a 3.4 GHz AMD Ryzen 5 processor with 16 GB of RAM. The objective function used in this study is:

$$f^{\text{tot}}(\underline{\mathbf{x}}_H) = \sum_{t \in \mathcal{T}} \left(Q_t^{\text{G}} + \sum_{e \in \mathcal{E}} 0.1 P_{e,t}^{\text{dis}} \right), \tag{5.47}$$

which satisfies the assumptions of the model formulation in Proposition 5.4.

Table 5.9: Bus locations for distributed resources, i.e., ESSs and PV sources, in the IEEE 18-bus test feeder.

Distributed Resource	Bus Locations
PV	2-5, 7-9, 12-14
ESS (5)	1, 3, 11, 12, 17
ESS (10)	2, 3, 5, 7, 10, 12-14, 16, 18
ESS (15)	1-5, 7-16

The numerical complementarity gap results for each simulation with varying numbers of ESSs in the distribution feeder are shown in Fig. 5.9, where the numerical complementarity gap for each ESS $e \in \mathcal{E}$ is defined as $\tilde{P}_{e,t}^{\text{ch}} \cdot \tilde{P}_{e,t}^{\text{dis}}$. From Fig. 5.9, our proposed penalty approach achieves a numerical complementarity gap on the order of 10^{-8} and 10^{-9}, showing the complementarity constraint (5.2) is numerically satisfied.

Lastly, simulations results are provided to demonstrate the computation time savings achieved with the relaxed convex ESS model in (5.42) compared to when the following mixed-integer ESS

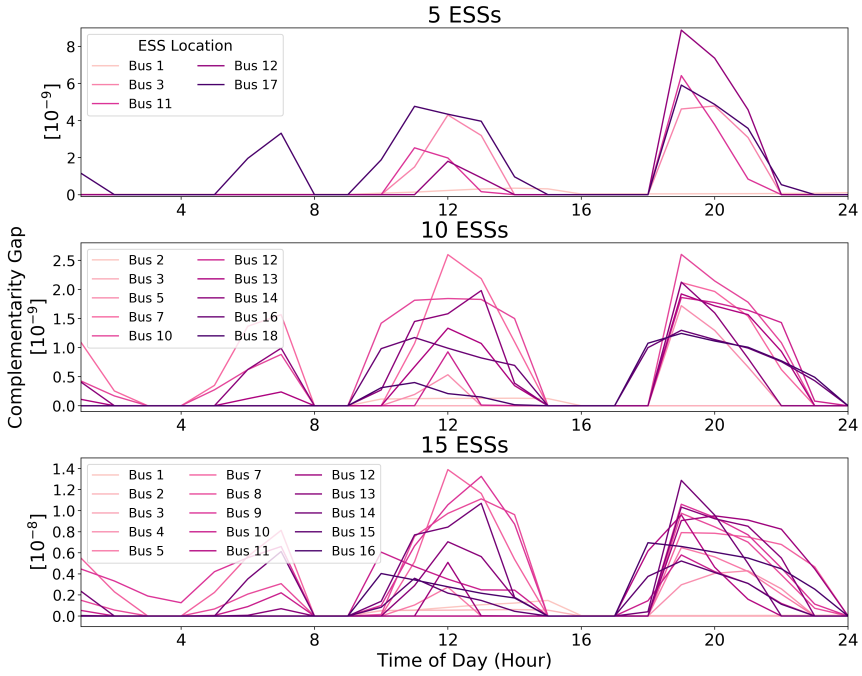

Figure 5.9: Numerical complementarity gap for distributed ESSs in the IEEE 18-bus test feeder. Top: Simulation with $|\mathcal{E}| = 5$. Middle: Simulation with $|\mathcal{E}| = 10$. Bottom: Simulation with $|\mathcal{E}| = 15$.

model is used:

$$E_{e,t+1} = E_{e,t} + \Delta t \eta_e^{\text{ch}} P_{e,t}^{\text{ch}} b_{e,t} - \Delta t \tfrac{1}{\eta_e^{\text{dis}}} P_{e,t}^{\text{dis}} (1 - b_{e,t}), \qquad \forall e \in \mathcal{E}, \forall t \in \mathcal{T}, \tag{5.48a}$$

$$\underline{E}_e \leq E_{e,t+1} \leq \overline{E}_e, \qquad \forall e \in \mathcal{E}, \forall t \in \mathcal{T}, \tag{5.48b}$$

$$0 \leq P_{e,t}^{\text{ch}} \leq \overline{P}_e, \qquad \forall e \in \mathcal{E}, \forall t \in \mathcal{T}, \tag{5.48c}$$

$$0 \leq P_{e,t}^{\text{dis}} \leq \overline{P}_e, \qquad \forall e \in \mathcal{E}, \forall t \in \mathcal{T}, \tag{5.48d}$$

$$b_{e,t} \in \{0, 1\}, \qquad \forall e \in \mathcal{E}, \forall t \in \mathcal{T}, \tag{5.48e}$$

where $b_{e,t}$ is a binary variable introduced into the ESS model to enforce the omitted complementarity constraint (5.2). When the binary ESS model in (5.48) replaces the relaxed convex ESS model in (5.42d)-(5.42g), the overall optimization problem in (5.42) becomes a mixed-integer SOCP (MISOCP), which is solved using Gurobi. To measure the computation time savings achieved by using

the relaxed convex ESS model, we define the Speed-Up Factor metric as:

$$\text{Speed-Up Factor } = \frac{t^{\text{MISOCP}}}{t^{\text{SOCP}}},$$

where t^{MISOCP} is the total computation time to solve the MISOCP problem and t^{SOCP} is the total computation time to solve (5.42). In Table 5.10, our numerical experiments show significant computation time savings when the relaxed convex ESS model is used.

Table 5.10: Computation time savings for the relaxed convex ESS model compared to a mixed-integer ESS model in a distribution setting.

Number of ESSs	Speed-Up Factor, $\frac{t^{\text{MISOCP}}}{t^{\text{SOCP}}}$
5	8.442
10	16.506
15	16.353

5.5 Discussion and Conclusions

This chapter provides a convex relaxation for a grid-connected ESS model using the penalty reformulation approach in a multi-period BTM EMS setting, in a DC OPF problem in transmission, and an SOCP relaxation of AC OPF in distribution. We provide the conditions under which the relaxed convex ESS model in each optimization model ensures a solution with an ESS simultaneously charging and discharging is suboptimal. In the EMS setting, our theoretical guarantees include EMS models that capture net metering, FiTs, demand charges, TOU rates, and flexible load scheduling. We leverage the KKT conditions for our analysis, with assumptions on the properties that the optimization objective function must satisfy, to provide guarantees for situations where a solution with simultaneous ESS charging and discharging is suboptimal. Thus, ESS models with non-convex complementarity constraints to prevent simultaneous charging and discharging are unnecessary when the conditions presented in this chapter are satisfied for their respective grid settings. Numerical case study results were provided to show the proper ESS charging and discharging behavior when the conditions for the relaxation to hold are satisfied, as well as when

the necessary conditions to guarantee non-simultaneous ESS charging and discharging are not satisfied. In the transmission and distribution setting, we provide additional simulation results on multiple IEEE test systems showing that the computation time is reduced when using relaxed ESS model compared to a non-convex ESS model, while still ensuring that the correct non-simultaneous charging and discharging is observed.

Chapter 6

Conclusion and Future Directions

In this thesis, we presented stochastic optimization methods for integrating renewable energy into the power grid in both BTM settings with distributed renewable energy resources and transmission grid settings with large wind farms. Integrating renewable energy is challenging due to the intermittent, variable, and non-dispatchable characteristics of renewable energy generation. To reduce the impact of these challenges on the grid, ESSs are often coupled with renewable energy sources in many active areas of power grid optimization research. This thesis also presented theoretical analysis for a grid-connected convex ESS model that is guaranteed to produce a physically realizable control policy when included in optimization models from BTM to transmission settings.

To aid in BTM renewable energy integration, two chance constrained MPC-based optimization models were proposed for a HEMS algorithm that coordinates appliances, customer preferences, and BTM controllable resources such as generation from rooftop PV panels and an HBS. The first chance constrained MPC-based HEMS responded to utility-requested DR events, and chance constraints were incorporated into the optimization problem to ensure the DR request and home indoor air temperature preferences are satisfied with a high probability given uncertainty in both the solar and weather forecasts. In the second chance constrained MPC-based HEMS study, the performance of the HEMS algorithm was compared across multiple scenarios, each with different sets of controllable BTM resources, under a constant electricity price and a TOU electricity price. Similarly, chance constraints ensured the indoor thermal comfort was maintained with high probability given uncertainty in the weather forecast. When comparing the performance results

with TOU electricity prices to constant electricity prices, the HBS usage and the daily load factor increased in most scenarios with a TOU electricity price. Additionally, with TOU prices, the HEMS was able to optimally coordinate the available controllable resources in each scenario to decrease the total electricity cost for the consumers. Future work in chance constrained HEMS models includes incorporating other flexible loads, such as a dishwasher and/or water heater, into the proposed optimization framework. This may allow for further load flexibility and help with reducing HBS cycling and daily load factor. Further work on stochastic MPC-based HEMS algorithms includes incorporating other stochastic parameters with non-Gaussian distributions, such as home occupancy schedules and EV arrival and departure times, which can be incorporated into the optimization model using existing techniques in the literature [36]. A future research direction also includes determining optimal time-varying residential electricity rates that produce optimal EMS behavior, ensuring favorable HEMS performance from both customer and utility perspectives.

For integrating power generation from large wind farms at the transmission level, we proposed a two-stage stochastic optimal power flow problem with flexible line ratings to address uncertainty in wind power forecasts, alleviate line congestion, and minimize wind power curtailment. An SAA of a joint chance constraint is used to limit the probability of continuous line rating violations across probable wind scenario realizations, all times in the simulation, and all lines in the network. Simulation results on the RTS GMLC test system demonstrated that flexible line limits reduce the wind power curtailment in a congested area of the network with a large amount of distributed renewable and wind sources. By allowing violations of the nominal continuous line rating, wind power that would have been otherwise curtailed was exported to other areas of the network to satisfy the power demand. Future work includes using a Bender's decomposition algorithm or Generalized Disjunctive Programming (GDP) to consider a larger number of wind scenarios and compare our approach to optimal transmission switching (OTS). Additionally, incorporating ESSs into the test system may further help mitigate congestion in the network and minimize wind power curtailment. Excess available wind power could be stored in the ESS for use during periods of low renewable energy generation.

Lastly, this dissertation proposed a penalty reformulation approach for a relaxed convex grid-connected ESS model for use in power system optimization models. For a BTM EMS setting, DC OPF in transmission setting, and SOC relaxation of AC OPF in a distribution setting, we provided conditions under which the non-convex complementarity constraint can be omitted from an optimization model while ensuring feasible solutions with simultaneous charging and discharging are suboptimal. In the EMS setting, the proper ESS model behavior guarantees were extended to situations with net metering, FiTs, demand charges, TOU rates, and flexible load scheduling. Numerical case study results were provided for both the BTM and transmission setting to highlight proper ESS model behavior when the conditions for the convex relaxation to hold were satisfied, as well as when the necessary conditions to guarantee non-simultaneous ESS charging and discharging were not satisfied. In the DC OPF setting, we also provided simulation results on multiple IEEE test systems showing that the computation time was reduced when using relaxed ESS model compared to the nonlinear ESS model with the complementarity constraint, while still ensuring that the correct non-simultaneous charging and discharging was observed. In the SOC relaxed AC OPF setting, simulation results demonstrated the computation time savings with the relaxed convex ESS model compared to a mixed-integer linear ESS model where binary variables are used to ensure non-simultaneous charging and discharging. Future work includes ensuring non-simultaneous charging and discharging in stochastic ESS models and under different stochastic elements in both BTM and transmission settings. In the BTM EMS setting, potential future directions include extending our theoretical guarantees to transactive energy and peer-to-peer energy trading models. Additionally, future work could include studying relaxing complementarity conditions for other device models with binary modes of operation that arise in either BTM or transmission settings.

Bibliography

[1] R. Bowers. (2019, Feb) Updated renewable portfolio standards will lead to more renewable elecctricity generation. U.S. Energy Information Administration. Last accessed: August 10, 2020. [Online]. Available: https://www.eia.gov/todayinenergy/detail.php?id=38492#

[2] National Conference of State Legislatures. (2020, April) State renewable portfolio standards and goals. Last accessed: August 10, 2020. [Online]. Available: https://www.ncsl.org/research/energy/renewable-portfolio-standards.aspx

[3] S. Koebrich, T. Bowen, and A. Sharpe, "2018 renewable energy data book." [Online]. Available: https://www.nrel.gov/docs/fy20osti/75284.pdf

[4] California Independent System Operator (CAISO). (2016) What the duck curve tells us about managing a green grid. Last accessed: August 10, 2020. [Online]. Available: https://www.caiso.com/Documents/FlexibleResourcesHelpRenewables_FastFacts

[5] U.S. Department of Energy, Office of Energy Efficiency and Renewable Energy, "Buildings Energy Data Book," 2012.

[6] X. Jin, K. Baker, D. Christensen, and S. Isley, "Foresee: A user-centric home energy management system for energy efficiency and demand response," Applied Energy, vol. 205, pp. 1583 – 1595, 2017.

[7] B. Zhou, W. Li, K. W. Chan, Y. Cao, Y. Kuang, X. Liu, and X. Wang, "Smart home energy management systems: Concept, configurations, and scheduling strategies," Renewable and Sustainable Energy Reviews, vol. 61, pp. 30–40, 2016.

[8] WINDExchange: U.S. Installed and Potential Wind Power Capacity and Generation. U.S. Department of Energy's Wind Energy Technologies Office. Last accessed: August 2020. [Online]. Available: https://windexchange.energy.gov/maps-data/321

[9] S. Fink, C. Mudd, K. Porter, and B. Morgenstern, "Wind Energy Curtailment Case Studies: May 2008 - May 2009," National Renewable Energy Laboratory, NREL/SR-550-46716, Oct 2009. [Online]. Available: https://www.nrel.gov/docs/fy10osti/46716.pdf

[10] L. Bird, J. Cochran, and X. Wang, "Wind and Solar Energy Curtailment: Experience and Practices in the United States," National Renewable Energy Laboratory, NREL/TP-6A20-60983, March 2014. [Online]. Available: https://www.nrel.gov/docs/fy14osti/60983.pdf

[11] A. Castillo and D. F. Gayme, "Grid-scale energy storage applications in renewable energy integration: A survey," Energy Conversion and Management, vol. 87, pp. 885 – 894, 2014.

[12] A. A. Akhil, G. Huff, A. B. Currier, B. C. Kaun, D. M. Rastler, S. B. Chen, A. L. Cotter, D. T. Bradshaw, and W. D. Gauntlett, "DOE/EPRI 2013 electricity storage handbook in collaboration with NRECA." [Online]. Available: http://www.sandia.gov/ess/publications/SAND2013-5131.pdf

[13] F. Garrett, J. Mandel, J. Morris, and H. Touati, "The economics of battery energy storage: How multi-use, customer-sited batteries deliver the most services and value to customers and the grid." Rocky Mountain Institute, 2015.

[14] K. Divya and J. Østergaard, "Battery energy storage technology for power systems-an overview," Electric Power Systems Research, vol. 79, no. 4, pp. 511–520, 2009.

[15] D. Wu, C. Jin, P. Balducci, and M. Kintner-Meyer, "An energy storage assessment: Using optimal control strategies to capture multiple services," in 2015 IEEE Power and Energy Society General Meeting, July 2015.

[16] D. M. Rosewater, D. A. Copp, T. A. Nguyen, R. H. Byrne, and S. Santoso, "Battery energy storage models for optimal control," IEEE Access, vol. 7, pp. 178 357–178 391, 2019.

[17] K. Garifi, K. Baker, D. Christensen, and B. Touri, "Stochastic model predictive control for demand response in a home energy management system," in 2018 IEEE Power and Energy Society General Meeting, 2018.

[18] K. Garifi, K. Baker, B. Touri, and D. Christensen, "Stochastic home energy management systems with varying controllable resources," in 2019 IEEE Power and Energy Society General Meeting, 2019.

[19] K. Garifi and K. Baker, "Considering integer chance constraints for enforcing flexible line flow ratings," in 2020 American Control Conference (ACC), 2020, pp. 3134–3139.

[20] K. Garifi, K. Baker, D. Christensen, and B. Touri, "Convex relaxation of grid-connected energy storage system models with complementarity constraints in DC OPF," IEEE Transactions on Smart Grid, vol. 11, no. 5, pp. 4070–4079, 2020.

[21] ——, "Guarantees for omitting complementarity constraints in energy management system models," IEEE Transactions on Smart Grid, 2020, under review.

[22] S. Boyd and L. Vandenberghe, Convex Optimization. Cambridge University Press, 2004.

[23] D. Bertsekas, A. Nedic, and A. E. Ozdaglar, Convex Analysis and Optimization. Athena Scientific, 2003.

[24] S. Leyffer, G. López-Calva, and J. Nocedal, "Interior methods for mathematical programs with complementarity constraints," SIAM Journal on Optimization, vol. 17, no. 1, pp. 52–77, 2006.

[25] X. M. Hu and D. Ralph, "Convergence of a penalty method for mathematical programming with complementarity constraints," Journal of Optimization Theory and Applications, vol. 123, no. 2, pp. 365–390, Nov 2004.

[26] J. Hu, J. Mitchell, J. Pang, K. Bennett, and G. Kunapuli, "On the global solution of linear programs with linear complementarity constraints," SIAM Journal on Optimization, vol. 19, no. 1, pp. 445–471, 2008.

[27] H. Scheel and S. Scholtes, "Mathematical programs with complementarity constraints: Stationarity, optimality, and sensitivity," Mathematics of Operations Research, vol. 25, no. 1, pp. 1–22, 2000.

[28] M. Ferris and F. Tin-Loi, "On the solution of a minimum weight elastoplastic problem involving displacement and complementarity constraints," Computer Methods in Applied Mechanics and Engineering, vol. 174, no. 1, pp. 108 – 120, 1999.

[29] M. Anitescu, "On solving mathematical programs with complementarity constraints as nonlinear programs," Preprint ANL/MCS-P864-1200, Argonne National Laboratory, Argonne, IL, vol. 3, 2000.

[30] D. Klatte, First Order Constraint Qualifications. Boston, MA: Springer US, 2009, pp. 1055–1060.

[31] M. Fukushima, Z.-Q. Luo, and J.-S. Pang, "A globally convergent sequential quadratic programming algorithm for mathematical programs with linear complementarity constraints," Computational Optimization and Applications, vol. 10, pp. 5–34, 1998.

[32] A. Zakaria, F. B. Ismail, M. H. Lipu, and M. Hannan, "Uncertainty models for stochastic optimization in renewable energy applications," Renewable Energy, vol. 145, pp. 1543 – 1571, 2020.

[33] A. Charnes, W. W. Cooper, and G. H. Symonds, "Cost horizons and certainty equivalents: An approach to stochastic programming of heating oil," Management Science, vol. 4, no. 3, pp. 235–263, 1958.

[34] A. Charnes and W. W. Cooper, "Chance-constrained programming," Management Science, vol. 6, no. 1, pp. 73–79, 1959.

[35] B. L. Miller and H. M. Wagner, "Chance constrained programming with joint constraints," Operations Research, vol. 13, no. 6, pp. 930–945, 1965.

[36] E. Dall'Anese, K. Baker, and T. Summers, "Chance-constrained AC optimal power flow for distribution systems with renewables," IEEE Transactions on Power Systems, vol. 32, no. 5, pp. 3427–3438, 2017.

[37] T. Summers, J. Warrington, M. Morari, and J. Lygeros, "Stochastic optimal power flow based on conditional value at risk and distributional robustness," International Journal of Electrical Power & Energy Systems, vol. 72, pp. 116 – 125, 2015.

[38] M. Lubin, Y. Dvorkin, and S. Backhaus, "A robust approach to chance constrained optimal power flow with renewable generation," IEEE Transactions on Power Systems, vol. 31, no. 5, pp. 3840–3849, 2016.

[39] F. Oldewurtel, A. Parisio, C. N. Jones, D. Gyalistras, M. Gwerder, V. Stauch, B. Lehmann, and M. Morari, "Use of model predictive control and weather forecasts for energy efficient building climate control," Energy and Buildings, vol. 45, pp. 15 – 27, 2012.

[40] Y. Huang, L. Wang, W. Guo, Q. Kang, and Q. Wu, "Chance constrained optimization in a home energy management system," IEEE Transactions on Smart Grid, vol. 9, no. 1, pp. 252–260, 2018.

[41] D. Bienstock, M. Chertkov, and S. Harnett, "Chance-constrained optimal power flow: Risk-aware network control under uncertainty," SIAM Review, vol. 56, no. 3, pp. 461–495, 2014.

[42] Q. Wang, Y. Guan, and J. Wang, "A chance-constrained two-stage stochastic program for unit commitment with uncertain wind power output," IEEE Transactions on Power Systems, vol. 27, no. 1, pp. 206–215, Feb 2012.

[43] F. Qiu and J. Wang, "Distributionally robust congestion management with dynamic line ratings," IEEE Transactions on Power Systems, vol. 30, no. 4, pp. 2198–2199, July 2015.

[44] M. Vrakopoulou, K. Margellos, J. Lygeros, and G. Andersson, Probabilistic Guarantees for the N-1 Security of Systems with Wind Power Generation. Springer India, 2013.

[45] M. A. Bucher, M. Vrakopoulou, and G. Andersson, "Probabilistic N-1 security assessment incorporating dynamic line ratings," in 2013 IEEE Power and Energy Society General Meeting, July 2013.

[46] B. Singh, B. Knueven, and J. Watson, "Modeling flexible generator operating regions via chance-constrained stochastic unit commitment," Computational Management Science, 2020.

[47] K. Baker, G. Hug, and X. Li, "Optimal storage sizing using two-stage stochastic optimization for intra-hourly dispatch," in 2014 North American Power Symposium (NAPS), Sept 2014.

[48] A. Nemirovski and A. Shapiro, "Convex approximations of chance constrained programs," SIAM Journal on Optimization, vol. 17, no. 4, pp. 969–996, 2007.

[49] A. Prékopa, "Convexity theory of probabilistic constrained problems," in Stochastic Programming. Springer Netherlands, vol. 324, pp. 301–317.

[50] ——, "Two-stage stochastic programming problems," in Stochastic Programming. Springer Netherlands, vol. 324, pp. 301–317.

[51] J. R. Birge and F. Louveaux, Introduction to Stochastic Programming, 2nd ed. Springer, 2011.

[52] A. Ruszczyński and A. Shapiro, "Stochastic programming models," in Stochastic Programming, ser. Handbooks in Operations Research and Management Science. Elsevier, vol. 10, pp. 1–64.

[53] B. Singh and J.-P. Watson, "Approximating two-stage chance-constrained programs with classical probability bounds," Optimization Letters, pp. 1–14, 2019.

[54] C. E. García, D. M. Prett, and M. Morari, "Model predictive control: theory and practice-a survey," Automatica, vol. 25, no. 3, pp. 335–348, 1989.

[55] D. Mayne, J. Rawlings, C. Rao, and P. Scokaert, "Constrained model predictive control: stability and optimality," Automatica, vol. 36, no. 6, pp. 789–814, 2000.

[56] C. Chen, J. Wang, Y. Heo, and S. Kishore, "MPC based appliance scheduling for residential building energy management controller," IEEE Transactions on Smart Grid, vol. 4, no. 3, pp. 1401–1410, 2013.

[57] Z. Bradac, V. Kaczmarczyk, and P. Fiedler, "Optimal scheduling of domestic appliances via MILP," Energies, vol. 8, no. 1, pp. 217–232, 2014.

[58] D. Zhang, S. Li, M. Sun, and Z. O'Neill, "An optimal and learning-based demand response and home energy management system," IEEE Transaction on Smart Grid, vol. 7, no. 4, pp. 1790–1801, 2016.

[59] Y. Du, L. Jiang, Y. Li, and Q. Wu, "A robust optimization approach for demand side scheduling under energy consumption uncertainty of manually operated appliances," IEEE Transactions on Smart Grid, 2017, to be published.

[60] H. Wu, A. Pratt, and S. Chakraborty, "Stochastic optimal scheduling of residential appliances with renewable energy sources," in 2015 IEEE Power and Energy Society General Meeting, 2015.

[61] X. Wu, X. Hu, S. Moura, X. Yin, and V. Pickert, "Stochastic control of smart home energy management with plug-in electric vehicle battery energy storage and photovoltaic array," Journal of Power Sources, vol. 333, pp. 203–212, 2016.

[62] K. Baker, G. Hug, and X. Li, "Energy storage sizing taking into account forecast uncertainties and receding horizon operation," IEEE Transactions on Sustainable Energy, vol. 8, no. 1, pp. 331–340, Jan 2017.

[63] L. J. Wilson, W. R. Burrows, and A. Lanzinger, "A strategy for verification of weather element forecasts from an ensemble prediction system," Monthly Weather Review, vol. 127, no. 6, pp. 956–970, 1999.

[64] M. Grant and S. Boyd, "CVX: Matlab software for disciplined convex programming, version 2.1," http://cvxr.com/cvx, March 2014.

[65] ——, "Graph implementations for nonsmooth convex programs," in Recent Advances in Learning and Control, ser. Lecture Notes in Control and Information Sciences, V. Blondel, S. Boyd, and H. Kimura, Eds. Springer-Verlag Limited, 2008, pp. 95–110, http://stanford.edu/~boyd/graph_dcp.html.

[66] E. Raszmann, K. Baker, Y. Shi, and D. Christensen, "Modeling stationary lithium-ion batteries for optimization and predictive control," in 2017 IEEE Power and Energy Conference at Illinois (PECI), 2017.

[67] H. Diamond, T. Karl, M. Palecki, C. Baker, J. Bell, R. Leeper, D. Easterling, J. Lawrimore, T. Meyers, M. Helfert, G. Goodge, and P. Thorne, "2013: U.S. climate reference network after one decade of operations: status and assessment," Bulletin of the American Meteorological Society, vol. 94, pp. 489–498, 2013.

[68] Xcel Energy, "Time of Use Pricing," https://www.xcelenergy.com/, 2018 [last accessed: November 5, 2018].

[69] Ecotope Inc., "Residential Building Stock Assessment: Metering Study," Northwest Energy Efficiency Alliance, Technical Report E 14-283, April 2014.

[70] C. Barrows, A. Bloom, E. A., J. Jorgenson, D. Krishnamurthy, J. Lau, B. McBennet, M. O'Connell, E. Preston, A. S. Staid, and J. P. Watson, "The IEEE reliability test system: A proposed 2018 update," 2018.

[71] D. Kolkmann and Et. al., "Managing transmission line ratings," U.S. DOE Federal Energy Regulatory Commission, August 2019.

[72] S. Balser, S. Sankar, R. Miller, A. Rawlins, M. Isreal, T. Curry, and T. Mason, "Effective Grid Utilization: A Technical Assessment and Application Guide," National Renewable Energy Laboratory, NREL/SR-5500-53696, Sept 2012. [Online]. Available: https://www.nrel.gov/docs/fy13osti/53696.pdf

[73] C. Grigg, P. Wong, P. Albrecht, R. Allan, M. Bhavaraju, R. Billinton, Q. Chen, C. Fong, S. Haddad, S. Kuruganty, W. Li, R. Mukerji, D. Patton, N. Rau, D. Reppen, A. Schneider, M. Shahidehpour, and C. Singh, "The IEEE reliability test system-1996. A report prepared by the reliability test system task force of the application of probability methods subcommittee," IEEE Transactions on Power Systems, vol. 14, no. 3, pp. 1010–1020, Aug 1999.

[74] B. Banerjee, D. Jayaweera, and S. M. Islam, "Optimal scheduling with dynamic line ratings and intermittent wind power," in 2014 IEEE Power and Energy Society General Meeting, July 2014.

[75] S. Zhang, C. Liu, X. Gu, and T. Wang, "Optimal transmission line switching incorporating dynamic line ratings," in 2017 IEEE PES Innovative Smart Grid Technologies Conference Europe (ISGT-Europe), Sep. 2017.

[76] F. Qiu and J. Wang, "Chance-constrained transmission switching with guaranteed wind power utilization," IEEE Transactions on Power Systems, vol. 30, no. 3, pp. 1270–1278, May 2015.

[77] B.-M. Hodge and M. Milligan, "Wind power forecasting error distributions over multiple timescales," in 2011 IEEE Power and Energy Society General Meeting, 2011.

[78] A. A. Thatte, L. Xie, D. E. Viassolo, and S. Singh, "Risk measure based robust bidding strategy for arbitrage using a wind farm and energy storage," IEEE Transactions on Smart Grid, vol. 4, no. 4, pp. 2191–2199, Dec 2013.

[79] W. E. Hart, C. D. Laird, J. P. Watson, D. L. Woodruff, G. A. Hackebeil, B. L. Nicholson, and J. D. Siirola, Pyomo - Optimization Modeling in Python, 2nd ed. Springer Optimization and Its Applications, 2017.

[80] B. Knueven, C. Laird, J. P. Watson, M. Bynum, A. Castillo, and USDOE. (2019, March) Egret v. 0.1 (beta). [Online]. Available: Available:https://www.osti.gov//servlets/purl/1498854

[81] Gurobi Optimization, LLC, "Gurobi optimizer reference manual," 2020. [Online]. Available: http://www.gurobi.com

[82] IEA, "Energy storage," 2020. [Online]. Available: https://www.iea.org/reports/energy-storage

[83] FERC, "Order 841: Electric storage participation in markets operated by regional transmission organizations and independent system operators," 2018.

[84] O. Erdinc, N. G. Paterakis, T. D. P. Mendes, A. G. Bakirtzis, and J. P. S. Catalao, "Smart household operation considering bi-directional EV and ESS utilization by real-time pricing-based DR," IEEE Transactions on Smart Grid, vol. 6, no. 3, pp. 1281–1291, May 2015.

[85] M. A. F. Ghazvini, J. Soares, O. Abrishambaf, R. Castro, and Z. Vale, "Demand response implementation in smart households," Energy and Buildings, vol. 143, pp. 129 – 148, 2017.

[86] R. Hemmati, "Technical and economic analysis of home energy management system incorporating small-scale wind turbine and battery energy storage system," Journal of Cleaner Production, vol. 159, pp. 106–118, 2017.

[87] R. A. Jabr, S. Karaki, and J. A. Korbane, "Robust multi-period OPF with storage and renewables," IEEE Transactions on Power Systems, vol. 30, no. 5, pp. 2790–2799, Sept 2015.

[88] A. Parisio, E. Rikos, and L. Glielmo, "A model predictive control approach to microgrid operation optimization," IEEE Transactions on Control Systems Technology, vol. 22, no. 5, pp. 1813–1827, Sep. 2014.

[89] D. Wu, T. Yang, A. A. Stoorvogel, and J. Stoustrup, "Distributed optimal coordination for distributed energy resources in power systems," IEEE Transactions on Automation Science and Engineering, vol. 14, no. 2, pp. 414–424, April 2017.

[90] K. Smith, Y. Shi, and S. Santhanagopalan, "Degradation mechanisms and lifetime prediction for lithium-ion batteries: A control perspective," in 2015 American Control Conference (ACC), July 2015, pp. 728–730.

[91] D. Zarrilli, A. Giannitrapani, S. Paoletti, and A. Vicino, "Energy storage operation for voltage control in distribution networks: A receding horizon approach," IEEE Transactions on Control Systems Technology, vol. 26, no. 2, pp. 599–609, 2018.

[92] Z. Li, Q. Guo, H. Sun, and J. Wang, "Storage-like devices in load leveling: Complementarity constraints and a new and exact relaxation method," Applied Energy, vol. 151, pp. 13 – 22, 2015.

[93] Z. Li, Q. Guo, H. Sun, and J. Wang, "Sufficient conditions for exact relaxation of complementarity constraints for storage-concerned economic dispatch," IEEE Transactions on Power Systems, vol. 31, no. 2, pp. 1653–1654, 2016.

[94] A. Castillo and D. F. Gayme, "Profit maximizing storage allocation in power grids," in IEEE Conference on Decision and Control (CDC), 2013.

[95] N. Nazir, P. Racherla, and M. Almassalkhi, "Optimal multi-period dispatch of distributed energy resources in unbalanced distribution feeders," IEEE Transactions on Power Systems, vol. 35, no. 4, pp. 2683–2692, 2020.

[96] A. Sani Hassan, L. Cipcigan, and N. Jenkins, "Optimal battery storage operation for PV systems with tariff incentives," Applied Energy, vol. 203, pp. 422 – 441, 2017.

[97] C. Wouters, E. S. Fraga, and A. M. James, "An energy integrated, multi-microgrid, MILP (mixed-integer linear programming) approach for residential distributed energy system planning – a south australian case-study," Energy, vol. 85, pp. 30 – 44, 2015.

[98] K. Spees and L. Lave, "Impacts of responsive load in PJM: Load shifting and real time pricing," The Energy Journal, vol. 29, no. 2, pp. 101–121, 2008.

[99] S. Diamond and S. Boyd, "CVXPY: A Python-embedded modeling language for convex optimization," Journal of Machine Learning Research, vol. 17, no. 83, pp. 1–5, 2016.

[100] A. Agrawal, R. Verschueren, S. Diamond, and S. Boyd, "A rewriting system for convex optimization problems," Journal of Control and Decision, vol. 5, no. 1, pp. 42–60, 2018.

[101] A. Parisio, E. Rikos, G. Tzamalis, and L. Glielmo, "Use of model predictive control for experimental microgrid optimization," Applied Energy, vol. 115, pp. 37 – 46, 2014.

[102] K. M. Chandy, S. H. Low, U. Topcu, and H. Xu, "A simple optimal power flow model with energy storage," in IEEE Conference on Decision and Control (CDC), Dec 2010, pp. 1051–1057.

[103] Y. Levron, J. M. Guerrero, and Y. Beck, "Optimal power flow in microgrids with energy storage," IEEE Transactions on Power Systems, vol. 28, no. 3, pp. 3226–3234, Aug 2013.

[104] R. D. Zimmerman, C. E. Murrillo-Sanchez, and R. J. Thomas, "MATPOWER: steady-state operations, planning, and analysis tools for power systems research and education," IEEE Transactions on Power Systems, vol. 26, no. 1, pp. 12–19, 2011.

[105] PJM Interconnection, L.L.C. PJM metered load data. Last accessed: October 16, 2019. [Online]. Available: https://dataminer2.pjm.com/feed/hrl_load_metered/definition.

[106] National Renewable Energy Laboratory Wind Integration Data Sets. Eastern solar dataset. Last accessed: October 16, 2019. [Online]. Available: https://www.nrel.gov/grid/solar-power-data.html.

[107] W. E. Hart, C. D. Laird, J.-P. Watson, D. L. Woodruff, G. A. Hackebeil, B. L. Nicholson, and J. D. Siirola, Pyomo–optimization modeling in python, 2nd ed. Springer Science & Business Media, 2017, vol. 67.

[108] W. E. Hart, J.-P. Watson, and D. L. Woodruff, "Pyomo: modeling and solving mathematical programs in python," Mathematical Programming Computation, vol. 3, no. 3, pp. 219–260, 2011.

[109] A. Wächter and L. T. Biegler, "On the implementation of an interior-point filter line-search algorithm for large-scale nonlinear programming," Mathematical Programming, vol. 106, no. 1, pp. 25–57, Mar 2006.

[110] M. B. Cain, R. P. O'neill, and A. Castillo, "History of optimal power flow and formulations," Federal Energy Regulatory Commission, pp. 1–36, 2012.

[111] A. Gómez Expósito and E. Romero Ramos, "Reliable load flow technique for radial distribution networks," IEEE Transactions on Power Systems, vol. 14, no. 3, pp. 1063–1069, 1999.

[112] R. A. Jabr, "Radial distribution load flow using conic programming," IEEE Transactions on Power Systems, vol. 21, no. 3, pp. 1458–1459, 2006.